GEOMAR
Helmholtz Centre for Ocean Research Kiel

Advanced Understanding of the Tropopause Inversion Layer: High-Resolution GPS-RO Observations and Reanalyses

Dissertation
in fulfillment of the requirements for the degree “Dr. rer. Nat.”
of the Faculty of Mathematics and Natural Sciences
at Christian-Albrechts-Universität zu Kiel

Submitted by:
Robin Pilch Kedzierski

Kiel, 2016

First referee: Dr. Katja Matthes
Second referee: Dr. Richard Greatbatch

Date of the oral examination: 2016.10.17
Approved for publication: 2016.10.17

Signed: Dr. Wolfgang J. Duschl, Dean

Table of contents

Abstract

The upper troposphere and lower stratosphere (UTLS) is a region of the atmosphere that acts as a 'transition' between the two layers and consequently has properties from both. Within this region, a fine-scale feature is located: the Tropopause Inversion Layer (TIL), which consists of a sharp temperature inversion at the tropopause and the corresponding high static stability values aloft. The latter theoretically affects the dispersion relations of atmospheric waves like Rossby or Inertia-Gravity waves and hampers stratosphere-troposphere exchange (STE), which is why the TIL is established as an important feature of the UTLS.

The present thesis aims to improve the observational knowledge about the TIL by analyzing high-resolution GPS radio-occultation (GPS-RO) data globally. The focus is on day-to-day and synoptic-scale TIL variability, a novel approach to build upon the climatological point of view from earlier TIL studies. Daily snapshots of the horizontal structures of TIL strength show the first evidence of a relationship between a stronger (weaker) TIL and near-tropopause divergent (convergent) flow in the tropics. In the extratropics, the TIL within mid-latitude ridges in winter is as strong or stronger than the TIL in polar summer, which is strongest in the seasonal zonal-mean according to previous studies.

Also, a dynamical mechanism for TIL enhancement is studied and quantified: the transient tropopause modulation by equatorial and extratropical waves, and the resulting net TIL enhancement. In the tropics, equatorial waves explain an important part of the observed TIL strength, with Kelvin, Rossby and inertia-gravity waves as main contributors. In the extratropics, the modulation by planetary and synoptic-scale waves explains the observed TIL strength at mid-latitudes almost entirely, while also being dominant in polar regions. The role of this transient wave modulation mechanism has not been investigated in TIL literature, and its quantification from GPS-RO observations puts it among the most important TIL enhancing processes.

Lastly, the paradigm that data assimilation worsens the representation of the TIL in reanalyses, valid a decade ago, has been tested in modern systems: the ERA-Interim reanalysis and the ECMWF forecasts. Both systems show TIL improvement by data assimilation increments, updating the earlier status quo.

As a whole, this thesis significantly improves our knowledge about observed properties of the TIL and the mechanisms responsible for its formation and maintenance, and shows that reanalyses are a valuable tool for TIL research.

Zusammenfassung

Die obere Troposphäre und die untere Stratosphäre (UTLS) stellen eine Übergangsschicht dar, die Eigenschaften beider Schichten aufweist. Innerhalb dieser Schicht befindet sich die lokal eng begrenzte Tropopause Inversion Layer (TIL), welche durch eine markante Temperaturinversion an der Tropopause und eine daraus resultierende hohe statische Stabilität oberhalb dieser charakterisiert ist. Letztere beeinflusst theoretischen Betrachtungen zufolge die Dispersionsrelationen atmosphärischer Wellen (z.B. Rossby- oder Schwerewellen) und behindert den stratosphärisch-troposphärischen Austausch (STE), weshalb der Erforschung der TIL als Bestandteil der UTLS besondere Aufmerksamkeit gewidmet wird.

Ziel der vorliegenden Arbeit ist eine verbesserte Analyse der TIL und der mit ihr verbundenen Prozesse anhand von hochaufgelösten globalen Daten auf Basis der GPS Radio-Okkultation (GPS-RO). Der Analyseschwerpunkt liegt in der Untersuchung der Variabilität auf täglichen und synoptischen Skalen. Im Gegensatz zu früheren Studien auf klimatologischer Basis kann diese Herangehensweise als neuer Ansatz verstanden werden, da tägliche Momentaufnahmen der horizontalen Strukturen der TIL es erlauben, erstmals einen Zusammenhang zwischen einer stark (schwach) ausgeprägten TIL und divergenten (konvergenten) Strömungen nahe der Tropopause in den Tropen aufzuzeigen. In den Extratropen ist die TIL im Winter im Bereich von atmosphärischen Rücken in den mittleren Breiten ebenso stark oder sogar stärker ausgeprägt als die TIL im polaren Sommer, die entsprechend früherer Studien im zonalen Mittel am stärksten ausgeprägt ist.

Desweiteren wird in dieser Arbeit ein dynamischer Prozess untersucht und quantifiziert, der zu einer Verstärkung der TIL führt: Die kurzlebige Tropopausenmodulation aufgrund von äquatorialen und extratropischen Wellen sowie die resultierende Gesamtverstärkung der TIL. Es wird gezeigt, dass die TIL in den Tropen im wesentlichen durch äquatoriale Wellen, hauptsächlich Kelvin-, Rossby- und Trägheitsschwerewellen, verstärkt wird, während in den mittleren wie auch polaren Breiten die Modulation durch Wellen auf planetarer sowie synoptischer Skala dominiert. Der Einfluss des in dieser Arbeit untersuchten Wellen-Modulations-Mechanismus auf die TIL wurde in früheren Studien zur TIL nicht diskutiert, obwohl seine Quantifizierung mit Hilfe der GPS-RO Beobachtungen in dieser Studie zeigt, das er als einer der wichtigsten Verstärkungsprozesse der TIL angesehen werden muss.

Schließlich wird das vor einem Jahrzehnt gültige Paradigma, dass die Datenassimilation die Repräsentation der TIL in Reanalysen verschlechtert, anhand neuer Datensätze (ERA-Interim und EZMW-Vorhersagen) überprüft. In beiden Datensätzen ist die TIL durch Fortschritte in der Datenassimilation deutlich realistischer dargestellt, was die früheren Feststellungen über die Qualität der Reanalysedaten revidiert.

Zusammengefasst, liefert diese Arbeit wichtige Beiträge, um unsere Kenntnisse über das Erscheinungsbild der TIL sowie die für ihre Bildung und Aufrechterhaltung relevanten Prozesse zu erweitern. Außerdem zeigt sie, dass die aktuellen Reanalysedaten ein wertvoller Tool für die Untersuchung der TIL sind.

1 Introduction

1.1 What is the Tropopause Inversion Layer?

The Tropopause Inversion Layer (TIL) is a narrow region characterized by a sharp temperature inversion at the tropopause and the corresponding enhanced static stability located right above. The TIL is a fine-scale feature of about 1 km depth, discovered by tropopause-based averaging of high-resolution radiosonde measurements by *Birner et al.* [2002] and *Birner* [2006]. Satellite Global Positioning System radio occultation observations (GPS-RO) show that the TIL is present globally [*Grise et al.*, 2010].

Figure 1.1 shows vertical profiles of temperature and static stability (N^2) at mid-latitudes, comparing the tropopause-based and ground-based averaging techniques (from *Birner* [2006]).

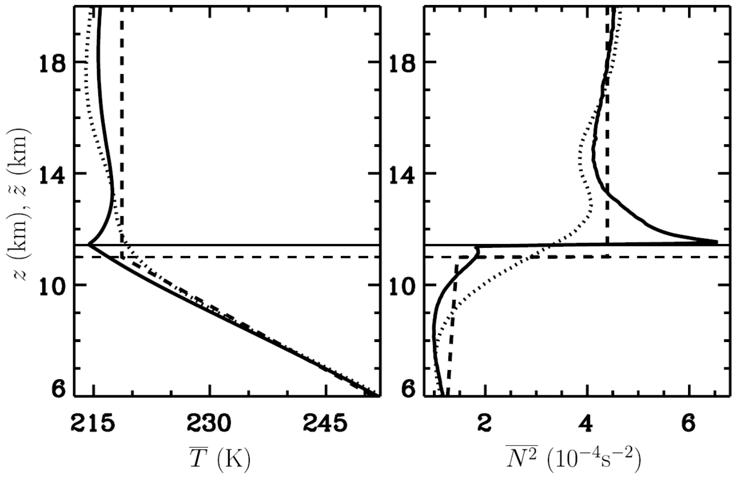

Fig. 1.1 Climatological profiles of temperature (left) and buoyancy frequency squared (right) at ~45°N from high-resolution radiosondes (1998-2002). Dotted lines are a ground-based average, solid lines are a tropopause-based average, and the dashed lines denote the US standard atmosphere profiles. Figure from *Birner* [2006].

Only when averaging is performed with respect to the tropopause level as the reference, the temperature inversion and maximum in N^2 are clearly visible in Fig. 1.1 (solid black lines), with very sharp gradients across just a few hundred meters: therefore observations with very high vertical resolution are needed in order to capture these gradients.

The TIL is located within a region of the atmosphere that has properties from both the troposphere and the stratosphere as a consequence of the transition between these two layers. In the tropics this transition layer is known as the Tropical Tropopause Layer (TTL, *Fueglistaler et al.* [2009]), and at other latitudes as the extratropical upper-troposphere and lower-stratosphere (Ex-UTLS, *Gettelman et al.* [2011]). The TIL is established as an important feature of the UTLS [*Gettelman et al.*, 2011] since it shows that the transition between the troposphere and the stratosphere is rather sharp at a certain and narrow altitude range. Figure 1.2 shows a UTLS schematic with the location of the TIL and the tropopause structures and processes that take place at different latitudes (from *Gettelman et al.* [2011]).

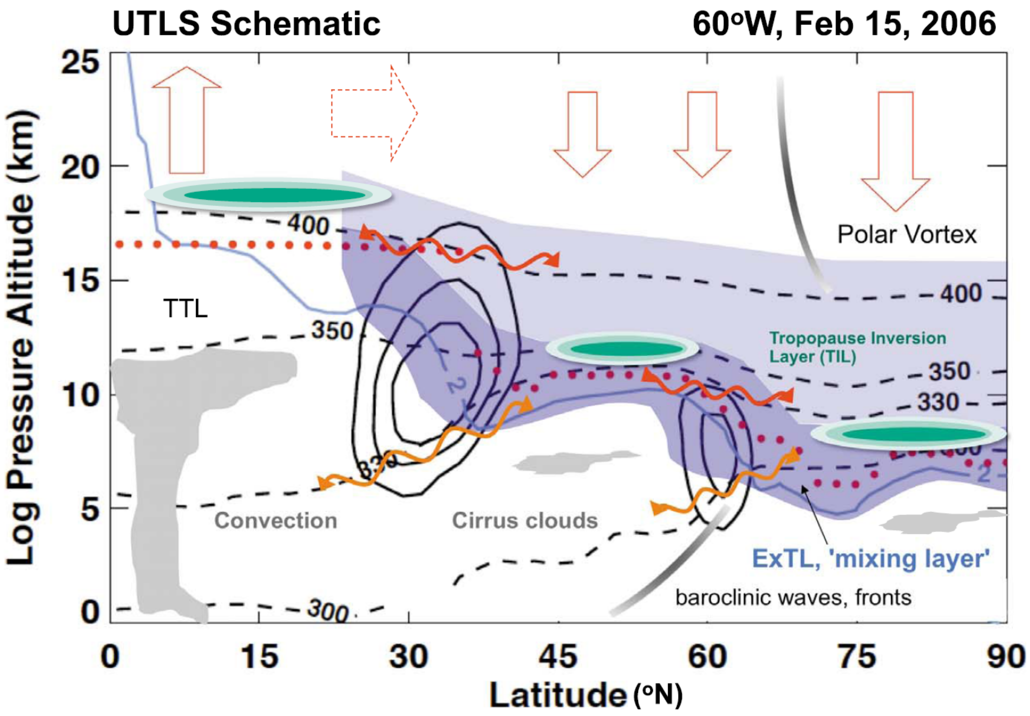

Fig. 1.2 Schematic snapshot of the extratropical UTLS, as a meridional section in the Northern Hemisphere. Shown are zonal winds (solid black lines), potential temperature surfaces (dashed black lines), the thermal tropopause (red dots) and the dynamical tropopause (2 PVU surface, light blue solid line). Illustrated are sketches of the TIL (green shading), the Brewer-Dobson Circulation (red arrows at the top), quasi-isentropic exchange (wavy red arrows), cross-isentropic exchange (wavy orange arrows) and clouds and fronts (gray shading). The extratropical UTLS is represented by blue shading, including the 'mixing layer' (dark blue shading). Figure from *Gettelman et al.* [2011].

What are the implications of the TIL? As shown in Fig. 1.1, the positive gradient of temperature right above the tropopause translates into high N^2 values, distinctly above those found throughout the stratosphere. High static stability suppresses vertical motion, therefore inhibiting the cross-tropopause exchange of chemical compounds, which is why the vertical

N^2 structure near the tropopause is correlated with the strength of trace gas gradients [*Hegglin et al.*, 2009; *Kunz et al.*, 2009; *Schmidt et al.*, 2010]. Hence the TIL could significantly influence the stratosphere-troposphere exchange (STE) and the composition of both layers. Also, N^2 is a parameter used in different atmospheric wave theory approximations [*Andrews et al.*, 1987], so the TIL shall theoretically affect the dispersion relations of Rossby and Inertia-Gravity waves.

To summarize, the TIL is a relatively recent and growing topic of research, whose study needs observations with high vertical resolution due to its fine-scale nature. The TIL could potentially play an important role in the chemical composition and the dynamics of the troposphere and the stratosphere, as well as the interactions between these two atmospheric layers.

1.2 Observed Variability of the TIL

This subsection will introduce the properties of the TIL which have been observed thus far. A subdivision between the tropics and extratropics applies given the difference in the dominant physical processes between these regions: radiative-convective balance in the tropics and baroclinic wave dynamics in the extratropics [*Held*, 1982]; therefore the TIL shows a different behavior in each region. The proposed mechanisms that drive the observed TIL variability will be discussed in the next subsection 1.3.

1.2.1 Tropics

Research about the TIL has focused very little in the tropics. The global TIL study by *Grise et al.* [2010] includes the horizontal and vertical variability of the tropical TIL, making it the most detailed description of TIL properties in the tropics. *Bell and Geller* [2008] showed the TIL from one tropical radiosonde station, and *Wang et al.* [2013] reported a slight weakening of the tropical TIL between 2001-2011. In the study by *Grise et al.* [2010] it was found that the strongest tropical TIL (as the mean N^2 in the layer 0-1 km above the tropopause) is centered at the equator, peaking during NH winter. Later studies by *Son et al.* [2011] and *Kim and Son* [2012] agree well with this seasonality and location of the tropical tropopause sharpness.

Figure 1.3 shows the seasonal cycle of the vertical tropopause-based N^2 structure in the subtropics and the equator (from *Grise et al.* [2010]). The tropopause is higher in winter throughout the tropics, which is related to the seasonal cycle of the stratospheric Brewer-Dobson circulation [*Yulaeva et al.*, 1994].

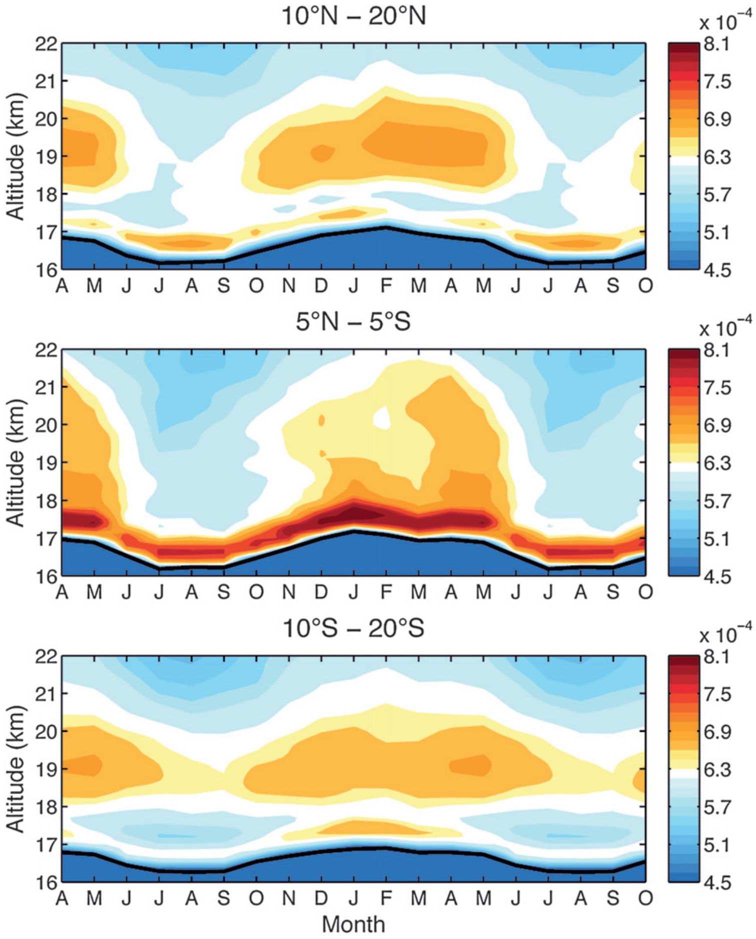

Fig. 1.3 Seasonal cycle of the monthly tropopause-based N^2 vertical profile (color shading) at the NH subtropics, the equator and the SH subtropics. The black solid line represents the tropopause. Figure from *Grise et al.* [2010].

In the layer right above the tropopause, the equator shows the highest N^2 values, peaking in winter. In the subtropics, both hemispheres show a stronger TIL during their respective summer months, while another deeper region of enhanced N^2, centered at 19 km height, forms during NH winter. This second subtropical maximum in N^2 at 19 km is related to the large seasonal cycle of temperature and ozone within that altitude range [*Randel et al.*, 2007b]. The fact that the highest N^2 values right above the tropopause are centered around the equator indicates that the tropical TIL is strongly influenced by equatorially-trapped wave modes.

Indeed, the seasonal-mean horizontal structure of the TIL in the tropics is reminiscent of the equatorial stationary wave response associated with climatological deep convection [*Grise et al.*, 2010; *Kim and Son*, 2012]. *Grise et al.* [2010] also found higher N^2 in the layer

1-3 km above the tropopause and throughout the stratosphere during the easterly phase of the quasi-biennial oscillation (QBO, *Baldwin et al.* [2001]).

1.2.2 Extratropics

Studies about observational properties of the extratropical TIL are more numerous. Seasonal climatologies of the zonal-mean TIL show that it is strongest during polar summer, while another relative maximum in TIL strength is observed in mid-latitude winter [*Birner*, 2006; *Grise et al.*, 2010; *Randel and Wu*, 2010; *Randel et al.*, 2007a]. This is shown in the latitude-height N^2 seasonal tropopause-based climatologies in Figure 1.4 (from *Grise et al.* [2010]). Note that both maxima in extratropical TIL strength during polar summer and mid-latitude winter are still below the high N^2 values observed right above the tropical tropopause and centered at the equator.

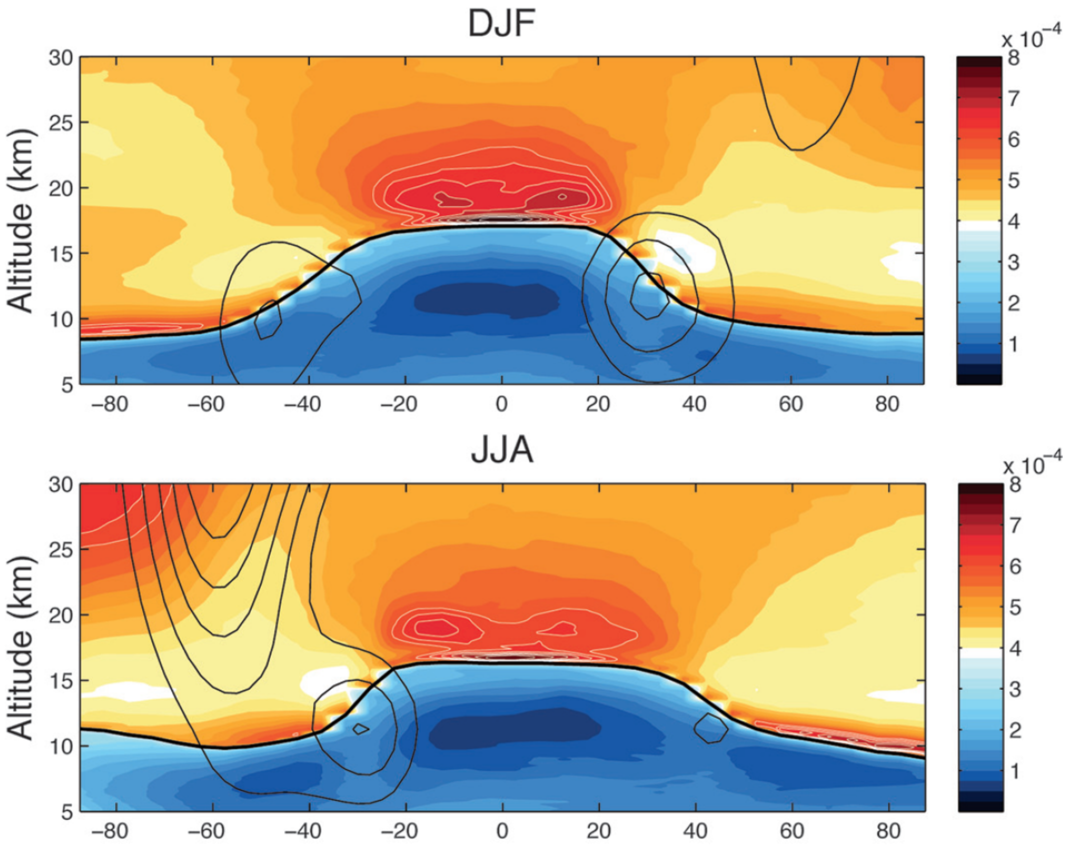

Fig. 1.4 Seasonal zonal and tropopause-based mean N^2 global vertical structure (color shading), for NH winter and summer (top and bottom, respectively). Black contours represent the seasonal zonal mean zonal winds, starting at 20 m/s with 10 m/s intervals. Figure from *Grise et al.* [2010].

The cyclones and anticyclones embedded within baroclinic waves clearly modulate the extratropical TIL strength. Observations show a stronger (weaker) TIL within anticyclones (cyclones) at all extratropical latitudes and seasons. Figure 1.5 shows this relationship in mid-latitude winter (left, from *Randel et al.* [2007a]) and polar summer (right, from *Randel and Wu* [2010]) as the dependence of stronger (weaker) TIL with collocated anticyclonic (cyclonic) relative vorticity. This relationship comes together with higher (lower) tropopauses within anticyclones (cyclones).

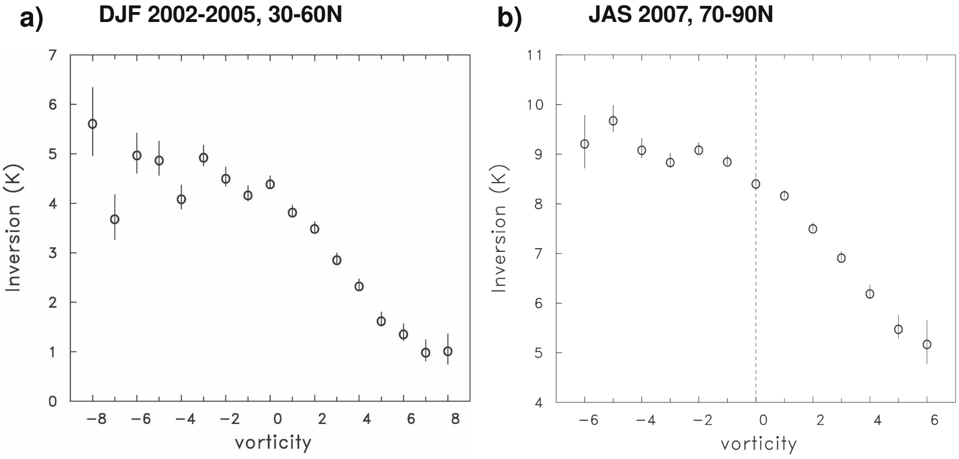

Fig. 1.5 Diagrams of relative vorticity ($10^{-5}s^{-1}$) versus TIL strength, as the temperature difference in K between the tropopause and 2 km above. (a) Mid-latitude winter; (b) polar summer. Figures from *Randel et al.* [2007a] and *Randel and Wu* [2010].

Polar vortex dynamics also influence the TIL: [*Grise et al.*, 2010] found stronger high-latitude TIL correlated with downward-propagating positive N^2 and easterly wind anomalies that result from strong vortex disturbances, which is supported by a case study of major sudden stratospheric warmings (SSW) by *Wargan and Coy* [2016]. On the other hand, the Southern Hemisphere polar winter TIL is nearly absent [*Tomikawa et al.*, 2009], since the polar vortex is strong, stable and cold there.

And finally, inertia-gravity waves (IGW) can affect the TIL and viceversa: a study with one US radiosonde station [*Zhang et al.*, 2015] showed that the upward propagation of IGW is inhibited by the TIL, and also that the TIL can cause IGW breaking from shear instability, which subsequently strengthens the TIL (see section 1.3 for more details about the mechanism).

1.3 Processes enhancing the TIL

The present consensus about what forces the TIL is that a blend of different mechanisms, whose dominance varies with season and latitude, are responsible for its formation and maintenance. As shown in Fig. 1.1 in section 1.1, the TIL consists of a sharp temperature inversion at the tropopause, and the resulting temperature gradient right above the tropopause causes its high N^2 values. Therefore, processes making this temperature gradient larger will effectively enhance the TIL. This can be accomplished in two ways: by cooling the tropopause and/or warming aloft, as sketched in Figure 1.6. The processes that have been proposed to enhance the TIL will be disclosed in the following paragraphs.

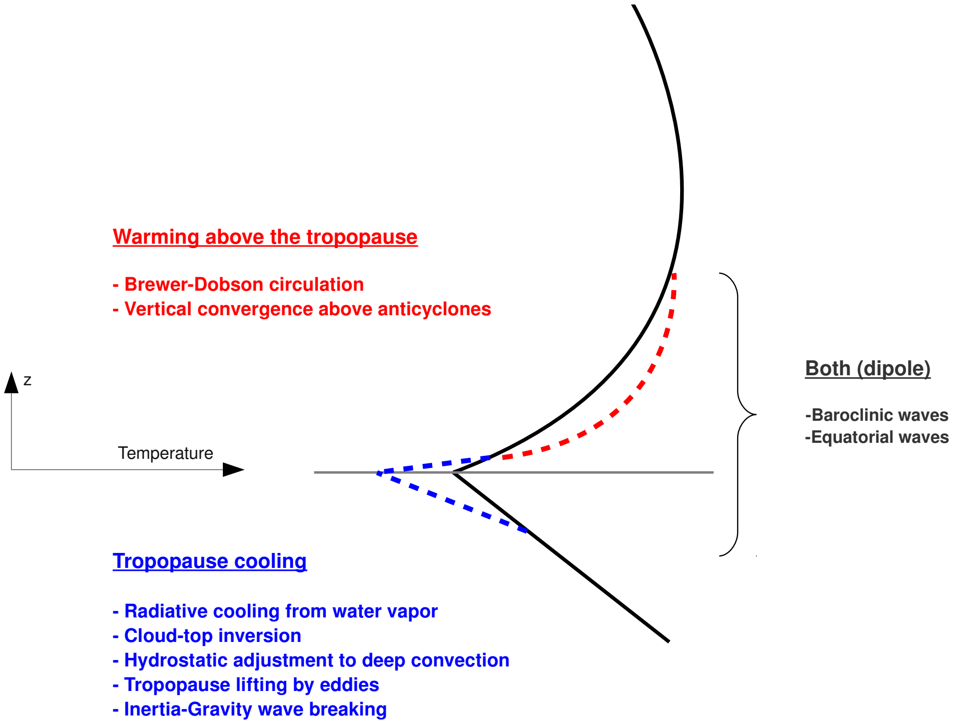

Fig. 1.6 Sketch of TIL enhancement by different processes: tropopause cooling (blue dashed line) and warming aloft (red dashed line) on a generic tropopause-based temperature profile (solid black line) similar to that in Fig. 1.1.

Tropopause cooling

- Radiative cooling from water vapor: the strong gradient of water vapor across the tropopause leads to a differential cooling around the tropopause. This was first proposed by *Randel et al.* [2007a] and later supported by *Hegglin et al.* [2009]; *Kunz et al.* [2009]; *Randel and Wu* [2010]. A high-resolution model study by *Miyazaki et al.* [2010a,b] showed that this mechanism is dominant enhancing the TIL in polar summer.

- Cloud-top inversion: case studies using GPS-RO data have investigated the sharp temperature inversion generally found at the top of convective [*Biondi et al.*, 2012] and non-convective cirrus clouds [*Taylor et al.*, 2011]. Note that cirrus cloud occurrence near the tropopause is more frequent. Although near-tropopause clouds and the TIL have not been linked in scientific literature thus far, we suggest that a cloud top near the tropopause would have a TIL enhancing effect.

- Hydrostatic adjustment to deep convection: this is a purely dynamical response to compensate the pressure gradients from tropospheric warming, that extend above the heating. Ascent and adiabatic cooling act to diminish these pressure gradients with height, cooling the tropopause region above the deep convective tower. *Holloway and Neelin* [2007] described the hydrostatic adjustment mechanism, and *Paulik and Birner* [2012] showed that the negative temperature signal near the tropical tropopause can be found a few thousand kilometers away from the convective region. This mechanism could be important for TIL enhancement in the tropics, which has not been studied yet.

- Tropopause lifting by eddies: model experiments have shown that dry dynamics explain an important part of the extratropical TIL behavior. Baroclinic waves have embedded cyclones and anticyclones, and balanced dry dynamics produce a higher and colder tropopause within anticyclonic flow in idealized model experiments [*Wirth*, 2003, 2004]. This is consistent with the findings by *Randel and Wu* [2010]; *Randel et al.* [2007a], who observed higher tropopauses within anticyclonic flow together with stronger TIL. As shown in Figure 1.5 (section 1.2), the TIL relationship with relative vorticity is present at all extratropical latitudes.

- Inertia-Gravity wave breaking: a baroclinic life cycle experiment by *Kunkel et al.* [2014] showed transient TIL modulation by the presence of IGWs and proposed a mechanism of persistent TIL enhancement from IGW breaking. The study by [*Zhang et al.*, 2015] with one US radiosonde station supports this hypothesis by finding that the strong wind shear above the tropopause causes instability and breaking of IGWs, inducing wave energy dissipation, turbulence and downward heat flux, which in turn leads to a net cooling of the tropopause.

Warming above the tropopause

- Brewer-Dobson circulation: in a model experiment *Birner* [2010] proposed that the downwelling branch of the Brewer-Dobson circulation should produce dynamical heating above the tropopause. This is supported by a case study of major SSWs by *Wargan and Coy* [2016], who showed a high-latitude TIL enhancement by SSWs, when their downward-propagating temperature and N^2 signals reach the tropopause region. This signal is driven by the convergence of the vertical component of the residual circulation ($\overline{w*}$) [*Wargan and Coy*, 2016], which is accelerated during these events in agreement with *Andrews et al.* [1987].

- Vertical convergence above anticyclones: model experiments showed an onset of a secondary circulation between the cyclone and anticyclone embedded within a baroclinic wave *Wirth* [2004]; *Wirth and Szabo* [2007] which induces a heating above the tropopause in anticyclones. Vertical divergence above cyclones reduces the TIL strength, but only partly counteracts the TIL enhancement over anticyclones, which dominate the zonal mean.

Dipole by waves

- Baroclinic waves: as explained in the previous paragraphs, baroclinic waves effectively form a dipole of tropopause cooling and warming aloft through separated mechanisms acting at the same time: tropopause lifting and vertical convergence above anticyclonic flow [*Wirth*, 2003, 2004; *Wirth and Szabo*, 2007], which are explained by balanced dry dynamics. An idealized model experiment with only dry, synoptic-scale dynamics by *Son and Polvani* [2007] was able to partly explain the seasonality and latitude-dependence of the extratropical TIL strength which follows the amount of baroclinic wave activity. Also, baroclinic wave breaking skews the relative vorticity distribution near the tropopause towards anticyclonic values [*Erler and Wirth*, 2011], further increasing the dominance of anticyclonic TIL in the zonal-mean.

- Equatorial waves: since the tropical TIL strength is centered at the equator, the role of equatorially-trapped wave modes has to be important for the formation of the TIL in the tropics [*Grise et al.*, 2010]. An important part of the equatorial wave spectrum is coupled to convection [*Wheeler and Kiladis*, 1999], so the aforementioned tropopause cooling from hydrostatic adjustment to deep convection [*Holloway and Neelin*, 2007; *Paulik and Birner*, 2012] can be included in this dipole, although convection can be independent of equatorial waves as well, and equatorial waves can also propagate freely. *Kim and Son* [2012] reported that the dominant modes of temperature variability at the tropopause region were Kelvin waves and the Madden-Julian oscillation (MJO, *Madden and Julian* [1994]). Equatorial wave temperature anomalies show lower-stratospheric warming and tropopause cooling in composites [*Kim and Son*, 2012] and average signatures on the long-term mean profile [*Grise and Thompson*, 2013], but their effect on the strength of the TIL has not been studied.

It has to be noted that all the mechanisms disclosed above target permanent and irreversible effects on TIL strength. Little attention has been payed to the contribution of atmospheric waves just by being present in the tropopause region, i.e. by a transient and reversible modulation of the temperature structures near the tropopause. Extratropical waves (baroclinic or IGW) and equatorial waves, all have vertical tilts in their temperature structures.

If these temperature anomalies are large, they can effectively modulate tropopause height, as shown schematically in Figure 1.7.

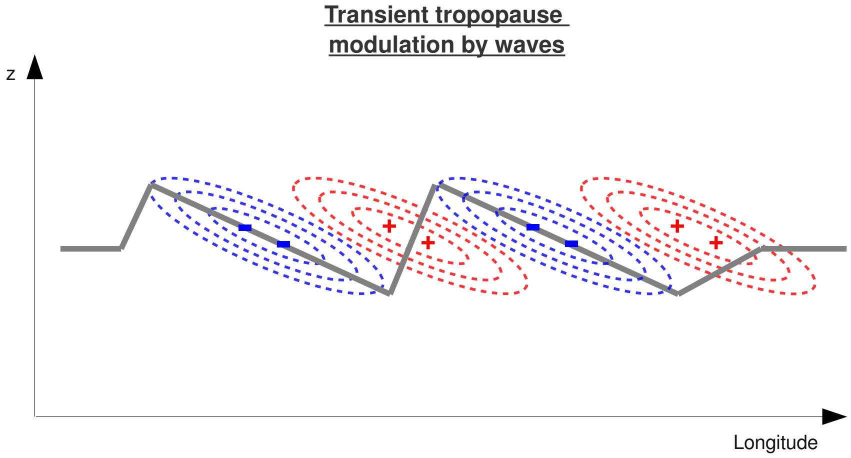

Fig. 1.7 Schematic of transient tropopause modulation by an idealized wave with westward vertical tilt, as a snapshot of the wave's temperature anomalies (dashed contours: positive red, negative blue) and the undulating tropopause (thick solid grey line). Figure from *Pilch Kedzierski et al.* [2016b].

Tropopause height, usually the coldest point at the uppermost troposphere, would vary zonally as a consequence of the wave anomaly structure. The zonal-mean tropopause height, the zonal-mean (ground-based) temperature or N^2 structure are not affected by the instantaneous tilted wave structure as in Fig. 1.7. However, the tropopause-based mean of the wave anomaly would turn to be a dipole of tropopause cooling and warming above, resulting in N^2 increase right above the tropopause, yielding a TIL. Once the wave is away from the tropopause or dissipated, it would not modulate the tropopause any more, but could still affect the TIL in other ways.

It would be of interest to know how much of the TIL is the result of the mere presence of transient atmospheric waves, which enables to separate the instantaneous modulation of the tropopause (and net TIL enhancement in the tropopause-based mean as in Fig. 1.7) from other permanent TIL forcings as disclosed before in this section. The mechanism showed in Fig. 1.7 has not been studied or quantified in any literature so far, thus being of great value for increasing the knowledge about the processes that enhance the TIL: see section 1.5 for more details about the goals of this thesis.

1.4 Representation of the TIL in models and reanalyses

The TIL is a fine-scale feature whose properties can only be captured by data of high vertical resolution (∼100 m), i.e. GPS radio occultation (GPS-RO) profiles by satellites, and high-resolution radiosonde measurements. Atmospheric models are very limited in this sense, generally having a vertical resolution near the tropopause of around 1 km. *Hegglin et al.* [2010] and *Gettelman et al.* [2010] compared the TIL in various models within the Chemistry Climate Model Validation project 2 (CCMVal-2). They also degraded the vertical resolution of GPS-RO observations to the models' standard pressure levels in order to eliminate vertical resolution as a source of differences.

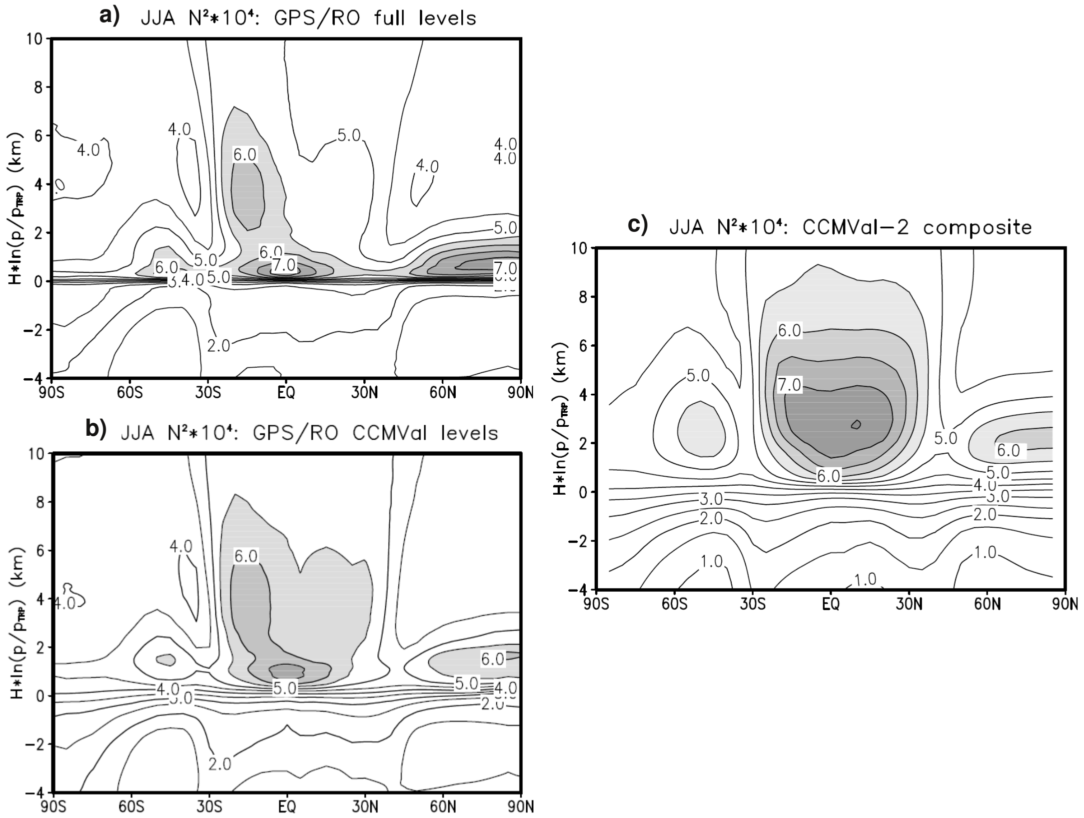

Fig. 1.8 Comparison of the representation of the TIL in (a) full resolution GPS-RO observations, (b) GPS-RO degraded to model resolution, and (c) CCMVal-2 models. Figure from *Gettelman et al.* [2010].

Figure 1.8 shows a latitude-height NH summer climatology of tropopause-based N^2 from GPS-RO at full resolution (Fig. 1.8 a), GPS-RO at the same vertical resolution as the models

(Fig. 1.8 b), and finally the TIL produced by the CCMVal-2 models (Fig. 1.8 c), all from *Gettelman et al.* [2010].

It can be observed that especially in the extratropics the modeled TIL (Fig. 1.8 c) is too weak, too deep and very far away from the tropopause compared to the observed TIL from GPS-RO data at full vertical resolution (Fig. 1.8 a). When the vertical resolution of GPS-RO is degraded, the N^2 values above the tropopause (Fig. 1.8 b) are similar to those from the CCMVal-2 models, but still much closer to the tropopause, suggesting that the coarser vertical resolution in the models is not the only issue that causes a rather poor representation of the TIL. Despite this bias in the CCMVal-2 models, with weaker TIL and further away from the tropopause, its seasonality and latitude-dependence are well captured [*Gettelman et al.*, 2010; *Hegglin et al.*, 2010].

Birner et al. [2006] investigated the TIL in two data assimilation systems, the NCEP/NCAR reanalysis [*Kalnay et al.*, 1996], and the Canadian Middle Atmosphere Model assimilating observations (CMAM+DA, *Polavarapu et al.* [2005]); both with similar vertical resolution of roughly 1km near the tropopause and the same three-dimensional variational (3D-Var) data assimilation technique. *Birner et al.* [2006] found that the TIL from the free-running CMAM was stronger than the TIL from CMAM with data assimilation and the NCAR reanalysis, therefore suggesting that data assimilation smooths out the sharp gradients that lead to the formation of the TIL. This is well illustrated in Fig. 1.9, that shows the response of the TIL strength to data being assimilated into the CMAM model.

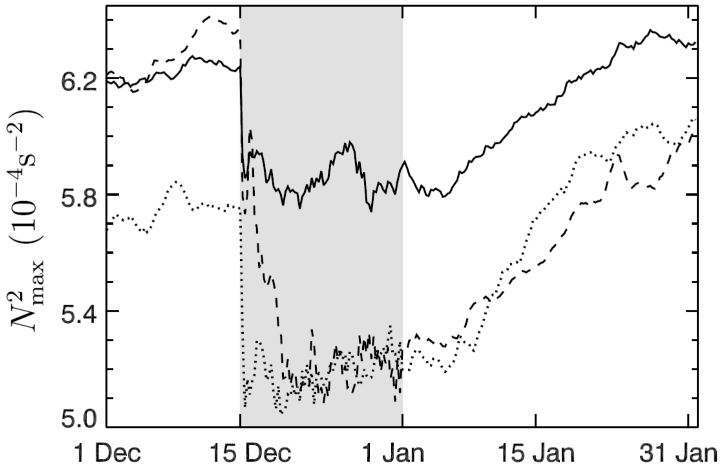

Fig. 1.9 Time series of TIL strength as N^2_{max}, from December 2001 to the end of January 2002. Line types denote different latitudes: global mean (solid), NH mid-latitudes (45°N-75°N, dotted), SH mid-latitudes (45°S-75°S, dashed). Grey shading shows the time period when data assimilation is active in CMAM. Figure from *Birner et al.* [2006].

As soon as data assimilation is switched on (15 Dec) in CMAM+DA, the TIL strength drops dramatically in Fig. 1.9 and remains low while data is assimilated (grey shading). As soon as data assimilation is switched off (1 Jan), the TIL starts recovering slowly. Therefore it is accepted that the TIL in a model gets worse once data is assimilated, as it is the case in reanalyses.

It has to be pointed out that GPS-RO data could not be assimilated at the time of the study by *Birner et al.* [2006], and that the models as well as the assimilation techniques have improved and are more sophisticated nowadays. Recently, modern reanalyses have been used to study the TIL, as is the case in *Gettelman and Wang* [2015] who produced a set of TIL diagnostics from ERA-Interim [*Dee et al.*, 2011], and *Wargan and Coy* [2016] who investigated the TIL in a case study of a major SSW in the Modern-Era Retrospective Analysis for Research and Applications version 2 (MERRA-2, *Bosilovich and Coauthors* [2015]; *Molod et al.* [2015]), proving both reanalyses useful for studying the TIL. Therefore the question arises whether data assimilation still makes the TIL worse in modern reanalyses.

1.5 Goals of this Thesis

This thesis broadly aims to increase the knowledge about TIL properties, the processes that lead to its formation/maintenance/enhancement and how data assimilation affects TIL representation in models. The goals of this thesis can be summarized into three main points, each of which groups several scientific questions, as disclosed below:

(a) Discover more TIL properties from observations: current knowledge about TIL properties is from climatologies, and smaller space and time-scales have not been explored yet.

- How does the real-time TIL look like? Most of the observed properties of the TIL, like the seasonality and latitude-dependence of its strength, were derived from climatologies, i.e. long-term means [*Birner*, 2006; *Grise et al.*, 2010]. At synoptic-scales, its relationship with cyclonic-anticyclonic flow is known as seasonal averages binned by collocated relative vorticity [*Randel and Wu*, 2010; *Randel et al.*, 2007a]. Snapshots of the horizontal structures of the TIL from observations will give a novel approach to study its day-to-day, synoptic-scale behavior.

- Done the above, can we make new links between the observed TIL and near-tropopause meteorological processes? The synoptic-scale behavior of the TIL can be linked to ongoing (collocated in space and time) dynamical processes near the tropopause, so this approach at least will be useful to confirm some TIL enhancing mechanisms that have been proposed in literature from model experiments (see section 1.3) but still await observational evidence.

(b) Quantify the transient TIL modulation by atmospheric waves: this mechanism for TIL enhancement has not been investigated in literature and could play an important role.

- How much of the TIL comes from the instantaneous tropopause modulation by waves? Wave temperature anomalies and tropopause structures as sketched in Fig. 1.7 can be obtained from gridded GPS-RO observations (see section 2, Methods). Separating the relative contribution for TIL enhancement that is transient from other permanent processes can help to put their roles into context, which would be of high interest for the scientific community.

- What other processes enhance the remaining TIL without the wave signal? The vertical structure and time variability of the remaining N^2 structures without the wave signal can give very useful hints about what processes cause it, a valuable secondary result of the quantification of the TIL wave modulation.

(c) Test the hypothesis of *Birner et al.* [2006] in modern reanalyses: the study by *Birner et al.* [2006] is, up to date, the only one investigating the effect of data assimilation on the modeled TIL. A decade ago, data assimilation acted to smooth out the sharp gradients from the TIL, but assimilation techniques and models are more sophisticated nowadays.

- Does data assimilation improve the representation of the TIL in modern reanalyses? Newer reanalyses are being useful for research about the TIL, so an affirmative answer to this question would change the paradigm about how data assimilation affects the TIL, and encourage further use of reanalyses in TIL research.

- In the process, the representation of the TIL in the ERA-Interim reanalysis and the European Centre for Medium-Range Weather Forecasts (ECMWF) system, and the direct effect of the data assimilation increments will be disclosed.

Section 3 will deal with points **a** and **b** in the tropics, and section 4 will do the same for the extratropics. Section 5 focuses on point **c**. These sections consist solely of reprints of articles published or submitted to scientific journals. Section 2 will give a general overview of the methodology that the publications of this thesis have in common. To finish, section 6 will summarize the main conclusions of this thesis and give an outlook about current research possibilities.

2 Methods

This section describes the datasets and methods that the majority of publications included in this thesis have in common, to serve as a general overview of all papers' methodologies.

As mentioned in the Introduction, the TIL needs observations of very high vertical resolution in order to show its fine-scale structure. Satellite GPS-RO temperature profiles are the primary source of data used in this thesis (see section 2.1.1), complemented by wind information from ERA-Interim reanalysis (see section 2.1.2). How the TIL is diagnosed from the temperature data is explained in section 2.2, and the extraction of the longitude-height wave structures (as in Fig. 1.7) is explained in section 2.3.

2.1 Datasets

2.1.1 GPS Radio-Occultation profiles

The GPS radio occultation is a technique for sounding the Earth's atmosphere that provides temperature profiles at high vertical resolution. The proof-of-concept of this technique was carried out by the GPS Meteorology (GPS/MET) experiment in 1995-1997 [*Kursinski et al.*, 1996; *Ware et al.*, 1996]. Datasets derived from GPS-RO profiles are provided at a vertical grid with constant 100 m separation, from the ground up to 40 km height, which is comparable to the vertical resolution of radiosondes. GPS-RO has the advantage of weather-independence and global coverage, compared to radiosondes which are restricted to land or ships. Also, GPS-RO soundings are more precise [*Anthes et al.*, 2008; *WMO*, 1996], and higher in number: the COSMIC mission currently provides $\sim$2000 profiles per day [*Anthes et al.*, 2008] compared to the daily $\sim$1500 radiosonde launches.

Figure 2.1 a compares vertical temperature profiles from a GPS/MET occultation (thick line), a radiosounding (thin line) and the ECMWF model (dotted line), collocated in space and time on the left. The right-hand side of Fig. 2.1 a shows the differences between the occultation and the radiosonde and ECMWF. It can be observed that the GPS-RO and radiosonde profiles on the left are close to overlap, showing very good agreement whereas the modelled temperature from ECMWF differs more.

Figure 2.1 b shows the global distribution of daily COSMIC occultations (green) and radiosoundings (red). Radiosondes hardly cover oceanic regions and the Southern Hemisphere, where COSMIC is the primary source of high-resolution observations of the UTLS.

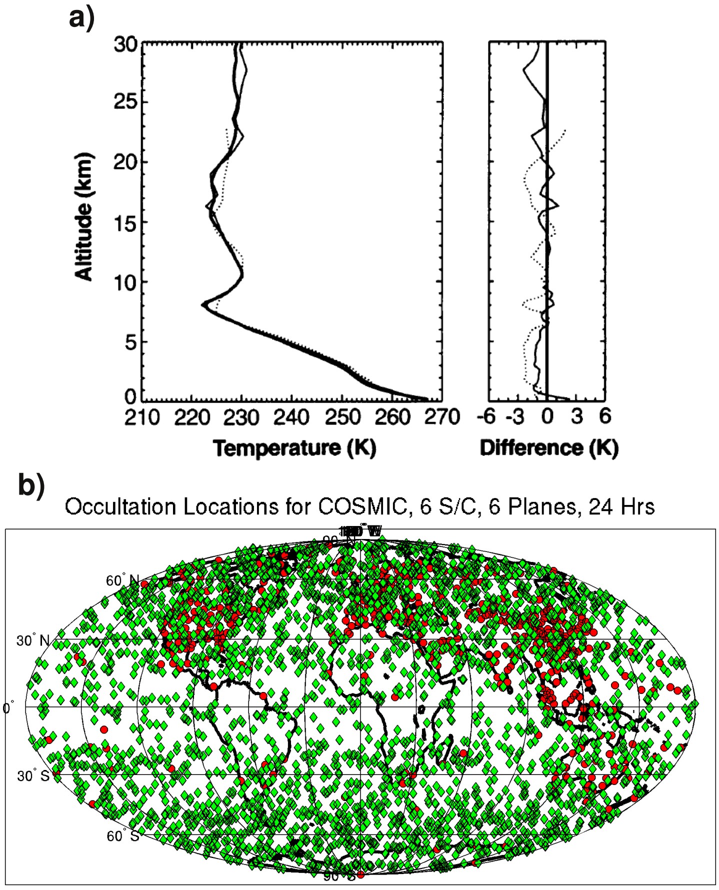

Fig. 2.1 (a) Left: comparison of collocated temperature profiles near Hall Beach (Canada) from occultation (thick line), radiosonde (thin line) and ECMWF (dotted line) on 5 May 1995. Right: temperature differences (occultation - radiosonde or ECMWF). Figure from *Kursinski et al.* [1996]. (b) Map showing typical locations of COSMIC soundings (green diamonds) and radiosonde launch sites (red circles) over a 24 h period. Figure from *https://www2.ucar.edu/news/cosmic-visuals-multimedia-gallery* .

Although the GPS-RO data are provided on a 100 m vertical grid, the effective resolution of the occultations varies between ∼100 m and ∼1 km [*Kursinski et al.*, 1997; *Sokolovskiy et al.*, 2006; *Wickert et al.*, 2001]. The vertical resolution of the occultations is increased in regions where the stratification of the atmosphere changes, like the top of the boundary layer or the tropopause: i.e. the resolution is highest where it is most needed [*Kursinski et al.*, 1997]. In regions of the atmosphere with constant stratification like the middle stratosphere, the resolution of GPS-RO is typically 1.4 km [*Kursinski et al.*, 1997]. The vertical resolution of the occultations might improve in the future, since the theoretical limit in vertical resolution for the GPS-RO technique is ∼60 m [*Gorbunov et al.*, 2004]. In the next paragraphs the GPS-RO technique is briefly explained:

The vertical scanning of the atmosphere is enabled by the relative motion between the Global Positioning System satellites that emit radio waves and the satellites that receive this signal at a lower orbit, after the signal has been refracted by its pass through an atmospheric layer, which has a refractive index depending on its density.

The GPS constellation consists of 24 satellites orbiting at 20.200 km altitude with a 55° inclination. The different satellite missions to measure the radio signal occultation are low earth orbiters (LEO), at ~800 km altitudes and inclinations of ~70°.

The refraction of the GPS radio signal by an atmospheric layer can be characterized by the bending angle (α), i.e. the change in direction between the emitted GPS radio signal and the same signal received by the LEO satellite, as shown in Figure 2.2.

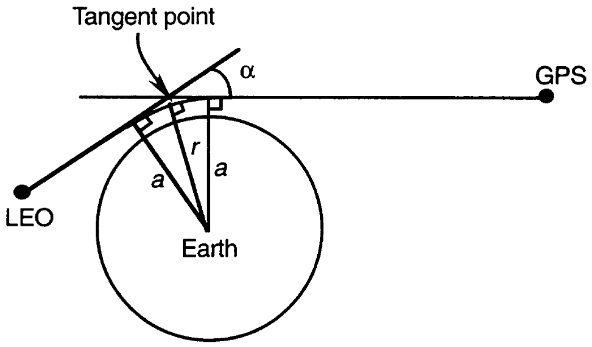

Fig. 2.2 Schematic of the LEO and GPS satellites, their occultation geometry and how the bending angle α is defined. Figure from *Kursinski et al.* [1996].

From the bending angles, profiles of atmospheric refractivity are obtained (see *Kursinski et al.* [1997] for the detailed method). Refractivity (N) is a function of different atmospheric parameters:

$$N = 77.6 \cdot p/T + 3.73 \times 10^5 \cdot e/T^2 - 4.03 \times 10^7 \cdot n_e/f^2$$

as represented in the formula above: p (pressure in hPa), T (temperature in Kelvin), e (water vapor pressure in hPa) and n_e (electron density as electron number per cubic meter). f is the frequency of the GPS carrier signal in Hz. N can be used to derive profiles of electron density in the ionosphere, temperature in the stratosphere, and temperature and water vapor in the troposphere. N depends on the atmosphere's density, and the vertical gradient in N defines the vertical resolution of the GPS-RO measurements, which is why it increases towards the surface and has peaks at stratification discontinuities like the top of the boundary layer and the tropopause [*Kursinski et al.*, 1997].

Thanks to the high amount of occultations and their global coverage, the assimilation of GPS-RO observations has had a major impact in both reanalysis and numerical weather prediction systems, having improved the representation of upper tropospheric and stratospheric temperatures. Although GPS-RO data are not the largest observation source (satellite radiances), they do have the highest assimilation rate among datasets in the ERA-Interim reanalysis [*Poli et al.*, 2010], (60-65 ٪ of the observations are assimilated, compared to a 50 ٪ rate of assimilation for radiosondes); and GPS-RO data are among the top influencers on analyses and forecasts in the ECMWF numerical weather prediction system, especially between 10-20 km altitude [*Cardinali and Healy*, 2014]. ERA-Interim and ECMWF assimilate GPS-RO data since the end of 2006.

In this thesis, GPS-RO profiles from the COSMIC mission [*Anthes et al.*, 2008] for the years 2007-2013 are used. Occasionally, earlier missions CHAMP [*Wickert et al.*, 2001] and GRACE [*Beyerle et al.*, 2005], which provide less observations (around 200 profiles/day together) are used for 2002-2006. Less than 1 ٪ of the profiles is rejected by a preliminary quality control: profiles with unphysical temperatures or N^2 values (temperature <-150°C, >150°C or $N^2 > 100 \times 10^{-4} s^{-2}$) or those where the tropopause was not found were excluded to avoid unrealistic temperature gradients and/or TIL location.

2.1.2 ERA-Interim reanalysis

The ERA-Interim reanalysis uses the ECMWF operational forecast model from early 2007 (IFS Cycle 31r2), which has 60 vertical model levels with the top at 0.1 hPa ($\sim$65 km) altitude, a vertical resolution of 700-800 m near the extratropical tropopause and a T255 ($\sim$80 km) horizontal grid [*Dee et al.*, 2011]. ERA-Interim uses four-dimensional variational assimilation (4D-Var, e.g. *Rabier et al.* [2000]) to fit its atmospheric models to observations (see *ECMWF* [2007b] for an in-depth description).

In sections 3 and 4, ERA-Interim data is used to provide information about the near-tropopause situation of winds and geopotential height, in order to calculate relative vorticity and horizontal divergence, and discern troughs and ridges (cyclones-anticyclones). In the extratropics, the 200 hPa level is chosen to compare to earlier literature [*Randel and Wu*, 2010; *Randel et al.*, 2007a]; while in the tropics the 100 hPa is the closest standard pressure level to the tropopause which is between 100-85 hPa throughout the year [*Kim and Son*, 2012]. Also, vertical profiles of mean zonal winds are used. These data are used to complement the TIL diagnostics from GPS-RO (see section 2.2).

In section 5, the TIL produced by ERA-Interim is studied, so additional data are used: surface geopotential, surface pressure, the hybrid coordinates of the model levels (L60 in the reanalysis, L91 in the operational system), and the temperature and specific humidity at the model levels. Also, 4D-Var increments (the difference in the model states before and after data assimilation) of surface pressure, temperature and specific humidity are used. Calculations are done on model levels, without any interpolation to avoid losing vertical resolution. Also in section 5, ERA-Interim is compared to a newer version of the ECMWF operational weather forecast system (IFS Cycle 35r3), which uses the same 4D-Var data assimilation and has 91 vertical model levels with the top at 0.01 hPa (∼80 km) altitude, a 400-500 m vertical resolution near the tropopause and a T1279 (∼16 km) horizontal grid.

2.2 TIL diagnostics

The tropopause detection and TIL diagnostics are done in the same way throughout this thesis. We define the tropopause height (TP_z) using the World Meteorological Organization lapse-rate tropopause criterion [*WMO*, 1957], as the point in the vertical profile where the mean lapse-rate is lower than 2 K/km in all points between the tropopause and 2 km above. From the GPS-RO temperature profiles, vertical profiles of static stability are calculated as the Brunt-Väisälä frequency squared (N^2, s^{-2}):

$$N^2 = (g/\Theta) \cdot (\partial\Theta/\partial z)$$

where g is the gravitational acceleration, and Θ the potential temperature. The vertical profiles of temperature and N^2 are averaged with the tropopause level as reference. TIL strength is calculated as the maximum static stability value (N^2_{max}) above the tropopause level, like the peak in Fig. 1.1 but for individual profiles. This TIL strength measure is commonly used [*Birner et al.*, 2006; *Erler and Wirth*, 2011; *Wirth and Szabo*, 2007], because it makes TIL strength independent of its distance from the tropopause (N^2_{max} is not always at the exact same distance from the tropopause) and N^2 is a physically relevant quantity.

In the tropics, given the strong negative lapse-rate found above the tropopause near the equator, the lapse-rate tropopause nearly coincides with the cold-point tropopause most of the time. Earlier studies did not find substantial differences in their results applying different tropopause definitions [*Grise et al.*, 2010; *Wang et al.*, 2013], so the use of the WMO lapse-rate criterion to define the tropopause in the tropics in this thesis is not problematic.

In the extratropics, there exists a cyclone-anticyclone asymmetry between the lapse-rate tropopause (based on temperature gradient) and the dynamical tropopause (based on a threshold of 2 potential vorticity units, 2 PVU), with increasing differences towards stronger cyclonic circulation [*Wirth*, 2001]. We allow our algorithm to find the N^2_{max} up to 3 km above the tropopause, although it is almost always found in the first 1-2 km.

This way, the TIL diagnostics are flexible enough to work at all latitudes and synoptic conditions. Given the high observation density of COSMIC GPS-RO profiles, daily maps or snapshots of TIL strength can be obtained by gridding N^2_{max} depending on the location of the corresponding profile. Similarly, tropopause-based temperature and N^2 profiles can be gridded choosing the profiles closest to the longitude-latitude grid-point on a daily basis.

The methodology to grid GPS-RO profiles was developed by *Randel and Wu* [2005] and consists of defining a regular longitude grid at a certain latitude band and, for each grid point, selecting the GPS-RO profiles within a given distance to this point to derive an average vertical profile at the grid point. Therefore distance depending weights are assigned to each selected GPS-RO profile. The weighting function is Gaussian-shaped, decaying exponentially with increasing distance of the GPS-RO profile from the grid point.

2.3 Wave signal extraction

One of the goals of this thesis is to quantify the transient wave modulation of the tropopause, a novel mechanism for TIL enhancement as explained in section 1.3 (Fig. 1.7), which could play an important role in the dynamical formation/maintenance/enhancement of the TIL. In order to obtain wave anomalies like in Fig. 1.7, we make use of space-time bandpass filters that are applied to the gridded GPS-RO profiles. Subsections 2.3.1 and 2.3.2 are shortened extracts of the methodology to filter equatorial and extratropical waves, respectively, from the papers included in sections 3 and 4.2.

2.3.1 Tropics

Equatorial waves are the zonally and vertically propagating, equatorially trapped solutions of the ’shallow water’ equations [*Lindzen*, 1967; *Matsuno*, 1966]. Each wave type (Kelvin, Rossby, the different modes of Inertia-Gravity waves) has a unique dispersion curve in the wavenumber-frequency domain, given its mode n and equivalent depth h.

Wheeler and Kiladis [1999] found that the equatorial outgoing longwave radiation (OLR) power had spectral signatures that were significantly above the background at certain wavenumber-frequency domain regions, matching with the dispersion curves of the different equatorial wave types and the MJO, as shown in Fig. 2.3 from their paper.

Our method to filter waves is similar to that of *Wheeler and Kiladis* [1999], but analyzes temperature and N^2 at all levels between 10-35 km altitude instead of OLR. For filtering, the data must be periodic in longitude and time and cover all longitudes of the equatorial latitude band. Therefore, the COSMIC GPS-RO profiles [*Anthes et al.*, 2008] need to be put on a

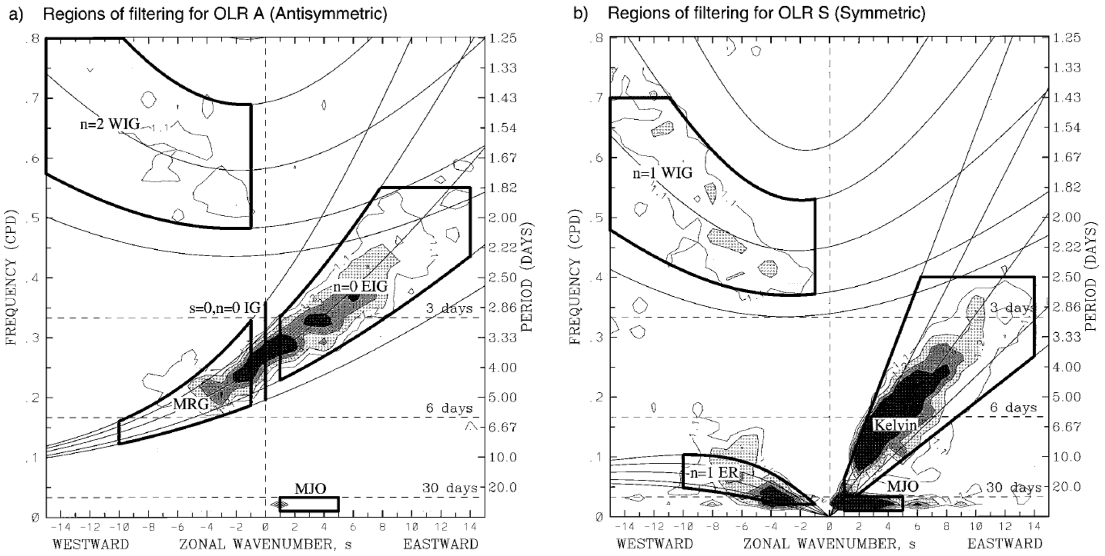

a) Regions of filtering for OLR A (Antisymmetric)

b) Regions of filtering for OLR S (Symmetric)

Fig. 2.3 Regions of the wavenumber-frequency domain with power spectrum above the background, thin contours starting at 1.1 and shading above 1.2. (a) antisymmetric component, (b) symmetric component of the OLR spectrum. The wave dispersion curves are for equivalent depths h = 8, 12, 25, 50 and 90 m. Thick-lined boxes indicate the regions of the wavenumber-frequency domain used for filtering. Figure from *Wheeler and Kiladis* [1999].

regular longitude grid on a daily basis. The filter settings are fairly similar to those shown in Fig. 2.3, although we allow for larger equivalent depths to account for the faster and not convectively coupled waves modes that can exist near the tropopause and throughout the stratosphere.

At a certain latitude band, and for each vertical level (0.1 km vertical spacing), the data consists of a longitude-time array, which is detrended and tapered in time. Then, a space-time bandpass filter is applied using a two-dimensional Fast Fourier Transform. This is done using the freely available ’kf-filter’ NCL function [*Schreck*, 2009].

The Fast Fourier Transform separates, in the longitude direction, all the zonal structure of temperature anomalies into a sum of harmonics of different wavenumbers. The same is done in the time dimension: each wavenumber has to oscillate in time with a certain frequency within the region defined for the bandpass filter, in order to be captured by it. If waves are present, which are theoretically defined by space-time harmonics, their filtered signal is outstanding compared to the (unavoidable to filter) background noise, which appears as a continuum of low-amplitude fluctuations [*Wheeler and Kiladis*, 1999].

Combining the filtered signals of each vertical level, which are filtered independently, will give the longitude-height wave anomaly structures that we are looking for as in the idealized representation in Fig. 1.7. This method is adapted for the extratropics in a simplified way, as explained next.

2.3.2 Extratropics

The extratropical wave modes differ greatly from those at the equator: they are not equatorially trapped and can propagate in any direction, the Coriolis parameter has to be taken into account since it is non-zero outside the equator, and the zonal wind regimes in the extratropics are much more variable than the equatorial ones. Background winds affect the propagation of waves, by Doppler-shifting their dispersion relations or even precluding their propagation, therefore it is of special importance to take them into account in the extratropics.

We make a comparison of the dispersion curves of the extratropical Rossby wave under different background zonal wind regimes in Figure 2.4. The Rossby wave dispersion relation is defined as the most common form of large-scale wave disturbance found in the extratropics: a planetary wave forced from the troposphere, and propagating vertically and zonally in a quasi-geostrophic flow. Assuming N^2 and background mean zonal winds ($\bar{U}$) to be constant, and no meridional propagation for simplicity, the following dispersion relation can be obtained (following *Andrews et al.* [1987], see chapter for Linear Wave Theory):

$$w = s\bar{U} - s\beta[s^2 + f^2/gh]^{-1}$$

where w is the frequency, s is the zonal wavenumber, f the Coriolis parameter, β its meridional derivative at a certain latitude (the Beta-plane approximation), g the gravity acceleration and h the equivalent depth. Since we assume no meridional propagation for simplicity, the meridional wavenumber is set to zero so it is absent in this formula (compared to *Andrews et al.* [1987]). The term ($s\bar{U}$) accounts for the Doppler-shifting of the dispersion relation by the background zonal winds; and the (f^2 /gh) term is an approximation to account for the vertical propagation of the wave.

Figure 2.4 shows how the dispersion curve of a Rossby wave changes depending on its equivalent depth (different line types), and the background zonal mean winds (zero winds black, blue for easterlies, red for westerlies, see specific arrows outside the diagram). Note that each dispersion curve is not valid for the entire year for the Rossby wave, only for the seasons with similar background $\bar{U}$.

The dispersion relations in Fig. 2.4 show the difficulty of defining a wave type in the extratropics: the dispersion curve for a given wave type (idealized Rossby wave in this case) can be in every possible place within the wavenumber-frequency domain, depending on the background winds. Therefore, it is impossible to define one filter to extract Rossby waves

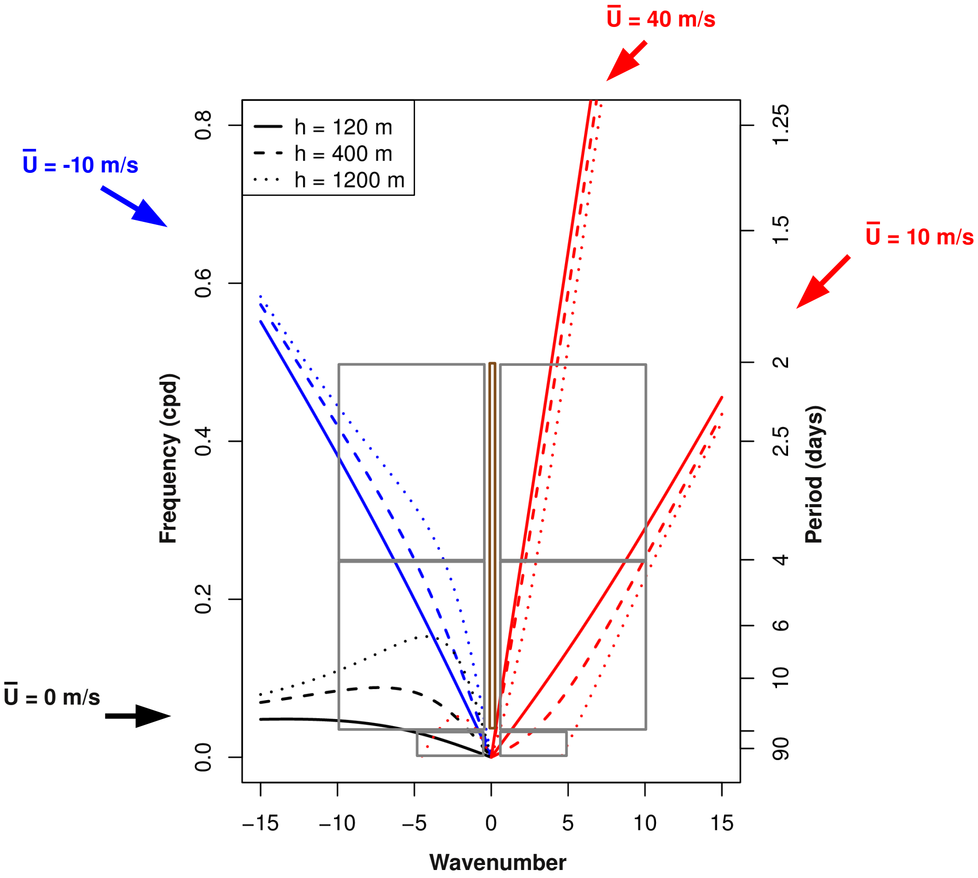

Fig. 2.4 Examples of dispersion curves for forced planetary waves at 50°N under different mean zonal wind regimes (line colors, winds specified outside the diagram), and differentiating equivalent depths (line type, top-left box). Filter bounds in the wavenumber-frequency domain are shown as grey boxes (brown for wavenumber zero). Figure from *Pilch Kedzierski et al.* [2016b].

that is valid for the entire time period (2007-2013) and that could be used at all levels between 5 and 35 km altitude.

Instead of defining certain dispersion curves, we use wide boxes in the wavenumber-frequency domain, only differentiating eastward-westward propagating oscillations with respect to the ground and their periods (faster 2-4 day waves; slower 4-25 day waves; and 30-96 day or quasi-stationary waves), which are displayed as the six grey boxes in Fig. 2.4. We also define a seventh filter for wavenumber zero (s = 0, brown box in the middle of the diagram in Fig. 2.4) for completeness. This way, the Rossby waves will be captured by one or another filter, independently of the background zonal winds.

With this method we prioritize knowing the total effect of planetary and synoptic-scale extratropical waves on the TIL, at the cost of not differentiating baroclinic, barotropic, standing, traveling (etcetera) wave modes. We find this to be a fair compromise, since our study targets TIL modulation and enhancement by extratropical waves, and not to disclose particular properties of these waves.

The space-time filtering methodology has never been applied to extract extratropical waves before due to the variability of background zonal winds which precludes defining a specific dispersion curve for the waves. By simplifying the methodology, the novel procedure developed during the doctoral work, as explained within this subsection, allows the extraction of the combined signal from planetary and synoptic-scale extratropical waves.

Next, sections 3, 4 and 5 will show the main results of this thesis, as reprints of the scientific publications produced during the doctoral work.

3 The Tropical Tropopause Inversion Layer: Variability and Modulation by Equatorial Waves

This chapter is a reprint of the article of the same name under review in *Atmospheric Chemistry and Physics Discussions*. It investigates the daily variability of the horizontal and vertical N^2 structures in the tropics, the relationship of stronger TIL with near-tropopause divergent flow, and how the QBO affects the TIL and also forms a secondary N^2 maximum below the zero-wind line.

The TIL modulation and enhancement by equatorial waves is quantified for the first time, comparing the relative roles of Kelvin, Rossby, IGWs and the MJO. Lastly, the remaining TIL without the equatorial wave signal is shown.

Citation:

Pilch Kedzierski, R., K. Matthes, and K. Bumke (2016a), The tropical tropopause inversion layer: variability and modulation by equatorial waves, *Atmospheric Chemistry and Physics Discussions*, pp. 1-31, doi:10.5194/acp-2016-178, (in review).

Author contributions to this publication:

- R. Pilch Kedzierski initiated the study, designed the method, did the analysis, produced all the figures and wrote the manuscript.

- K. Matthes contributed with ideas and discussions on the analysis, and commented the manuscript.

- K. Bumke contributed with ideas and discussions on the analysis, and commented the manuscript.

Manuscript prepared for Atmos. Chem. Phys.
with version 2015/04/24 7.83 Copernicus papers of the LaTeX class copernicus.cls.
Date: 28 July 2016

The Tropical Tropopause Inversion Layer: Variability and Modulation by Equatorial Waves

Robin Pilch Kedzierski[1], Katja Matthes[1,2], and Karl Bumke[1]

[1]Marine Meteorology Department, GEOMAR Helmholtz Centre for Ocean Research Kiel, Kiel, Germany.

[2]Faculty of Mathematics and Natural Sciences, Christian-Albrechts-Universität zu Kiel, Kiel, Germany.

Correspondence to: Robin Pilch Kedzierski (rpilch@geomar.de)

Abstract.

The Tropical Tropopause Layer (TTL) acts as a 'transition' layer between the troposphere and the stratosphere over several kilometers, where air has both tropospheric and stratospheric properties. Within this region, a fine-scale feature is located: the Tropopause Inversion Layer (TIL), which consists of a sharp temperature inversion at the tropopause and the corresponding high static stability values right above, which theoretically affect the dispersion relations of atmospheric waves like Rossby or Inertia-Gravity waves and hamper stratosphere-troposphere exchange (STE). Therefore, the TIL receives increasing attention from the scientific community, mainly in the extratropics so far. Our goal is to give a detailed picture of the properties, variability and forcings of the tropical TIL, with special emphasis on small-scale equatorial waves and the QBO.

We use high-resolution temperature profiles from the COSMIC satellite mission, i.e. $\sim$2000 measurements per day globally, between 2007 and 2013, to derive TIL properties and to study the fine-scale structures of static stability in the tropics. The situation at near tropopause level is described by the 100hPa horizontal wind divergence fields, and the vertical structure of the QBO is provided by the equatorial winds at all levels, both from the ERA-Interim reanalysis.

We describe a new feature of the equatorial static stability profile: a secondary stability maximum below the zero wind line within the easterly QBO wind regime at about 20-25km altitude, which is forced by the descending westerly QBO phase and gives a double-TIL-like structure. In the lowermost stratosphere, the TIL is stronger with westerly winds. We provide the first evidence of a relationship between the tropical TIL strength and near-tropopause divergence, with stronger (weaker) TIL with near-tropopause divergent (convergent) flow, a relationship analogous to that of TIL strength with relative vorticity in the extratropics.

To elucidate possible enhancing mechanisms of the tropical TIL, we quantify the signature of the different equatorial waves on the vertical structure of static stability in the tropics. All waves show, on average, maximum cold anomalies at the thermal tropopause, warm anomalies above, and a net TIL enhancement close to the tropopause. The main drivers are Kelvin, inertia-gravity and Rossby

waves. We suggest that a similar wave modulation will exist at mid and polar latitudes from the extratropical wave modes.

1 Introduction

The Tropopause Inversion Layer (TIL) is a narrow region characterized by temperature inversion and enhanced static stability located right above the tropopause. This fine-scale feature was discovered by tropopause-based averaging of high-resolution radiosonde measurements by Birner et al. (2002) and Birner (2006). Satellite Global Positioning System radio occultation observations (GPS-RO) show that the TIL is present globally (Grise et al., 2010).

Static stability is a parameter used in a number of wave theory approximations, thus affecting the dispersion relations of atmospheric waves like Rossby or Inertia-Gravity waves (Birner, 2006; Grise et al., 2010). Also, static stability suppresses vertical motion and correlates with sharper trace gas gradients, inhibiting the cross-tropopause exchange of chemical compounds (Hegglin et al., 2009; Kunz et al., 2009; Schmidt et al., 2010). For these reasons, the TIL attracts increasing interest from the scientific community.

There is a considerable body of research about the TIL in the extratropics, establishing the TIL as an important feature of the extratropical upper-troposphere and lower-stratosphere (Gettelman et al., 2011). In the tropics, the transition between the troposphere and the stratosphere is considered to happen over several kilometers, dynamically and chemically (Fueglistaler et al., 2009; Gettelman and Birner, 2007), but less is known about the tropical TIL, as the following review will show.

In the extratropics, climatological studies have shown that the TIL reaches maximum strength during polar summer (Birner, 2006; Randel et al., 2007; Randel and Wu, 2010; Grise et al., 2010), whereas the TIL within anticyclones in mid-latitude winter is of the same strength or even higher from a synoptic-scale point of view (Pilch Kedzierski et al., 2015). Several mechanisms for extratropical TIL formation/maintenance have been studied: water vapor radiative cooling below the tropopause (Randel et al., 2007; Hegglin et al., 2009; Kunz et al., 2009; Randel and Wu, 2010), dynamical heating above the tropopause from the downwelling branch of the stratospheric residual circulation (Birner, 2010), tropopause lifting and sharpening by baroclinic waves and their embedded cyclones-anticyclones (Wirth, 2003, 2004; Wirth and Szabo, 2007; Son and Polvani, 2007; Randel et al., 2007; Randel and Wu, 2010; Erler and Wirth, 2011), and the presence of small-scale gravity waves (Kunkel et al., 2014). A high-resolution model study by Miyazaki et al. (2010a, b) suggests that radiative effects dominate TIL enhancement in polar summer whereas dynamics are the main drivers in the remaining latitudes and seasons.

On the other hand, very little research has focused on the tropical TIL. Bell and Geller (2008) showed the TIL from one tropical radiosonde station, and Wang et al. (2013) reported a slight weakening of the tropical TIL between 2001-2011. Grise et al. (2010) included the horizontal and vertical variability of the tropical TIL in their global study about near-tropopause static stability, which is so far the most detailed description of the TIL in the tropics. They found the strongest TIL centered at the equator in the layer 0-1km above the tropopause, peaking during NH winter. This agrees well with the seasonality and location of tropopause sharpness as described later by Son et al. (2011) and Kim and Son (2012). The horizontal structures in seasonal mean TIL in the tropics are reminiscent of the equatorial stationary wave response associated with climatological deep convection (Grise et al., 2010; Kim and Son, 2012). Grise et al. (2010) also noted that static stability is enhanced in the layer 1-3km above the tropopause during the easterly phase of the quasi-biennial oscillation (QBO).

Equatorial waves influence the intraseasonal and short-term variability of the temperature structure near the tropical tropopause (Fueglistaler et al., 2009). Kelvin waves and the Madden-Julian oscillation (MJO) (Madden and Julian, 1994) were reported as the dominant modes of temperature variability at the tropopause region (Kim and Son, 2012). Equatorial waves cool the tropopause region (Grise and Thompson, 2013), and also produce a warming effect above it (Kim and Son, 2012). This wave effect forms a dipole that can sharpen the gradients that lead to TIL enhancement, but no study has quantified this effect so far.

Our study aims to describe the tropical TIL, its variability and forcings in detail, in order to increase the knowledge about its properties and highlight this sharp and fine-scale feature within the tropical transition layer between the troposphere and the stratosphere. Section 2 will show the datasets and methods used in our analyses. Section 3 will describe the vertical and horizontal structure and day-to-day variability of the TIL, its relationship with near-tropopause divergence, and the influence of the QBO on the vertical structure of static stability and TIL strength in particular. In section 4 we quantify the signature of the different equatorial waves and their effect on the mean temperature and static stability profiles in tropopause-based coordinates. Section 5 will discuss the applicability of our results with equatorial wave modulation to the extratropical TIL, given the different wave spectrum in the extratropics, and section 6 sums up the results.

2 Data and Methods

2.1 Datasets

We analyze temperature profiles from GPS radio occultation (GPS-RO) measurements which are provided at a 100m vertical resolution, from the surface up to 40km altitude, comparable to high-resolution radiosonde data. Although the effective physical resolution of GPS-RO retrievals is of $\sim$1km, it improves in regions where the stratification of the atmosphere changes, such as the tropopause and the top of the boundary layer, i.e. the vertical resolution is highest where it is most needed (Kursinski et al., 1997). The advantage of GPS-RO is based on its global coverage, high sampling density of $\sim$2000 profiles/day, and weather-independence. We mainly use data from the COSMIC satellite mission (Anthes et al., 2008) for the years 2007-2013. For Figure 1 only, we added two earlier GPS-RO satellite missions: CHAMP (Wickert et al., 2001) and GRACE (Beyerle et al., 2005), which provide less observations (around 200 profiles/day together) for 2002-2007.

The situation at near-tropopause level is retrieved from the ERA-Interim reanalysis (Dee et al., 2011). We make use of horizontal wind divergence and geopotential height fields at 100hPa on a 2.5°×2.5° longitude-latitude grid and 6-hourly time resolution, and also daily-mean vertical profiles of the zonal wind at the equator, for the time period 2007-2013. We choose the 100hPa level because it is the standard pressure level from ERA-Interim that is closest to the climatological tropopause in the tropics (96-100hPa in summer, 86-88hPa in winter, Kim and Son (2012)). Tropical winds near the tropopause in ERA-Interim differ from observations slightly more than in the extratropics, but still are of good quality (Poli et al., 2010; Dee et al., 2011), and the variability of horizontal divergence is in balance with temperatures, which are constrained by GPS-RO in the UTLS.

2.2 TIL Strength Calculation

We define the tropopause height (TP_z) using the WMO lapse-rate tropopause criterion (WMO, 1957). Given the strong negative lapse-rate found above the tropopause near the equator, the lapse-rate tropopause nearly coincides with the cold-point tropopause most of the time. This is in agreement with earlier studies, which did not find substantial differences in their results applying different tropopause definitions (Grise et al., 2010; Wang et al., 2013). From the GPS-RO temperature profiles, vertical profiles of static stability are calculated as the Brunt-Väisälä frequency squared (N^2 [s^{-2}]):

$$N^2 = (g/\Theta) \cdot (\partial\Theta/\partial z)$$

where g is the gravitational acceleration, and Θ the potential temperature. Profiles with unphysical temperatures or N^2 values (temperature <-150°C, >150°C or N^2 >$100\times10^{-4}s^{-2}$) and those where the tropopause cannot be found have been excluded. TIL strength (sTIL) is calculated as the maximum static stability value (N^2_{max}) above the tropopause level. This sTIL measure is commonly used (Birner et al., 2006; Wirth and Szabo, 2007; Erler and Wirth, 2011; Pilch Kedzierski et al., 2015), because it makes sTIL independent of its distance from the tropopause and N^2 is a physically relevant quantity. Our algorithm searches for N^2_{max} in the first 3km above TP_z, but most often finds it in the first kilometer.

2.3 Mapping of TIL Snapshots

The procedure to derive daily TIL snapshots in this study is similar to the method by Pilch Kedzierski et al. (2015), but with a longitude-latitude projection.

The daily TIL snapshots were estimated at a 5° longitude-latitude grid between 30°S-30°N. For each grid point we calculate the mean N^2_{max} from all GPS-RO profiles within +-12.5° longitude-latitude to account for the lower GPS-RO observation density in the tropics compared to the extratropics (Son et al., 2011). This setting avoids gaps appearing in the maps, and smooths out undesired small-scale features that cannot be captured with the current GPS-RO sampling.

We also produce similar maps of 100hPa horizontal wind divergence. For a fair comparison with the TIL snapshots, we equal the spatial scale and follow the same method, but instead of averaging N^2_{max} values, we use the collocated divergence of each GPS-RO profile: the value from the nearest ERA-Interim grid point and 6h time period to each observation. Examples of TIL snapshots can be found in Figure 2 (section 3.1.2). If plotted at full horizontal resolution, divergence would show small-scale features superimposed over the synoptic-to-large scale structures in Fig. 2, making the comparison with N^2_{max} more difficult.

2.4 Wavenumber-Frequency Domain Filtering

Our purpose is to extract the temperature and N^2 signature of the different equatorial wave types on the zonal mean vertical profiles. For this, we follow Wheeler and Kiladis (1999), that studied equatorial wave signatures on the outgoing longwave radiation (OLR) spectrum observed from satellites by wavenumber-frequency domain filtering. Wheeler and Kiladis (1999) give an in-depth description of the theoretical and mathematical background of the filtering methods.

Theoretically, the equatorial wave modes are the zonally and vertically propagating, equatorially trapped solutions of the 'shallow water' equations (Matsuno, 1966; Lindzen, 1967) characterized by four parameters: meridional mode number (*n*), frequency (*v*), zonal planetary wavenumber (*s*) and equivalent depth (*h*). Each wave type (Kelvin, Rossby, the different modes of Inertia-Gravity waves) has a unique dispersion curve in the wavenumber-frequency domain, given its mode *n* and equivalent depth *h*.

Wheeler and Kiladis (1999) found that the equatorial OLR power had spectral signatures that were significantly above the background. The signature's regions in the wavenumber-frequency domain match with the dispersion curves of the different equatorial wave types. Also, they found signatures outside of the theoretical wave dispersion curves that have characteristics of the Madden-Julian oscillation (MJO) (Madden and Julian, 1994).

Our method is similar to that of Wheeler and Kiladis (1999), but analyzes temperature and N^2 at all levels between 10-35km altitude instead of OLR. For filtering, the data must be periodic in longitude and time and cover all longitudes of the equatorial latitude band. Therefore, the COSMIC GPS-RO profiles (Anthes et al., 2008) need to be put on a regular longitude grid on a daily basis. We explain how this is done in the follwing section (2.4.1). More details about our proceeding with the filter, and the differences from Wheeler and Kiladis (1999) can be found in section 2.4.2. Note that this method is only used in Figs. 5 and 6 (section 4).

2.4.1 Gridding of GPS-RO profiles

The COSMIC GPS-RO temperature profiles between 10°S-10°N are gridded daily on a regular longitude grid with a 10° separation. At each grid point, the profiles of that day within 10°S-10°N and +-5° longitude are selected to calculate a tropopause-based weighted average temperature profile and the corresponding N^2 vertical profile:

$$T_{grid}(\lambda, Z_{TP}, t) = \sum_i w_i T_i(\lambda, Z_{TP}, t) / \sum_i w_i$$

$$N^2_{grid}(\lambda, Z_{TP}, t) = \sum_i w_i N^2_i(\lambda, Z_{TP}, t) / \sum_i w_i$$

where λ is longitude, Z_{TP} is the height relative to the tropopause and t is time. The weight w_i is a Gaussian-shape function that depends on the distance of the GPS-RO profile from the grid center, taking longitude, latitude and time (distance from 12UTC):

$w_i = exp(-[(D_x/5)^2 + (D_y/10)^2 + (D_t/12)^2])$, where D are the distances in °longitude (x subscript), °latitude (y) and hours (t). The maximum distance allowed from the grid point in each dimension is: 5° longitude, 10° latitude, and 12 hours from 12UTC, respectively.

The gridded tropopause height (λ,t) is calculated with the same weighting of all profiles' tropopauses. The gridded temperature and N^2 profiles are shifted, as the last step, from the tropopause-based vertical scale onto a ground-based vertical scale from 10km to 35km altitude, obtaining a longitude-height array for each day for 2007-2013.

Most often 2-3 profiles are selected for averaging at a grid point with these settings, although one GPS-RO profile is sufficient to estimate a grid point. However, in 6.5% of the cases the algorithm does not find any profile. To fill in the gaps, the longitude range to select the profiles is incremented to +-10° instead of +-5°, which still leaves a 0.8% of empty grid-points. For this minority, profiles are selected within +-1day and +-15° longitude. In all cases the weighting function remains the same. These exceptions are for a very small portion of the gridded data, and therefore do not affect the retrieved wave signatures after filtering.

Our method is essentially an update from Randel and Wu (2005). It is adapted for the higher number of GPS-RO retrievals of the COSMIC mission compared to its predecessors CHAMP and GRACE: Randel and Wu (2005) used a 30° longitude grid and selected profiles for +-2days, while we use 10° spacing and profiles of the same day. This leads to increased zonal resolution, as well as a minimized temporal smoothing. Another difference is that we do the averaging in tropopause-based coordinates to avoid smoothing the TIL, and also use latitude differences in the weighting function. Compared to earlier studies that filtered equatorial waves using GPS-RO data (Randel and Wu, 2005; Kim and Son, 2012), our daily fields with barely any running mean allow the analysis of waves with higher frequencies and wavenumbers (i.e. a wide part of the inertia-gravity wave spectrum) that otherwise are smoothed out and not accounted for.

2.4.2 Filter Settings

With the longitude-height-time array of gridded temperature and N^2 profiles obtained according to section 2.4.1, we proceed with the filtering in the wavenumber-frequency domain as follows. For each vertical level (from 10km to 35km height with 0.1km vertical spacing), a longitude-time array is retrieved, detrended and tapered in time. Then, a space-time bandpass filter is applied using a two-dimensional Fast Fourier Transform. This is done using the freely available 'kf-filter' NCL function (Schreck, 2009).

The bandpass filter bounds in the wavenumber-frequency domain are defined for the following wave types: Kelvin waves, Rossby waves, and all modes of Inertia-Gravity waves: *n* = (0,1,2). We separate westward-propagating (negative wavenumber *s*) Inertia-Gravity waves (WIG_n), the eastward-propagating ones (positive s, EIG_n), and the zonal wavenumber zero ($_{s=0}IG_n$) in the analysis. Our WIG_n category includes the Mixed Rossby-Gravity wave modes for *n* = 0. Including the MJO band (which does not belong to any theoretical dispersion curve), we end up with 12 different bandpass filters that are applied to the longitude-time array of gridded temperature and N^2, at each vertical level separately. The exact filter bounds are listed in Table 1. They are similar to the ones used by Wheeler and Kiladis (1999) and take into account the faster and not convectively coupled Kelvin waves found by Kim and Son (2012) in the tropopause temperature variability spectrum. We also allow faster WIG_0 and Rossby waves in the corresponding filters. Note that the filter bounds defined in Table 1 never overlap in the wavenumber-frequency domain. After filtering, we obtain a daily longitude-height section with the 12 waves' temperature and N^2 signatures. We stress that the temperature and N^2 fields are filtered independently at each vertical level.

3 Structure and Variability of the Tropical TIL

3.1 Vertical and Horizontal Structures

3.1.1 Temporal variability of the vertical N^2 profile

We first focus on the variation of the equatorial N^2 profiles over time. Figure 1 shows the daily evolution of the equatorial (5°S-5°N) zonal mean N^2 profile between 2002-2013, with zonal wind contours superimposed (black westerlies, and dashed easterlies), and a grey tropopause line. The years 2002-2006 appear noisier because the number of observations from the CHAMP (Wickert et al., 2001) and GRACE (Beyerle et al., 2005) satellite missions is about 10 times less than the amount of profiles from COSMIC (Anthes et al., 2008) used between 2007-2013. Therefore local anomalies have a bigger impact on the zonal mean vertical profile during 2002-2006.

The tropopause height in Fig. 1 has a seasonal cycle with a generally higher (lower) tropopause and higher (lower) values of N^2 right above it during the NH winter (summer) months, in agreement with the seasonal cycle of the tropopause (Yulaeva et al., 1994) and the tropical TIL climatological seasonal cycle described by Grise et al. (2010).

The daily evolution of N^2 also shows a secondary maximum below the zero wind line (bold black), at the easterly side of the descending westerly QBO phase, between 20-25km height. The zero wind line (of the descending westerly QBO phase) usually crosses the ∼20km level in summer, while crossing the ∼25km level in the earlier winter. This happens in 2002, 2004, 2006, 2008 and 2013, with the exception of 2010 when the zero wind line crosses ∼25km in summer. The enhanced N^2 is present under the zero wind line all the way from 35km altitude, but it is most evident in winter and spring (∼25km altitude and below). In winter and spring the secondary maximum of N^2 (red, about $8\times10^{-4}s^{-2}$) is close to the TIL strength (brown, about $9\times10^{-4}s^{-2}$ in the first kilometer above the tropopause), forming a double-TIL-like structure in static stability. However, this secondary maximum in N^2 shall not be viewed as a second TIL since it is quite far away from the tropopause. In the case of 2010, when the secondary maximum appears in summer it is much weaker, probably due to the fact that N^2 is generally weaker throughout the whole lower stratosphere in summer (Fig. 1). We also note that during the descending easterly QBO phase N^2 is enhanced above the zero wind line, again within the easterly wind regime. This time, the enhanced N^2 is much weaker than in the descending westerly QBO phase case, and only discernible in the lowermost stratosphere.

Grise et al. (2010) found a significant correlation of enhanced N^2 in the layer 1-3km above the TP when easterlies were present in the lowermost stratosphere, while no clear correlation was found in the 0-1km layer above the TP. From Fig. 1 we deduce that this correlation of the 1-3km layer originates in the secondary N^2 maximum found below the zero wind line of the descending westerly QBO (or above the zero line of the descending easterly QBO to a lesser degree, within the easterly QBO wind regime in any case). The QBO influence on the TIL, strictly the absolute N^2_{max} that is found in the first kilometer above the TP, is hard to discern in Fig. 1. We investigate this in more detail in the subsection 3.3.

3.1.2 Horizontal structure of TIL strength

Figure 2 shows daily snapshots of TIL strength (sTIL, N^2_{max}) and collocated horizontal wind divergence (see section 2.3) between 30°S-30°N, together with 100hPa geopotential height contours, for four different days: two winter cases (left) and two summer cases (right), as examples representative of the variability in strength and zonal structures of the tropical TIL between 2007 and 2013.

The first remarkable aspect of the tropical TIL is that the magnitude of N^2_{max} is much higher than in the extratropics. Values near the equator vary between 9-15 $\times10^{-4}s^{-2}$ and reach the $20\times10^{-4}s^{-2}$ mark sometimes, compared to a sTIL of 8-10$\times10^{-4}s^{-2}$ generally found in polar summer or within ridges in mid-latitude winter (Pilch Kedzierski et al., 2015). This can be attributed to the background temperature gradient in the lower stratosphere in the tropics, with a strong negative lapse-rate and a higher background lower-stratospheric N^2.

When a dipole of tropopause cooling and warming aloft (needed for TIL formation) is added to this background profile, the potential temperature gradient just above the tropopause increases dramatically, giving the enormous N^2_{max} values observed in Fig. 2.

The peak containing N^2_{max} is very narrow and not always found at the exact same distance from the tropopause. Thus, when a zonal mean N^2 profile is computed, the high N^2_{max} values get slightly smoothed out (Pilch Kedzierski et al., 2015). This is why the N^2 values in the first kilometer above the tropopause in Fig. 1 are lower than in Fig. 2.

As observed by Grise et al. (2010), in Fig. 2 we find that the strongest TIL is almost always centered at the equator, pointing towards equatorially trapped wave modes as TIL enhancers (which we analyze in section 4). When the sTIL zonal structure is compared to 100hPa divergence and geopotential height, it can be observed that higher N^2_{max} is in general near regions of horizontally divergent flow (blue in Fig. 2) and a higher 100hPa surface. This high-low behavior with stronger-weaker TIL highly resembles the cyclone-anticyclone relationship with sTIL found in the extratropics (Randel et al., 2007; Randel and Wu, 2010; Pilch Kedzierski et al., 2015).

So far, Figs. 1 and 2 confirm the vertical/horizontal structures of the TIL and its seasonality from earlier studies Grise et al. (2010); Kim and Son (2012), while reporting new features: the TIL relation with near-tropopause divergence (which we analyze next in section 3.2) and a secondary N^2 maximum above the TIL region driven by the QBO, whose influence on the TIL is analyzed in section 3.3.

3.2 Relationship with Divergence

In this subsection, we have a closer look at the relationship of the zonal structure of the tropical sTIL with its collocated horizontal wind divergence as shown in Fig. 2. For this, we bin sTIL and tropopause height depending on the divergence value collocated with each GPS-RO observation, and make a mean within each divergence bin, as previous studies did with relative vorticity in the extratropics (Randel et al., 2007; Randel and Wu, 2010; Pilch Kedzierski et al., 2015). The resulting divergence versus sTIL diagrams are shown in Figure 3. In both summer and winter (Figs. 3 a, b) sTIL increases with divergence: from 11-12$\times 10^{-4} s^{-2}$ found with convergent flow (negative values) or near-zero divergence, increasing steadily up to almost $15\times 10^{-4} s^{-2}$ with increasingly divergent flow. The sTIL relation with divergence shown in the diagrams from Figs. 3 a and b is analogous to that of relative vorticity versus sTIL in the extratropics from earlier studies (Randel et al., 2007; Randel and Wu, 2010; Pilch Kedzierski et al., 2015). We also note that the N^2_{max} in winter is always slightly higher than in summer for any divergence value, in agreement with the seasonality with stronger TIL in winter from Fig.1 and the climatology by Grise et al. (2010). There is no clear link between a higher tropopause and a stronger TIL. The variation of tropopause height with divergence is very small (see Appendix A, figure A1).

The relation of stronger TIL with divergent flow in Fig. 3 is consistent with the hydrostatic adjustment mechanism over deep convection described by Holloway and Neelin (2007), which results in a colder tropopause and an increased temperature gradient aloft. The hydrostatic adjustment mechanism is a dynamical response to compensate the pressure gradients created by a local tropospheric warming (latent heat release) from convection. The pressure gradients extend above the heating, and ascent and adiabatic cooling act to diminish these pressure gradients with height, cooling the tropopause region above the deep convective tower. Paulik and Birner (2012) showed that this negative temperature signal near the tropical tropopause can be found even a few thousand kilometers away from the convective region. In Fig. 3, we do not differentiate whether divergence is coupled to equatorial waves or not, so any type of convection would be included together for the TIL enhancement with divergent flow. The horizontal structures of sTIL in Fig. 2 can also be shaped by deep convection not related to equatorial waves.

Given the results with divergence from Figures 2 and 3, and the resemblance with the sTIL relationship with relative vorticity in the extratropics, the question arises whether the tropical and extratropical TIL could share the same enhancing mechanism. We postulate an affirmative answer.

The modelling experiments of Wirth (2003, 2004) showed that the stronger TIL in anticyclones in the extratropics was caused by two mechanisms: tropopause lifting and cooling (therefore the higher tropopause with anticyclonic conditions found by Randel et al. (2007); Randel and Wu (2010)); and vertical wind convergence above the anticyclone due to the onset of a secondary circulation between the cyclones and the anticyclones. In the tropics, the tropopause height effect is absent, but there is a clear relationship between sTIL and divergence (Fig. 3a and 3b). Such a horizontally divergent flow is coupled with vertical convergence for continuity reasons. Given that sTIL is rather constant with horizontally convergent flow, the TIL enhancement by vertical convergence in the tropics seems to come in hand with the aforementioned hydrostatic adjustment mechanism to deep convective outflow. We propose that vertical wind convergence near the tropopause is one mechanism enhancing the TIL at all latitudes, although caused by different processes: convection in the tropics and baroclinic waves in the extratropics.

Vertical wind convergence is related to anticyclones within baroclinic waves in the extratropics, but tropopause lifting (cooling) and the stratospheric residual circulation also enhance the TIL at the same time (Birner, 2010). In a similar way, we expect that the (100hPa) vertical wind convergence in the tropics is partly related to the equatorial wave spectrum, enhancing the tropical TIL along with other mechanisms (e.g. radiative forcing from water vapor or clouds). The equatorial wave modulation of the tropical TIL is studied in detail in section 4.

3.3 QBO influence

In Fig. 1 we showed that a secondary maximum of N^2 forms within the easterly wind regime of the QBO, just below the zero wind line of the descending westerly QBO phase, giving a double-TIL structure in the vertical N^2 profile in the lowermost stratosphere. This secondary N^2 maximum is responsible for the correlation of enhanced N^2 in the layer 1-3km above the tropopause with easterly winds (easterly QBO) found by Grise et al. (2010). However, no correlation was found in the layer 0-1km above TP (strictly where the TIL shall be), and no clear difference in TIL strength can be observed (Fig. 1) during the different phases of the QBO. We investigate this in more detail here, looking at the N^2_{max} values found right above the TP instead of averaging over a certain layer.

To define the QBO phase, we take the zonal wind regime in the lowermost stratosphere, nearest to the TIL: around 18-20km altitude, which can be observed in Fig. 1 (black and dashed contour lines). We take two seasons of the same QBO phase in each case from the period between 2007-2013. The easterly phase of the QBO is found in the summers of 2007 and 2012 and the following winters of 2007/08 and 2012/13; while the westerly phase of the QBO is found in winters of 2008/09 and 2010/11 and the following summers of 2009 and 2011.

Figure 4 shows the distribution of N^2_{max} for both winter (left, DJF) and summer (right, JJA). The black lines denote the average distribution over the 2007-2013 period, compared to easterly QBO phase (blue) and westerly QBO (red) as defined in the paragraph above. Winter has a higher mean N^2_{max} ($12.17\times10^{-4}s^{-2}$) than summer ($11.39\times10^{-4}s^{-2}$), in agreement with the results of Grise et al. (2010) and Figures 1 and 3. We find that, during the easterly phase of the QBO (blue lines), the N^2_{max} distributions slightly narrow and shift to lower values, giving lower seasonal means of $12.06\times10^{-4}s^{-2}$ in winter and $10.92\times10^{-4}s^{-2}$ in summer. During the westerly QBO phase (red lines), the opposite happens: the N^2_{max} distributions widen and shift to higher values compared to the average distribution, giving higher seasonal means of $12.74\times10^{-4}s^{-2}$ in winter and $11.49\times10^{-4}s^{-2}$ in summer.

In both winter and summer, the seasonal mean N^2_{max} in the westerly QBO phase is $\sim0.6\times10^{-4}s^{-2}$ higher than during the easterly QBO phase. This difference is highly significant: the standard deviation of the seasonal mean is of the order of $0.02\times10^{-4}s^{-2}$ (each distribution's sample size is $\sim$20000 profiles), and a t-test (two-tailed distributions with different sample sizes and variances) with these values gives us a t value of $\sim$20, which is well beyond the 99.9 percent confidence level (critical value $\sim$3.3).

In summary, from Fig. 4 we conclude that the tropical TIL is stronger during the westerly QBO phase in the lowermost stratosphere. This is not related to changes in the divergence distribution (given the relationship shown in Fig. 3), and is also anticorrelated with the strength of the secondary N^2 maximum found above the TIL region (Fig. 1).

The reason for this behavior of stronger TIL with westerly QBO is probably the modulation by Kelvin waves (the dipole of cooling near the tropopause and warming above), which have a higher activity in the lowermost stratosphere with westerly shear, and a slower vertical propagation (Randel and Wu, 2005) which translates into a longer residence time and longer modulation near the tropopause region to enhance the TIL. How equatorial waves modulate the vertical temperature and N^2 structure is explained below in section 4.

4 Modulation by Equatorial Waves

4.1 Effect on the zonal structure of tropopause height

This section describes how equatorial waves modulate the temperature and N^2 vertical structure in the tropics. As explained in section 2.4, the gridded temperature and N^2 fields are filtered independently with 12 different bandpass filters in the wavenumber-frequency domain. As in Wheeler and Kiladis (1999), no bandpass filters overlap in the wavenumber-frequency domain (see Table 1), and the 12 filters amount for Kelvin waves, equatorial Rossby waves, MJO, and the three modes *n* = (0,1,2) of westward-propagating (negative wavenumber s) Inertia-Gravity waves (WIG_n), the eastward-propagating ones (positive s, EIG_n), and the zonal wavenumber zero $_{s=0}IG_n$. For each wave type, a daily longitude-height section with its signature on temperature and N^2 is obtained.

Figure 5 shows examples of longitude-height snapshots with the N^2 anomalies (ΔN^2) of Kelvin (Fig. 5a), Rossby (Fig. 5b), EIG_n (Fig. 5c) and MJO band (Fig. 5d) at selected dates when the zonal structure of the tropopause (thick black line) is affected by the wave anomalies in an obvious way. In the case of EIG_n the three modes *n* = (0,1,2) are superimposed: the resulting field is EIG_n = EIG_0 + EIG_1 + EIG_2. Note that the filtered N^2 anomalies include a wide range of wavenumbers, 1-14 in the case of Kelvin waves for example (see Table 1), so the signatures of planetary waves 1 or 2 as well as transient shorter waves (higher wavenumbers) are represented together, giving a patchy appearance sometimes. Nevertheless, clear and coherent structures of the waves' N^2 signatures can be observed in Figure 5.

Temperature perturbations from Kelvin waves were observed to have their maximum near the tropopause in the study by Randel and Wu (2005). In Fig. 5 (with N^2), we see the same for all wave types: their maximum amplitude is generally found near and above the tropopause (black line). Also, zonal variations in tropopause height tend to be aligned with the wave's structure, with N^2 positive anomalies above the tropopause and negative anomalies below. This tropopause adjustment happens where the anomaly's amplitude is large, and is consistent with a dipole of tropopause cooling and warming aloft. This is clearly evident in Fig. 5a within 0-75°E and 100-180°E for Kelvin wave anomalies and in Fig. 5b within 0-125°W and ∼50°E for equatorial Rossby wave anomalies.

Although usually one wave type is dominant (therefore the choosing of separate dates in Fig. 5), different waves can influence the zonal structure of tropopause height at the same time: in Fig. 5 c and d (both of the same day, 2013-08-28), the MJO band creates a zonal variation of tropopause height within 50-125°E, while EIG_n wave anomalies do so within 50-150°W. We note that in most of the cases the strongest wave signatures, as well as zonal variations of the equatorial tropopause, are caused by transient waves with higher wavenumbers (as in every panel in Fig. 5) rather than planetary, quasi-stationary waves 1 or 2.

It is worth highlighting the structures that appear in the MJO band, with large amplitudes near the tropopause. Their eastward propagation, speed and longitudinal location match with the described patterns of deep convection associated to the MJO (Madden and Julian, 1994), but the horizontal and vertical scales are shorter. The N^2 anomalies from Fig. 5d are very similar to the composite temperature anomalies from the MJO band in the study by Kim and Son (2012), who found that MJO temperature anomalies near the tropopause have higher wavenumber due to their longer persistence compared to OLR anomalies.

When daily anomalies without running means are obtained as with our method, we see that the wave's anomalies shape the zonal structure of the tropopause, apart from the tropical tropopause layer (TTL) temperature and N^2 variability.

4.2 Average effect on the seasonal, zonal-mean profile

As explained in section 4.1, Figure 5 shows that the tropopause adjusts to the horizontal and vertical structure of the different wave types, with positive N^2 anomalies tending to be placed right above it. A tropopause-based mean of the wave's signature then should show an average enhancement of the TIL. The contribution of each equatorial wave type to the enhancement of the TIL is shown in Figure 6: for each wave type, a tropopause-based mean of the temperature and N^2 anomalies is done for all longitudes and winter days, achieving the average wave's effect on the seasonal, zonal-mean tropopause-based profile. EIG_n (green), WIG_n (orange) and ${}_{s=0}IG_n$ (grey) are the sum of all their modes *n* = (0,1,2).

In Fig. 6a, all waves produce an average maximum cold anomaly right at the lapse-rate TP and a warm anomaly around 1-2km above the tropopause. Our results are in agreement with the study by Grise and Thompson (2013) that showed a cooling effect near the climatological tropopause by equatorial planetary waves, and remind of the dipole with tropopause cooling and lower-stratospheric warming found by Kim and Son (2012) which they attributed to convectively coupled waves. In the study by Kim and Son (2012), Kelvin waves and the MJO were the dominant wave types in short-term TTL temperature variability. By deriving daily fields with no temporal smoothing (see section 2.4.1), we were able to ascertain the role of waves with higher frequencies and zonal wavenumbers than previous studies, pointing out new important features from Fig. 6a: 1) the cold anomaly is maximized and centered right at the thermal tropopause, 2) all equatorial wave types give a similar signature, whose magnitude is dependent on the amount of the wave's activity, and 3) the role of transient waves with higher zonal wavenumbers and frequencies is significant: WIG_n, EIG_n and Rossby waves have a bigger impact than the MJO.

The resulting N^2 signature (Fig. 6b) is a maximum N^2 enhancement right above the tropopause, and two regions of destabilization: below the tropopause and 2-3km above it. The overall effect is a TIL enhancement tightly close to the thermal tropopause. In Fig. 5 we showed obvious examples of tropopause adjustment to the wave structure with positive N^2 anomalies right above the tropopause. Given that the signature in the seasonal zonal-mean profile is considerable in Fig. 6, it can be concluded that the tropopause adjustment to the different waves (and the resulting dipole of colder tropopause / warm anomaly above in the tropopause-based zonal mean profile) occurs continuously, but not always so clearly as in Fig. 5. We stress that the signatures seen in Figures 5 and 6 were obtained by filtering the temperature and N^2 fields directly and independently, without any filtering in the vertical dimension.

Looking at the different wave types separately in Fig.6, the Kelvin wave (blue) has the strongest temperature signature (Fig. 6a), but owing to its longer vertical scale (see Fig. 5a) the temperature gradient that the Kelvin wave produces is closer to the rest of the waves', giving an average N^2 enhancement of 0.35×$10^{-4}s^{-2}$. The signatures of EIG_n (green), WIG_n (orange) and Rossby (red) waves give an average TIL enhancement of ∼0.25×$10^{-4}s^{-2}$ each, followed by the MJO band (purple, 0.1×$10^{-4}s^{-2}$). The ${}_{s=0}IG_n$ wave type (grey), although lacking zonal structures by definition and having little activity, still gives a minor TIL enhancement. The relative N^2 minima below the tropopause and above the TIL region in the seasonal zonal-mean profile (e.g. Grise et al. (2010)) can be attributed to the equatorial wave modulation as well.

The total effect of the equatorial waves on the equatorial zonal-mean seasonal temperature profile is a ∼1.1K colder tropopause and a ∼0.5K warm anomaly above, with a resulting TIL enhancement of ∼1.2×$10^{-4}s^{-2}$. Fig. 6 shows the mean wave effect during winter; the results are similar during summer (see Appendix B, figure B1) except for a slightly weaker effect of the MJO band, given its lower average activity in that season.

We acknowledge the possibility that the wave signals shown in Figs. 5 and 6 may not be 100% dynamical: a radiative component is included if clouds are present near the tropopause (radiative cooling at the cloud top that creates a temperature inversion). Part of the equatorial wave spectrum in the TTL is known to be coupled with convection, a small part of which reaches the tropopause (Wheeler and Kiladis, 1999; Fueglistaler et al., 2009), and the occurrence of cirrus clouds is also related to equatorial waves (Virts and Wallace, 2010). Case studies using GPS-RO data have investigated the temperature inversion generally found at cloud tops, for convective clouds (Biondi et al., 2012) and non-convective cirrus clouds (Taylor et al., 2011). The signal from any cloud coupled with an equatorial wave would be captured by its corresponding wavenumber-frequency domain filter, since the cloud signal would travel together with the wave in the same domain. Therefore a part of the mean wave signal shown in Fig. 6 could be due to the temperature inversion of (wave-coupled) cloud-tops near the tropopause, but quantifying this is beyond the scope of our study. Nevertheless, it is logical to assume that the radiative part associated to the equatorial wave signal shall be small, since near-tropopause height cloud tops are not frequent, equatorial waves are not radiatively driven and their propagation is explained by dry dynamics.

Also note that in the case where the equatorial waves (Figs. 5 and 6) are coupled to convection, the tropopause cooling by the hydrostatic adjustment mechanism (Holloway and Neelin, 2007) is captured by the filters as well, and a much refined methodology would be needed to separate the contribution of equatorial waves and convection alone.

Our results from this section (Figs. 5 and 6) agree with earlier studies that derived equatorial wave anomalies from GPS-RO data (the Kelvin and MJO signatures and their amplification near the tropopause (Randel and Wu, 2005; Kim and Son, 2012)). Also, Fig. 6 confirms the effect of equatorial waves on the mean temperature profile (colder tropopause and warm anomalies above forming a dipole (Kim and Son, 2012; Grise and Thompson, 2013)) and their crucial role in enhancing the TIL in the tropics (Grise et al., 2010). The novelty in our study resides in that we include small-scale, higher-frequency waves (e.g. Inertia-Gravity waves); and that we are able to quantify the effect of each equatorial wave type separately by tropopause-based averaging of the filtered wave anomalies.

Our results from this section should not be viewed as a mere quantification of the waves themselves or an artifact of the tropopause-coordinate. Although transient and instantaneous, there are motions associated to the wave signals that locally lift/cool/modulate the tropopause, and also warm the air aloft. Another characteristic of the waves is that they amplify next to and above the tropopause (Fig. 5), and also increase their vertical tilt (Fig. 5a, visible for Kelvin waves), which increases the wave signal in the TIL region, and also increases the area of positive N^2 anomaly above the tropopause. This is a response of the wave to the elevated N^2 values in the lowermost stratosphere, in agreement with linear theory, which in turn enhances the TIL further, working as a positive feedback. Although our results point in this direction, more research needs to be carried out to consider such a feedback as a robust feature of the global tropopause region.

4.3 TIL without equatorial wave signals

Figure 7 shows the daily evolution of the equatorial zonal-mean, tropopause-based N^2 profile (Fig. 7a), and the resulting N^2 profile when the equatorial wave signals are subtracted (Fig. 7b). The display is very similar to that of Fig. 1, but in order to allow the subtraction of the equatorial wave signal, for Fig. 7 we use the gridded dataset obtained in section 2.4, from COSMIC profiles only (2007-2013) and 10°S-10°N without any temporal smoothing of N^2.

A clear difference in the TIL region can be observed in Fig. 7b: without the equatorial wave signal, the TIL in the first kilometer above the tropopause is much weakened, from N^2 values of 7-9$\times 10^{-4} s^{-2}$ right above the tropopause (orange-red colors in Fig. 7a) to values of 6-7$\times 10^{-4} s^{-2}$ (yellow-orange colors in Fig. 7b) and even less sometimes. In Fig. 7b, the stronger TIL with N^2 values above $7\times 10^{-4} s^{-2}$ (red) is very sparse in time and restricted to wintertime. The differences between Fig. 7a and Fig. 7b agree well with the magnitude of mean TIL enhancement calculated in section 4.2 (Fig. 6).

However, in Fig. 7b the deeper N^2 structures between the tropopause and ∼20km altitude remain intact, as well as the secondary N^2 maximum below the descending westerly QBO phase: they are basically the same as in Fig. 7a and therefore not directly modulated by equatorial waves.

What other mechanisms could enhance the TIL in the tropics? Deep convection that is not coupled with any equatorial wave can also lead to tropopause cooling (by hydrostatic adjustment) and TIL enhancement, as discussed in section 3.2 (Holloway and Neelin, 2007; Paulik and Birner, 2012). Given that deep convection near the equator is more frequent in winter, this would explain the occurrence of stronger TIL in Fig. 7b within this season. Radiative cooling from non-convective cloud tops near the tropopause (e.g. Taylor et al. (2011)), or from strong humidity gradients across the tropopause, can also enhance the gradients that lead to TIL enhancement.

Also note that the wave signals in Fig. 5, their average signature in Fig. 6, and the subtracted signals in Fig. 7b, all come from the instantaneous filtered anomalies: once the wave has left the tropopause region, or dissipated, our filters do not capture any signal that could modulate the TIL. The wave-mean flow interaction is not visible with our method, since its more persistent temperature and N^2 effect would not travel in the wavenumber-frequency domain any more.

The secondary N^2 maximum below the descending westerly QBO phase can be related to the temperature anomaly associated to the wind shear of the QBO (Baldwin et al., 2001), which affects the background N^2 structure throughout the stratosphere. It can be seen in Figs. 1 and 7 that during the easterly phase of the QBO, N^2 between 20-30km altitude is generally higher than within westerlies. It is also possible that the N^2 maximum right below the zero wind line of the descending westerly QBO could be forced by a temperature anomaly from the dissipation of Kelvin waves, which propagate vertically with easterlies until they reach westerly shear. In this case, it would be an indirect effect of Kelvin waves: once they dissipate there is no signal to be captured by our filter. Quantifying this effect (for both the secondary N^2 maximum and the TIL, as in the previous paragraph) is beyond the scope of our study.

5 Discussion: Applicability of the Wave Modulation in the Extratropics

As Fig. 6 showed, all equatorial wave types have the same effect on the temperature and N^2 seasonal zonal-mean vertical profiles, only varying in magnitude. Since all wave types have the same signature, one could expect a similar picture coming from the extratropical wave spectrum. Taking the extratropical baroclinic Rossby wave as an example: the embedded cyclones-anticyclones with lower-higher tropopause would be an example of tropopause adjustment to the anomalies associated with the wave, as in Fig. 5. Given that the zonal variability of TP_z at mid-latitudes is much larger than within the tropics (3km against 0.8km, see Appendix A) and that temperature gradients next to the jet stream are also of much higher magnitude, it is probable that the extratropical Rossby wave's N^2 signature on the mid-latitude zonal mean profile is even stronger than the signal observed from Kelvin waves in Fig. 6, which dominates in the tropics. Inertia-gravity waves are also widely present in the extratropics. Depending on the amplitude they reach next to the extratropical tropopause, this wave type shall also contribute to enhance the TIL, which is predicted by the modelling experiment by Kunkel et al. (2014).

The wavenumber-frequency domain filtering method used with the dispersion curves of extratropical wave modes would be suited to quantify the modulation of each wave mode on the extratropical TIL, in the same way our study has done with equatorial waves. Also, similarly to section 4.3 and Fig. 7, it could be possible to show how much of the TIL in the extratropics is due to processes other than the instantaneous modulation by extratropical waves (i.e. radiative forcing or residual circulation). Preliminary results show that the method used in this paper is indeed applicable in the extratropics as well, and a new paper about this is in preparation.

6 Concluding Remarks

Our study explores the horizontal and vertical variability of the tropical TIL, the effect of the QBO, the role of near-tropopause horizontal wind divergence and the role of equatorial waves in enhancing the tropical TIL. Overall it gives an in-depth observational description of the TIL properties in the tropics and the mechanisms that lead to its enhancement in a region where research has focused very little so far.

Our results agree with the seasonality and location of the tropical TIL described by Grise et al. (2010), with stronger TIL centered at the equator and peaking during NH winter. We describe a new feature: a secondary N^2 maximum that forms above the TIL region within the easterly wind regime of the QBO, below the zero wind line of the descending westerly QBO (Fig. 1). This secondary maximum leads to a double-TIL-like structure in the stability profile, and explains the correlation of enhanced N^2 in the 1-3km layer above the tropopause with easterly QBO found by Grise et al. (2010). The behavior of the secondary N^2 maximum is anticorrelated with the TIL strength (strictly the N^2_{max} found less than 1km above the tropopause): the TIL is stronger during the westerly phase of the QBO in the lowermost stratosphere (Fig. 4).

The zonal structure of the tropical TIL shows a stronger (weaker) TIL with near-tropopause divergent (convergent) flow (Fig. 2). This sTIL-divergence relationship (Fig. 3) is analogous to that of TIL strength with relative vorticity found in the extratropics (Randel et al., 2007; Randel and Wu, 2010; Pilch Kedzierski et al., 2015), and we suggest that vertical wind convergence is a TIL enhancing mechanism that the tropics (divergent flow) and extratropics (anticyclones) have in common.

We also quantified the signature of the different equatorial waves on the seasonal zonal-mean temperature and N^2 profile (Fig. 6). All wave types have, on average, maximum cold anomalies at the thermal tropopause and warm anomalies above, enhancing the TIL strength very close to the tropopause. The way this modulation is done is by tropopause adjustment to the vertical structure of the wave's associated anomalies when these have high amplitudes (Fig. 5). While agreeing with earlier studies that used GPS-RO to investigate equatorial waves (Randel and Wu, 2005; Kim and Son, 2012), our results show the importance of small-scale, high-frequency waves due to our method with minimized temporal smoothing, which enables us to quantify and compare the role of each different equatorial wave type for the first time. Inertia-gravity and Rossby waves play a very significant role, with a bigger signature than the MJO, and Kelvin waves dominate the net tropopause cooling and warming above in the tropopause-based profile, with the resulting TIL enhancement (Fig. 6).

Without the equatorial wave signal, the TIL is much weakened (Fig. 7) but part of it remains, and we point to non-wave-coupled deep convection (tropopause cooling by hydrostatic adjustment, (Holloway and Neelin, 2007; Paulik and Birner, 2012)) and radiative effects from clouds or humidity gradients as other possible mechanisms that could enhance the tropical TIL.

We suggest that this wave modulation will also be present in the extratropics with baroclinic Rossby and inertia-gravity waves as main contributors, which will be the subject of a follow-on study.

Appendix A: Divergence vs Tropopause Height

Figure A1 shows divergence versus tropopause height (TP_z) diagrams, as in Fig. 3 with TIL strength (section 3.2). There is no clear link between a higher tropopause and a stronger TIL. In summer (Fig. A1 a), the relation of higher TP_z with divergent flow is very small: the difference between convergent-divergent flow is only of 0.8km, while the difference in cyclones-anticyclones in the extratropics is over 3km (Randel and Wu, 2010). In winter (Fig. A1 b) this relation is non-existent: the tropical TP_z is around 17km at all divergence-convergence values.

Appendix B: Equatorial Wave Modulation in Summer

Figure B1 is the summer counterpart of Fig. 6 from section 4. The average effect of each wave in summer (Fig. B1) is very similar to the one from winter (Fig. 6), except for a smaller MJO signature.

Appendix C: Caveat on the Filtering of Periods of 1-2 Days from a Daily Dataset

As shown in Table 1, the modes *n* = 2 of all inertia-gravity wave types (EIG_n, WIG_n and $_{s=0}IG_n$) are defined for periods between 1-2 days. With a dataset of daily temporal resolution, filtering with such periods has to be taken with lots of caution for two reasons:

1) Oscillations with periods below 2 times the temporal resolution of the dataset (below 2 days in this case) are underestimated (best case scenario), or not resolved at all by the dataset. Nevertheless we applied these filters, should any part of the wave signal be discernible.

2) Once filtered, the resulting wave anomalies are subject to include spurious signals because of spectral ringing. It is very important to know how much of the wave signature in Figure 6 comes from this artifact, since all modes $n = (0,1,2)$ are summed-up there.

We computed the mean signature of modes $n = (0,1,2)$ separately, and found that all of the signal in Fig. 6 comes from modes $n = 0$ and 1. This means that the filters of inertia-gravity waves with periods between 1-2 days do not capture any signal at all (artificial or not), and therefore make no contribution to our results. The equatorial wave signature in Fig. 6 (and Fig. B1) comes entirely from oscillations that are resolved by our gridded daily dataset obtained from COSMIC GPS-RO profiles.

Waves with periods below 2 days could modulate the tropical tropopause region and the TIL, though: only the current amount of GPS-RO profiles is not enough to resolve this. It shall be possible to do so once COSMIC-2 profiles (a much increased amount compared to current data) are available.

Acknowledgements. This study was completed within the Helmholtz-University Young Investigators Group NATHAN project, funded by the Helmholtz Association through the president's Initiative and Networking Fund and the GEOMAR Helmholtz-Centre for Ocean Research in Kiel. We thank the ECMWF data server for the freely available ERA-Interim data; and UCAR for the COSMIC, CHAMP and GRACE satellite missions' temperature profiles. Comments by Joowan Kim and two anonymous reviewers are highly appreciated and clearly helped to improve the manuscript significantly. The assistance accessing different datasets and discussions with Sandro Lubis, Wuke Wang and Sebastian Wahl are also appreciated.

References

Anthes, R. A., Bernhardt, P. A., Chen, Y., Cucurull, L., Dymond, K. F., Ector, D., Healy, S. B., Ho, S.-P., Hunt, D. C., Kuo, Y.-H., Liu, H., Manning, K., McCormick, C., Meehan, T. K., Randel, W. J., Rocken, C., Schreiner, W. S., Sokolovskiy, S. V., Syndergaard, S., Thompson, D. C., Trenberth, K. E., Wee, T.-K., Yen, N. L., and Zeng, Z.: The COSMIC/FORMOSAT-3 Mission: Early Results, Bulletin of the American Meteorological Society, 89, 313, doi:10.1175/BAMS-89-3-313, 2008.

Baldwin, M. P., Gray, L. J., Dunkerton, T. J., Hamilton, K., Haynes, P. H., Randel, W. J., Holton, J. R., Alexander, M. J., Hirota, I., Horinouchi, T., Jones, D. B. A., Kinnersley, J. S., Marquardt, C., Sato, K., and Takahashi, M.: The quasi-biennial oscillation, Reviews of Geophysics, 39, 179–229, doi:10.1029/1999RG000073, 2001.

Bell, S. W. and Geller, M. A.: Tropopause inversion layer: Seasonal and latitudinal variations and representation in standard radiosonde data and global models, Journal of Geophysical Research (Atmospheres), 113, D05109, doi:10.1029/2007JD009022, 2008.

Beyerle, G., Schmidt, T., Michalak, G., Heise, S., Wickert, J., and Reigber, C.: GPS radio occultation with GRACE: Atmospheric profiling utilizing the zero difference technique, Geophysical Research Letters, 32, L13806, doi:10.1029/2005GL023109, 2005.

Biondi, R., Randel, W. J., Ho, S.-P., Neubert, T., and Syndergaard, S.: Thermal structure of intense convective clouds derived from GPS radio occultations, Atmospheric Chemistry & Physics, 12, 5309–5318, doi:10.5194/acp-12-5309-2012, 2012.

Birner, T.: Fine-scale structure of the extratropical tropopause region, Journal of Geophysical Research (Atmospheres), 111, D04104, doi:10.1029/2005JD006301, 2006.

Birner, T.: Residual Circulation and Tropopause Structure, Journal of Atmospheric Sciences, 67, 2582–2600, doi:10.1175/2010JAS3287.1, 2010.

Birner, T., Dörnbrack, A., and Schumann, U.: How sharp is the tropopause at midlatitudes?, Geophysical Research Letters, 29, 1700, doi:10.1029/2002GL015142, 2002.

Birner, T., Sankey, D., and Shepherd, T. G.: The tropopause inversion layer in models and analyses, Geophysical Research Letters, 33, L14804, doi:10.1029/2006GL026549, 2006.

Dee, D. P., Uppala, S. M., Simmons, A. J., Berrisford, P., Poli, P., Kobayashi, S., Andrae, U., Balmaseda, M. A., Balsamo, G., Bauer, P., Bechtold, P., Beljaars, A. C. M., van de Berg, L., Bidlot, J., Bormann, N., Delsol, C., Dragani, R., Fuentes, M., Geer, A. J., Haimberger, L., Healy, S. B., Hersbach, H., Hólm, E. V., Isaksen, L., Kållberg, P., Köhler, M., Matricardi, M., McNally, A. P., Monge-Sanz, B. M., Morcrette, J.-J., Park, B.-K., Peubey, C., de Rosnay, P., Tavolato, C., Thépaut, J.-N., and Vitart, F.: The ERA-Interim reanalysis: configuration and performance of the data assimilation system, Quarterly Journal of the Royal Meteorological Society, 137, 553–597, doi:10.1002/qj.828, 2011.

Erler, A. R. and Wirth, V.: The Static Stability of the Tropopause Region in Adiabatic Baroclinic Life Cycle Experiments, Journal of Atmospheric Sciences, 68, 1178–1193, doi:10.1175/2010JAS3694.1, 2011.

Fueglistaler, S., Dessler, A. E., Dunkerton, T. J., Folkins, I., Fu, Q., and Mote, P. W.: Tropical tropopause layer, Reviews of Geophysics, 47, RG1004, doi:10.1029/2008RG000267, 2009.

Gettelman, A. and Birner, T.: Insights into Tropical Tropopause Layer processes using global models, Journal of Geophysical Research (Atmospheres), 112, D23104, doi:10.1029/2007JD008945, 2007.

Gettelman, A., Hoor, P., Pan, L. L., Randel, W. J., Hegglin, M. I., and Birner, T.: The Extratropical Upper Troposphere and Lower Stratosphere, Reviews of Geophysics, 49, RG3003, doi:10.1029/2011RG000355, 2011.

Grise, K. M. and Thompson, D. W. J.: On the Signatures of Equatorial and Extratropical Wave Forcing in Tropical Tropopause Layer Temperatures, Journal of Atmospheric Sciences, 70, 1084–1102, doi:10.1175/JAS-D-12-0163.1, 2013.

Grise, K. M., Thompson, D. W. J., and Birner, T.: A Global Survey of Static Stability in the Stratosphere and Upper Troposphere, Journal of Climate, 23, 2275–2292, doi:10.1175/2009JCLI3369.1, 2010.

Hegglin, M. I., Boone, C. D., Manney, G. L., and Walker, K. A.: A global view of the extratropical tropopause transition layer from Atmospheric Chemistry Experiment Fourier Transform Spectrometer O_3, H_2O, and CO, Journal of Geophysical Research (Atmospheres), 114, D00B11, doi:10.1029/2008JD009984, 2009.

Holloway, C. E. and Neelin, J. D.: The Convective Cold Top and Quasi Equilibrium*, Journal of Atmospheric Sciences, 64, 1467, doi:10.1175/JAS3907.1, 2007.

Kim, J. and Son, S.-W.: Tropical Cold-Point Tropopause: Climatology, Seasonal Cycle, and Intraseasonal Variability Derived from COSMIC GPS Radio Occultation Measurements, Journal of Climate, 25, 5343–5360, doi:10.1175/JCLI-D-11-00554.1, 2012.

Kunkel, D., Hoor, P., and Wirth, V.: Can inertia-gravity waves persistently alter the tropopause inversion layer?, Geophysical Research Letters, 41, 7822–7829, doi:10.1002/2014GL061970, 2014.

Kunz, A., Konopka, P., Müller, R., Pan, L. L., Schiller, C., and Rohrer, F.: High static stability in the mixing layer above the extratropical tropopause, Journal of Geophysical Research (Atmospheres), 114, D16305, doi:10.1029/2009JD011840, 2009.

Kursinski, E. R., Hajj, G. A., Schofield, J. T., Linfield, R. P., and Hardy, K. R.: Observing Earth's atmosphere with radio occultation measurements using the Global Positioning System, Journal of Geophysical Research: Atmospheres, 102, 23 429–23 465, doi:10.1029/97JD01569, 1997.

Lindzen, R. D.: Planetary Waves on Beta-Planes, Monthly Weather Review, pp. 441–451, 1967.

Madden, R. A. and Julian, P. R.: Observations of the 40 50-Day Tropical Oscillation - A Review, Monthly Weather Review, 122, 814, doi:10.1175/1520-0493(1994)122<0814:OOTDTO>2.0.CO;2, 1994.

Matsuno, T.: Quasi-Geostrophic Motions in the Equatorial Area, Journal of the Meteorological Society of Japan. Ser. II, 44, 25–43, 1966.

Miyazaki, K., Watanabe, S., Kawatani, Y., Sato, K., Tomikawa, Y., and Takahashi, M.: Transport and Mixing in the Extratropical Tropopause Region in a High-Vertical-Resolution GCM. Part II: Relative Importance of Large-Scale and Small-Scale Dynamics, Journal of Atmospheric Sciences, 67, 1315–1336, doi:10.1175/2009JAS3334.1, 2010a.

Miyazaki, K., Watanabe, S., Kawatani, Y., Tomikawa, Y., Takahashi, M., and Sato, K.: Transport and Mixing in the Extratropical Tropopause Region in a High-Vertical-Resolution GCM. Part I: Potential Vorticity and Heat Budget Analysis, Journal of Atmospheric Sciences, 67, 1293–1314, doi:10.1175/2009JAS3221.1, 2010b.

Paulik, L. C. and Birner, T.: Quantifying the deep convective temperature signal within the tropical tropopause layer (TTL), Atmospheric Chemistry & Physics, 12, 12 183–12 195, doi:10.5194/acp-12-12183-2012, 2012.

Pilch Kedzierski, R., Matthes, K., and Bumke, K.: Synoptic-scale behavior of the extratropical tropopause inversion layer, Geophysical Research Letters, 42, 10,018–10,026, doi:10.1002/2015GL066409, 2015GL066409, 2015.

Poli, P., Healy, S. B., and Dee, D. P.: Assimilation of Global Positioning System radio occultation data in the ECMWF ERA-Interim reanalysis, Quarterly Journal of the Royal Meteorological Society, 136, 1972–1990, doi:10.1002/qj.722, 2010.

Randel, W. J. and Wu, F.: Kelvin wave variability near the equatorial tropopause observed in GPS radio occultation measurements, Journal of Geophysical Research (Atmospheres), 110, D03102, doi:10.1029/2004JD005006, 2005.

Randel, W. J. and Wu, F.: The Polar Summer Tropopause Inversion Layer, Journal of Atmospheric Sciences, 67, 2572–2581, doi:10.1175/2010JAS3430.1, 2010.

Randel, W. J., Wu, F., and Forster, P.: The Extratropical Tropopause Inversion Layer: Global Observations with GPS Data, and a Radiative Forcing Mechanism, Journal of Atmospheric Sciences, 64, 4489, doi:10.1175/2007JAS2412.1, 2007.

Schmidt, T., Cammas, J.-P., Smit, H. G. J., Heise, S., Wickert, J., and Haser, A.: Observational characteristics of the tropopause inversion layer derived from CHAMP/GRACE radio occultations and MOZAIC aircraft data, Journal of Geophysical Research (Atmospheres), 115, D24304, doi:10.1029/2010JD014284, 2010.

Schreck, C.: Extract equatorial waves by filtering in the Wheeler-Kiladis wavenumber-frequency domain., https://www.ncl.ucar.edu/Document/Functions/User_contributed/kf_filter.shtml, 2009.

Son, S.-W. and Polvani, L. M.: Dynamical formation of an extra-tropical tropopause inversion layer in a relatively simple general circulation model, Geophysical Research Letters, 34, L17806, doi:10.1029/2007GL030564, 2007.

Son, S.-W., Tandon, N. F., and Polvani, L. M.: The fine-scale structure of the global tropopause derived from COSMIC GPS radio occultation measurements, Journal of Geophysical Research (Atmospheres), 116, D20113, doi:10.1029/2011JD016030, 2011.

Taylor, J. R., Randel, W. J., and Jensen, E. J.: Cirrus cloud-temperature interactions in the tropical tropopause layer: a case study, Atmospheric Chemistry & Physics, 11, 10 085–10 095, doi:10.5194/acp-11-10085-2011, 2011.

Virts, K. S. and Wallace, J. M.: Annual, Interannual, and Intraseasonal Variability of Tropical Tropopause Transition Layer Cirrus, Journal of Atmospheric Sciences, 67, 3097–3112, doi:10.1175/2010JAS3413.1, 2010.

Wang, W., Matthes, K., Schmidt, T., and Neef, L.: Recent variability of the tropical tropopause inversion layer, Geophysical Research Letters, 40, 6308–6313, doi:10.1002/2013GL058350, 2013.

Wheeler, M. and Kiladis, G. N.: Convectively Coupled Equatorial Waves: Analysis of Clouds and Temperature in the Wavenumber-Frequency Domain., Journal of Atmospheric Sciences, 56, 374–399, doi:10.1175/1520-0469(1999)056<0374:CCEWAO>2.0.CO;2, 1999.

Wickert, J., Reigber, C., Beyerle, G., König, R., Marquardt, C., Schmidt, T., Grunwaldt, L., Galas, R., Meehan, T. K., Melbourne, W. G., and Hocke, K.: Atmosphere sounding by GPS radio occultation: First results from CHAMP, Geophysical Research Letters, 28, 3263–3266, doi:10.1029/2001GL013117, 2001.

Wirth, V.: Static Stability in the Extratropical Tropopause Region., Journal of Atmospheric Sciences, 60, 1395–1409, doi:10.1175/1520-0469(2003)060<1395:SSITET>2.0.CO;2, 2003.

Wirth, V.: A dynamical mechanism for tropopause sharpening, Meteorologische Zeitschrift, 13, 477–484, doi:10.1127/0941-2948/2004/0013-0477, 2004.

Wirth, V. and Szabo, T.: Sharpness of the extratropical tropopause in baroclinic life cycle experiments, Geophysical Research Letters, 34, 2809, doi:10.1029/2006GL028369, 2007.

WMO: Meteorology-A three-dimensional science, WMO Bull., 6, 134–138, 1957.

Yulaeva, E., Holton, J. R., and Wallace, J. M.: On the Cause of the Annual Cycle in Tropical Lower-Stratospheric Temperatures., Journal of Atmospheric Sciences, 51, 169–174, doi:10.1175/1520-0469(1994)051<0169:OTCOTA>2.0.CO;2, 1994.

Table 1. Parameters used to bound the filter of the different equatorial wave types, with the meridional mode *n* as subscript: *t* (period, in days), *s* (zonal planetary wavenumber) and *h* (equivalent depth, in m)

Wave type	t_{min}	t_{max}	s_{min}	s_{max}	h_{min}	h_{max}
Eq. Rossby	6	70	-14	-1	6	600
Kelvin	4	30	1	14	6	600
MJO	30	96	2	5	8	90
WIG_0	2.5	6	-10	-1	6	360
WIG_1	2	2.5	-15	-1	8	90
WIG_2	1	2	-15	-1	8	90
EIG_0	2.5	4	1	15	8	90
EIG_1	2	2.5	1	15	8	90
EIG_2	1	2	1	15	8	90
$_{s=0}IG_0$	3	6	-0.1	0.1	8	90
$_{s=0}IG_1$	2	3	-0.1	0.1	8	90
$_{s=0}IG_2$	1	2	-0.1	0.1	8	90

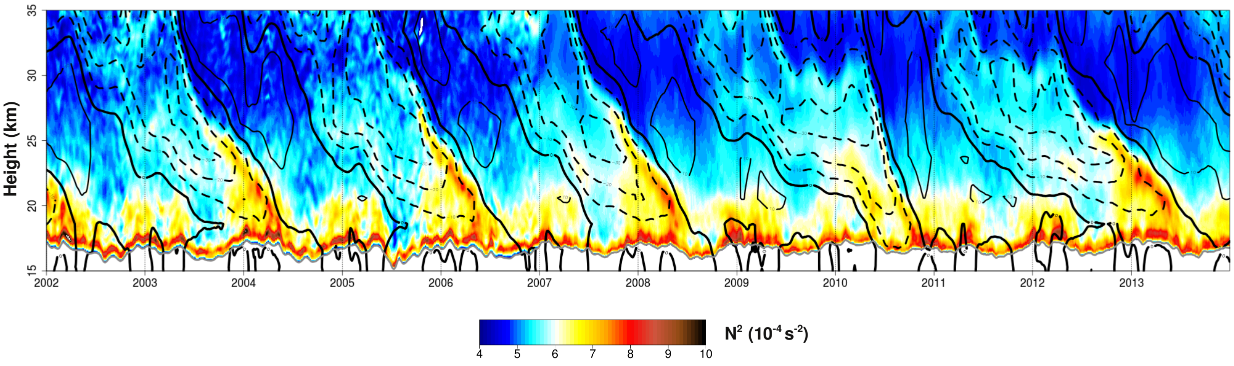

Figure 1. Daily evolution of the tropopause-based, equatorial (5°S-5°N) zonal mean N^2 vertical profile between 2002-2013 (colors). 2002-2006 from CHAMP+GRACE GPS-RO profiles, 2007-2013 from COSMIC. The grey line denotes the tropopause height (TP_z). Thin black contours denote positive (westerly) mean zonal wind, with a thicker contour for the zero line, dashed contours for negative (easterly) winds, and a 10m/s separation. To improve visibility, each day shows the running mean N^2 profile and TP_z of +-7 days. In the case of the winds, the running mean is made for +-15 days.

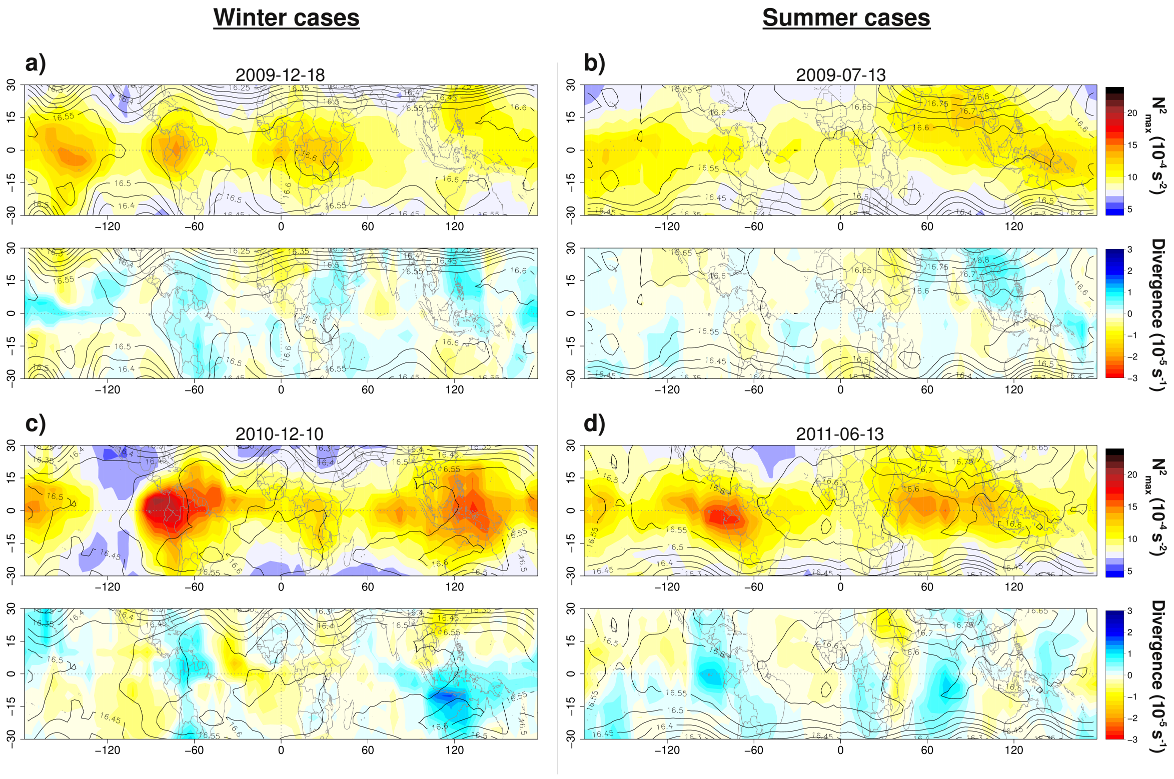

Figure 2. Maps of daily TIL strength (N^2_{max}, first and third rows) and 100hPa horizontal wind divergence (second and fourth rows). Winter cases are on the left side, and summer cases are on the right side. Corresponding color scales are on the right end. Contour lines show the 100hPa geopotential height (in km' with 50m' interval).

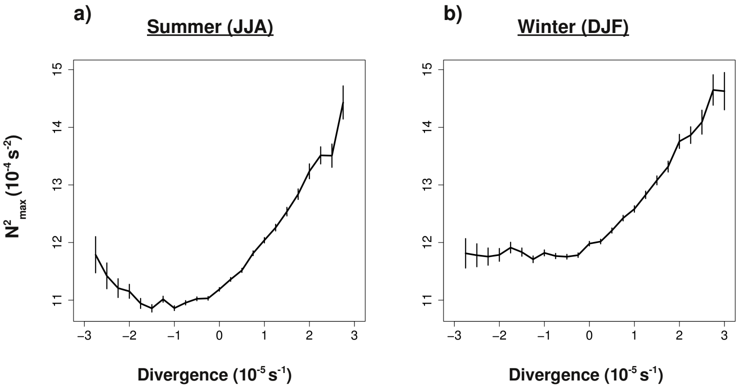

Figure 3. Diagrams of horizontal wind divergence versus TIL strength (N^2_{max}) for the latitude band 10°S-10°N. a) belongs to the summer season (JJA), and b) to the winter season (DJF). Vertical bars denote one standard deviation of the mean value.

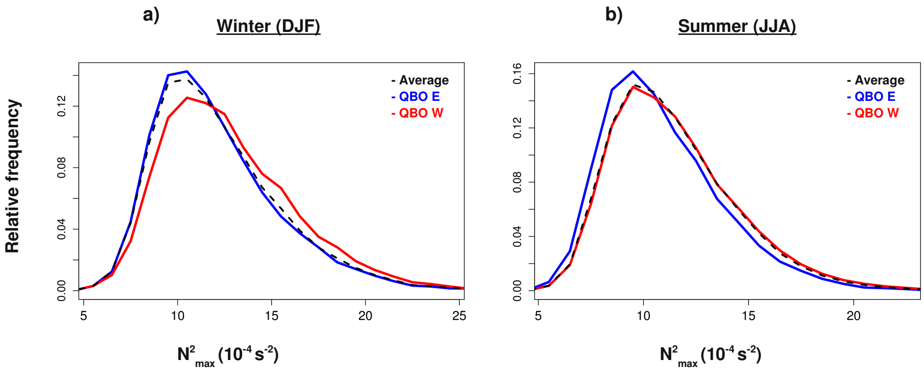

Figure 4. Histograms with relative frequency of TIL strength (N^2_{max}), for winter (a, DJF) and summer (b, JJA). The black dashed line denotes the average seasonal distribution. The blue line shows distributions during the easterly phase of the QBO in the lowermost stratosphere, and the red line shows the distributions during the westerly QBO phase.

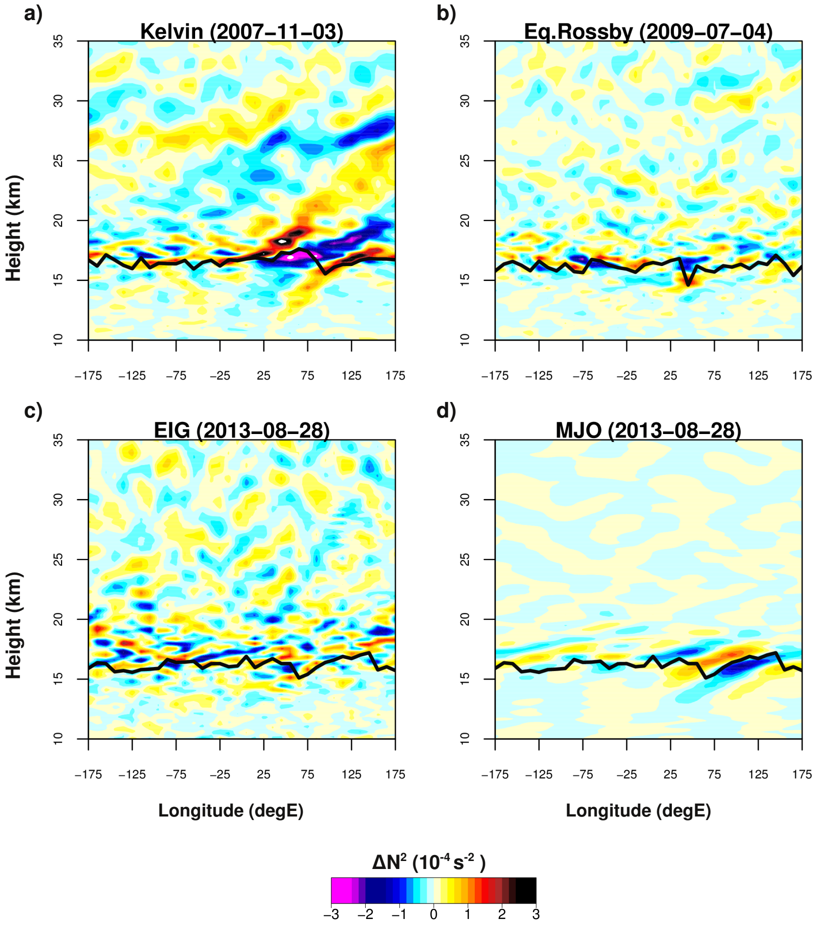

Figure 5. Longitude-height snapshots of static stability anomalies (ΔN^2) of different wave types at certain dates: a) Kelvin wave, b) Rossby wave, c) Eastward IGW (EIG_n), d) MJO band. The black line denotes the thermal tropopause.

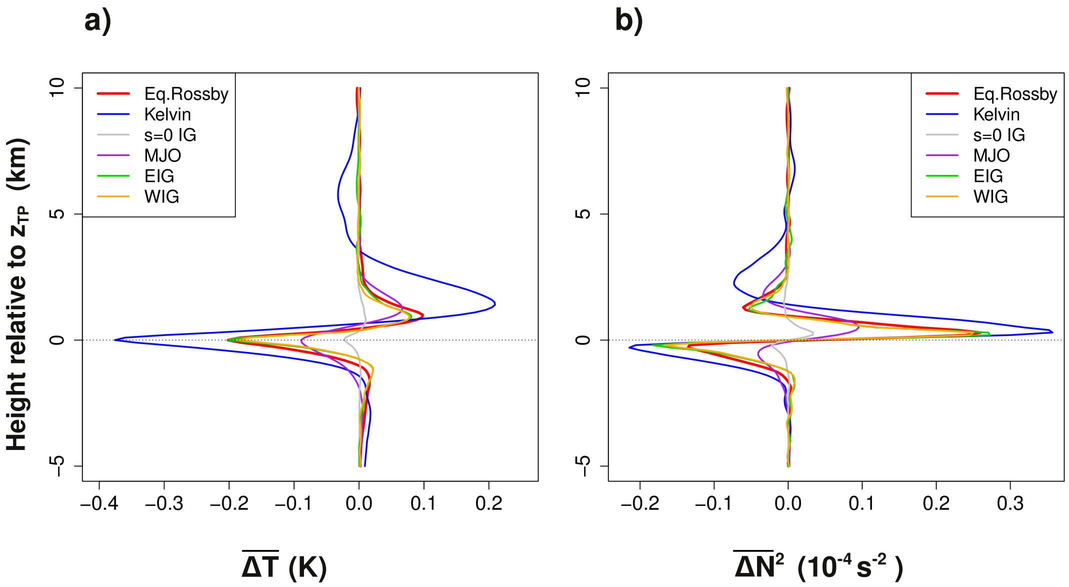

Figure 6. Winter (DJF) average signature of the different wave types, as the mean anomalies of (a) temperature $\overline{\Delta T}$ and (b) static stability $\overline{\Delta N^2}$ in the equatorial zonal-mean vertical profiles (10°S-10°N).

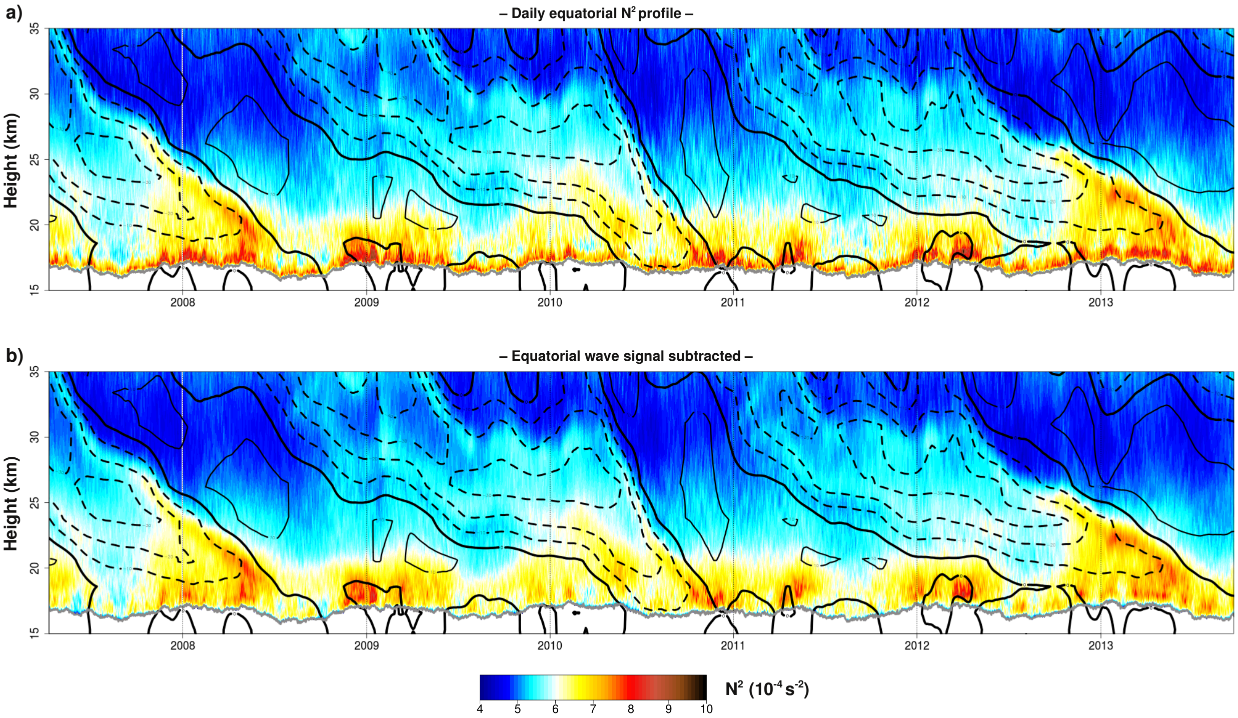

Figure 7. a) Daily evolution of the tropopause-based, equatorial (10°S-10°N) zonal mean N^2 vertical profile between 2007-2013 (colors) from COSMIC GPS-RO profiles. The grey line denotes the tropopause height (TP_z). Thin black contours denote positive (westerly) mean zonal wind, with a thicker contour for the zero line, dashed contours for negative (easterly) winds, and a 10m/s separation. To improve visibility, the winds are displayed with a running mean of +-15 days. No running mean is applied to the N^2 vertical profile or TP_z in order to allow the subtraction of the equatorial wave signal. b) Equatorial wave signal subtracted from the N^2 vertical profile.

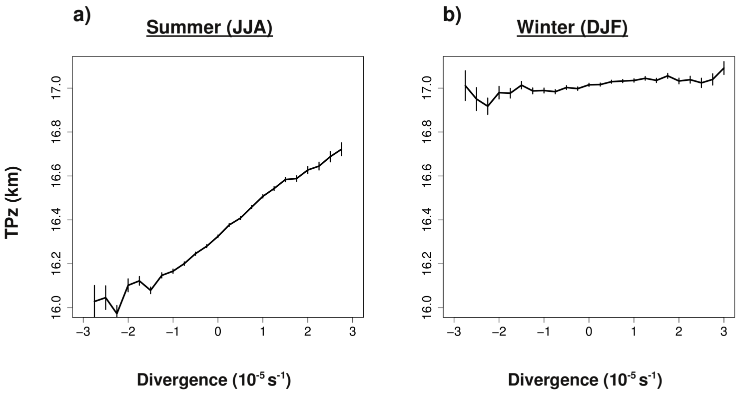

Figure A1. Diagrams of divergence versus tropopause height (TP_z, km) for the latitude band 10°S-10°N. a) belongs to the summer season (JJA), and b) to the winter season (DJF). Vertical bars denote one standard deviation of the mean value.

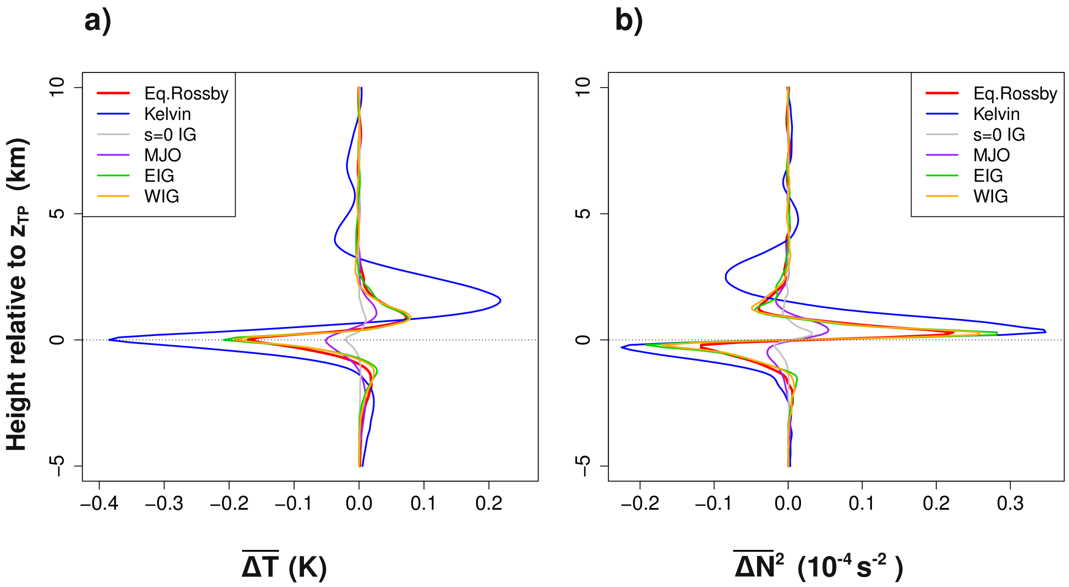

Figure B1. Summer (JJA) average signature of the different wave types, as the mean anomalies of (a) temperature $\overline{\Delta T}$ and (b) static stability $\overline{\Delta N^2}$ in the equatorial zonal-mean vertical profiles (10°S-10°N).

4 The Extratropical Tropopause Inversion Layer

This chapter is the equivalent to chapter 3 (which was for the tropics), but in this case the extratropical TIL is discussed under two aspects separately, consisting of two publications: one about synoptic-scale variability of the TIL, and the other about its wave modulation which is why this chapter is subdivided into two sections:

Section 4.1 will present daily snapshots of the horizontal structures of TIL strength in the extratropics, showing its synoptic-scale behavior collocated with troughs and ridges embedded within baroclinic waves near the tropopause. Also, relative vorticity is split into shear and curl terms: shear is horizontal wind gradient as from balanced adiabatic dynamics, while curl is an air parcel's spin and indicates flow imbalance; and the two terms contribute differently to TIL strength.

Section 4.2 will quantify the TIL modulation and enhancement by transient extratropical waves, with a simplified version of the method used to filter equatorial waves in section 3. In this case, the total TIL enhancement by planetary and synoptic-scale extratropical waves is obtained, for mid-latitudes and polar latitudes in both Hemispheres. Once the total wave signal is subtracted from the daily N^2 profiles, other TIL enhancing processes become clear.

Both sections consist of reprints of articles with the same title that have been published or submitted to scientific journals.

4.1 Synoptic-Scale Behavior of the Extratropical Tropopause Inversion Layer

Citation:

Pilch Kedzierski, R., K. Matthes, and K. Bumke (2015), Synoptic-scale behavior of the extratropical tropopause inversion layer, *Geophysical Research Letters*, *42*(22), 10,018–10,026, doi:10.1002/2015GL066409.

Author contributions to this publication:

- R. Pilch Kedzierski designed the method, did the analysis, produced all the figures and wrote the manuscript.
- K. Matthes initiated the study, contributed with ideas and discussions on the analysis, and commented the manuscript.
- K. Bumke suggested the relative vorticity split into curl and shear terms, and discussed and commented the manuscript.

AGU PUBLICATIONS

Geophysical Research Letters

RESEARCH LETTER

10.1002/2015GL066409

Synoptic-scale behavior of the extratropical tropopause inversion layer

Robin Pilch Kedzierski[1], **Katja Matthes**[1,2], **and Karl Bumke**[1]

[1]Marine Meteorology Department, GEOMAR Helmholtz Centre for Ocean Research Kiel, Kiel, Germany, [2]Faculty of Mathematics and Natural Sciences, Christian-Albrechts-Universität zu Kiel, Kiel, Germany

Key Points:

- Daily snapshots of TIL strength
- Synoptic-scale behavior of the TIL and shear/curl contributions to relative vorticity
- TIL within ridges in midlatitude winter is stronger than polar summer TIL

Supporting Information:

- Figures S1–S6

Correspondence to:
R. Pilch Kedzierski,
rpilch@geomar.de

Citation:
Pilch Kedzierski, R., K. Matthes, and K. Bumke (2015), Synoptic-scale behavior of the extratropical tropopause inversion layer, *Geophys. Res. Lett.*, *42*, 10,018–10,026, doi:10.1002/2015GL066409.

Received 1 OCT 2015
Accepted 29 OCT 2015

Abstract High-resolution GPS radio occultation temperature profiles from the COSMIC satellite mission (2007–2013) are used to obtain daily snapshots of the strength of the extratropical tropopause inversion layer (TIL). Its horizontal structure and day-to-day variability are linked to the synoptic situation at near-tropopause level. The strength of the TIL in cyclonic as well as anticyclonic conditions is investigated by separating relative vorticity into curl and shear terms. The analysis shows that the TIL has high zonal variability, and its strength is instantaneously adjusted to the synoptic situation at near-tropopause level. Our key finding is that the TIL within midlatitude ridges in winter is as strong as or stronger than the TIL in polar summer. The strongest TIL in anticyclonic conditions is related to the shear term, while the weaker TIL in cyclonic conditions is enhanced by the curl term.

1. Introduction

The extratropical tropopause inversion layer (TIL) is characterized by enhanced static stability and a strong temperature inversion in a thin layer of about 1 km depth right above the extratropical tropopause. The TIL was discovered via tropopause-based averaging [*Birner et al.*, 2002] and is a ubiquitous global phenomenon from high vertically resolved radiosonde observations [*Birner*, 2006] and satellite GPS radio occultation (GPS-RO) temperature profiles [*Grise et al.*, 2010].

The TIL receives increasing attention because its enhanced stability has implications for the vertical propagation of Rossby and small-scale gravity waves. Since a number of refraction indexes and wave theory approximations make use of static stability in their formulas, higher static stability would act to inhibit vertical wave propagation [see *Birner*, 2006, and references therein].

TIL seasonality, vertical structure, and strength are strongly correlated with observed gradients of stratospheric and tropospheric trace gases from aircraft [*Kunz et al.*, 2009; *Schmidt et al.*, 2010] and satellite measurements [*Hegglin et al.*, 2009]. Therefore, it is argued that the TIL plays an important role in stratosphere-troposphere exchange (STE), which determines stratospheric chemical composition and affects the radiation budget for surface climate. The relation is as follows: higher static stability inhibits vertical motion and correlates with sharper trace gas gradient which in turn inhibits STE.

Climatological studies have shown that the TIL is strongest in polar summer and also has a relative maximum in midlatitude winter [*Birner*, 2006; *Randel et al.*, 2007; *Randel and Wu*, 2010; *Grise et al.*, 2010]. The TIL is enhanced under anticyclonic conditions based on GPS-RO observations [*Randel et al.*, 2007; *Randel and Wu*, 2010]. Given that the temperature decreases with height up to the tropopause where the gradient is reversed, a dipole of cooling below the tropopause and warming above the tropopause is needed for the enhancement of the gradient right above the tropopause. Several hypotheses have been proposed about what mechanisms can produce this dipole and thus form and maintain the TIL:

1. Radiative effects: These involve longwave water vapor cooling below the tropopause and shortwave ozone warming above the tropopause due to their decreasing (increasing) concentration with height. This mechanism was first proposed by *Randel et al.* [2007]. Later the role of water vapor was found to be dominant [*Hegglin et al.*, 2009; *Kunz et al.*, 2009; *Randel and Wu*, 2010]. However, modeling studies by *Birner* [2010] and *Miyazaki et al.* [2010a] suggest that radiative effects are only important during summer.
2. Dynamics: The dipole consists of dynamical heating above the tropopause driven by the downwelling branch of the large-scale stratospheric residual circulation and cooling below the tropopause due to

Geophysical Research Letters 10.1002/2015GL066409

tropopause lifting by upper tropospheric eddies. *Birner* [2010] showed a TIL formation by including the dynamical effects of stratospheric residual circulation in a chemistry climate model, and a number of idealized modeling studies pointed to the importance of synoptic-scale dynamics alone: baroclinic waves and their embedded cyclones and anticyclones [*Wirth*, 2003, 2004; *Wirth and Szabo*, 2007; *Son and Polvani*, 2007] and specially baroclinic wave breaking events [*Erler and Wirth*, 2011] in the formation and enhancement of the TIL. Yet this dipole only explains the magnitude of the TIL found at midlatitudes, and the only observational studies making a direct link between TIL variability and dynamics are *Randel et al.* [2007] and *Randel and Wu* [2010] on the relationship between the TIL and near-tropopause cyclonic-anticyclonic relative vorticity. At small scales, a baroclinic life cycle experiment by *Kunkel et al.* [2014] showed transient enhancement of the TIL in the presence of gravity waves, which could persistently enhance/maintain the TIL via wave-mean flow interaction.

The current state of research suggests that the TIL, though a global phenomenon, has different formation processes which depend on latitude and season. The relative contribution of each was studied in a high-resolution model [*Miyazaki et al.*, 2010a, 2010b] and supports the idea that radiative effects are of importance only in polar summer while dynamics dominate otherwise.

The main goals of our study are to provide a first detailed observational picture of the TIL's real-time behavior and to gain insight into the role of synoptic-scale dynamics on the TIL formation and maintenance. We will contrast the polar summer TIL to the TIL found within baroclinic waves in winter. The high number of temperature profiles from GPS-RO observations from the COSMIC satellite mission [*Anthes et al.*, 2008] allows to derive daily snapshots of TIL properties at a sufficient horizontal resolution to be compared to the synoptic situation at near-tropopause level from ERA-Interim reanalysis [*Dee et al.*, 2011]. Also, we investigate the relationship between the TIL and cyclonic versus anticyclonic conditions by splitting relative vorticity into curl and shear terms. Shear represents pure horizontal wind gradient as from balanced adiabatic dynamics. Curl, an air parcel's spin, becomes important during the high-amplitude and breaking stages of a baroclinic wave [*Bell and Keyser*, 1993], and high values indicate flow imbalance [*Plougonven and Zhang*, 2014; *Kunkel et al.*, 2014]. Our interest is which term and its associated flow type enhances the TIL at different relative vorticity conditions.

In sections 2.1 and 2.2 we will explain, respectively, the methods to obtain TIL daily snapshots and to split relative vorticity into curl and shear terms. In section 3 the synoptic-scale behavior of the TIL will be analyzed; section 4 will discuss the relative contributions of curl and shear on the TIL relationship with cyclonic-anticyclonic relative vorticity; and section 5 will discuss and summarize the main findings.

2. Data and Methods

To derive TIL properties, we use temperature profiles from GPS-RO observations (COSMIC satellite mission [*Anthes et al.*, 2008]). The high vertical resolution of the GPS-RO temperature profiles (100 m spacing from the ground up to 40 km altitude) is comparable to that of high-resolution radiosondes, with the advantage of having weather independency and global coverage at a rate of ~2000 profiles per day. The wet temperature profiles we use (the "wetPrf" product) include the water vapor effect when retrieving temperature from the refractivity measured by the satellites, based on a 1D variational analysis using European Centre for Medium-Range Weather Forecasts (ECMWF) data. Higher concentrations or gradients of water vapor near the tropopause are not an error source this way. The "wetPrf" and dry temperature "atmPrf" profiles agree extremely well in a validation study by *Das and Pan* [2014], with absolute zero difference above the 200 hPa level. Less than 1% of the profiles is rejected by a preliminary quality control. Profiles with temperatures $>150°$C or $<-150°$C and those where the tropopause cannot be detected are not used to avoid unrealistic temperature gradients and/or TIL location.

The tropopause height (TP_z) is defined by the lapse-rate tropopause (LR TP) *World Meteorological Organization* [1957] criterion, unless stated otherwise. The near-TP synoptic situation is obtained from ERA-Interim reanalysis [*Dee et al.*, 2011]. The 200 hPa level was selected for comparison with earlier work about the TIL relationship with relative vorticity [*Randel et al.*, 2007; *Randel and Wu*, 2010]. Daily, 12 UTC fields of geopotential height and winds are retrieved from ERA-Interim on a $2.5° \times 2.5°$ longitude-latitude grid. Relative vorticity and its curl and shear terms are calculated from the wind fields. Our study was conducted for the time period 2007–2013.

2.1. TIL Strength and Mapping

Static-stability vertical profiles are obtained from the COSMIC temperature data, calculating the Brunt-Väisälä frequency squared (N^2 [s^{-2}]) with the following formula:

$$N^2 = g/\Theta \cdot \partial\Theta/\partial z$$

where g is the gravitational acceleration and Θ the potential temperature. As a measure of TIL strength, we use the maximum of the Brunt-Väisälä frequency squared (N^2_{max}) above the LR TP, following *Birner et al.* [2006], *Wirth and Szabo* [2007], and *Erler and Wirth* [2011].

N^2_{max} represents TP sharpness better than the temperature difference between TP_z and 2 km above used in *Randel et al.* [2007] and *Randel and Wu* [2010] in terms of physical meaning: it captures the maximum gradient of potential temperature, and N^2 is used in wave propagation/refraction indexes and wave theory approximations. Instead of averaging the N^2 profiles with respect to the tropopause, the simple mean of all their N^2_{max} is made directly for two reasons: (1) the N^2_{max} is not always located at the exact same distance from the tropopause and therefore gets diluted in the TP-based average profile; and (2) there exists a cyclone-anticyclone asymmetry between the LR TP (based on temperature gradient) and dynamical tropopause (based on a potential vorticity threshold) [*Wirth*, 2001], with increasing differences toward stronger cyclonic circulation. Taking the mean of N^2_{max} avoids these sources of indeterminacy. We allow our algorithm to find the N^2_{max} up to 3 km above the tropopause, although it is almost always found in the first 1–2 km.

TIL strength maps are displayed daily on a polar stereographic grid covering the area of 30°–90°N (41 × 41 grid points with ~3° spacing). All GPS-RO profiles of the corresponding day within a 1000 km radius from each grid point are used to obtain the grid's value. The 1000 km radius is chosen to minimize the number of gaps in our TIL strength maps and for smoothing purposes since it avoids small-scale structures that cannot be resolved with the COSMIC mission sampling density. These settings are well below the size of troughs/ridges that form within baroclinic waves at near-TP level in winter and therefore sufficient to follow their synoptic development.

2.2. Relative Vorticity and Split Into Curl and Shear

Relative vorticity (ζ) and its curl and shear terms are obtained by applying the notation developed in *Bell and Keyser* [1993] on ERA-Interim (daily 12 UTC 200 hPa) wind fields. Curl_ζ and Shear_ζ are calculated as follows:

$$\mathrm{Curl}_\zeta = 1/V^2[u^2 v_x - v^2 u_y - uv(u_x - v_y)] \qquad (1)$$

$$\mathrm{Shear}_\zeta = -1/V^2[u^2 u_y - v^2 v_x - uv(u_x - v_y)] \qquad (2)$$

where $V^2 = (u^2 + v^2)$ and the subscripts of u and v denote their partial derivatives with respect to x or y. This notation is very convenient since the sum of (1) and (2) gives $(v_x - u_y) = \zeta$.

The 200 hPa relative vorticity and geopotential height fields are interpolated from the original ERA-Interim longitude-latitude grid onto the polar stereographic projection used in our analysis. Examples of the spatial distribution of Curl_ζ and Shear_ζ compared to ζ are given in the supporting information (Figure S1).

When making diagrams of TIL strength versus relative vorticity, we follow the method by *Randel et al.* [2007] and *Randel and Wu* [2010], binning TIL properties regarding their collocated 200 hPa relative vorticity. We use 12 UTC daily ERA-Interim [*Dee et al.*, 2011] instead of daily National Centers for Environmental Prediction (NCEP) reanalysis fields [*Kalnay et al.*, 1996] and N^2_{max} as the measure of TIL strength instead of the temperature difference between the TP_z and 2 km above. For each value of ζ, a distribution of N^2_{max} from all GPS-RO profiles collocated with such relative vorticity is computed. The Curl_ζ and Shear_ζ terms are also binned for comparison. In each case ζ, Curl_ζ and Shear_ζ are binned alone, regardless of what value the other terms have.

3. Synoptic-Scale Behavior of the TIL From Daily Snapshots

The synoptic-scale behavior of the TIL strength (sTIL) is analyzed based on snapshots of different summer and winter days. To take near-TP synoptic variability into account, the examples chosen for this section are representative of a range of situations that can be found in summer and winter: stronger/weaker N^2_{max} peaks and

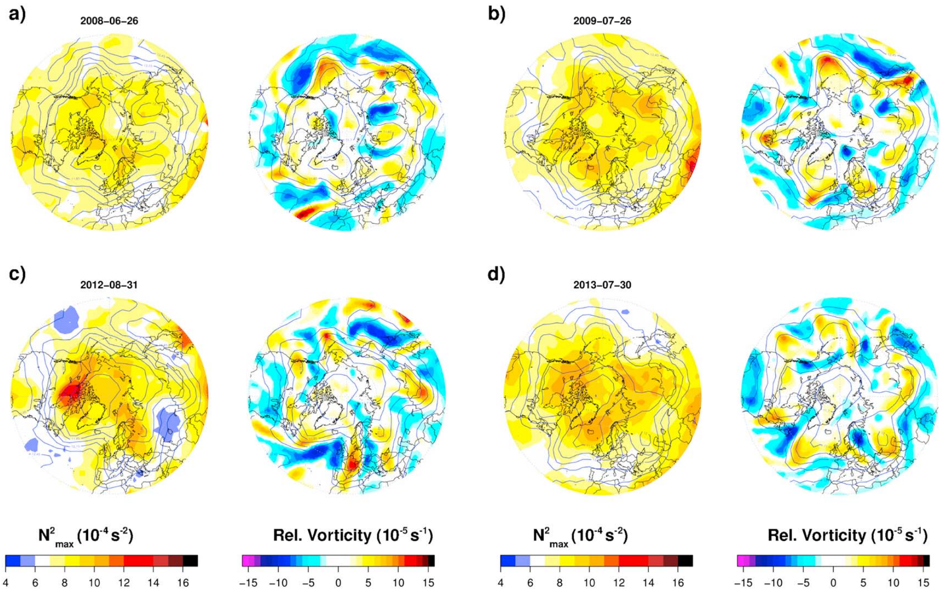

Figure 1. Polar stereographic maps of (first and third columns) daily TIL strength (N^2_{max}) and (second and fourth columns) 200 hPa relative vorticity, at different summer days. Corresponding color scales are at the bottom. Contour lines show 200 hPa geopotential height (in km with 150 m interval).

the presence of various zonal structures such as troughs and ridges of different wavelenghts and amplitudes. The results of this section are compared to earlier observational studies and climatologies [*Birner*, 2006; *Randel et al.*, 2007; *Randel and Wu*, 2010; *Grise et al.*, 2010], unless referred otherwise.

3.1. Summer Examples

Figure 1 shows four examples of sTIL daily snapshots during summer and the corresponding near-tropopause (12 UTC, 200 hPa) ζ and geopotential height fields of the same day. Note that due to our definition of sTIL via N^2_{max}, the magnitude of the sTIL is higher than in previous studies [*Birner*, 2006; *Randel et al.*, 2007; *Randel and Wu*, 2010; *Grise et al.*, 2010], differing about $2 \times 10^{-4}s^{-2}$.

In summer, the polar TIL is stronger than in midlatitudes. *Randel and Wu* [2010] showed that water vapor radiative effects dominate TIL formation in polar summer, since the highest upper tropospheric concentrations and cross-TP gradients are found then. The daily snapshots in Figure 1 reveal that the sTIL has high zonal and day-to-day variability, showing sTIL maxima collocated with anticyclonic relative vorticity. This is also in agreement with *Randel and Wu* [2010] who suggested that synoptic-scale dynamics shape the horizontal structure of the already strong polar summer TIL.

sTIL ranges typically between $8–10 \times 10^{-4}s^{-2}$ at polar regions and $6–7 \times 10^{-4}s^{-2}$ at midlatitudes. This is far away from typical stratospheric values ($\sim 4 \times 10^{-4}s^{-2}$) and supports the TIL as an absolutely ubiquitous feature in Northern Hemisphere (NH) summer. The weakest TIL found in some cases (Figure 1c, blue) has still values above $5 \times 10^{-4}s^{-2}$. In rare cases, the sTIL reaches more than $11 \times 10^{-4}s^{-2}$ (Figure 1c, red). Such events happen once per month on average and last 1–2 days.

3.2. Winter Examples

Figure 2 shows more sTIL snapshots from winter to compare with Figure 1 (summer). The geopotential height fields now show a stronger jet with larger-amplitude oscillations: well-defined troughs and ridges at midlatitudes. Due to the enhanced dynamic activity in midlatitude winters, we separated example days where the sTIL had very strong peaks (Figures 2a, 2c, 2e, and 2g) from days when it was weaker (Figures 2b, 2d, 2f, and 2h). The magnitude of N^2_{max} suggests that the TIL in NH winter is always present. Values below $5 \times 10^{-4}s^{-2}$ are only found in SH winter in the polar vortex region (see supporting information Figure S3).

In winter midlatitudes, the TIL is, in general, stronger than near the pole in agreement with previous climatologies [*Birner*, 2006; *Randel et al.*, 2007; *Randel and Wu*, 2010; *Grise et al.*, 2010] due to the increased

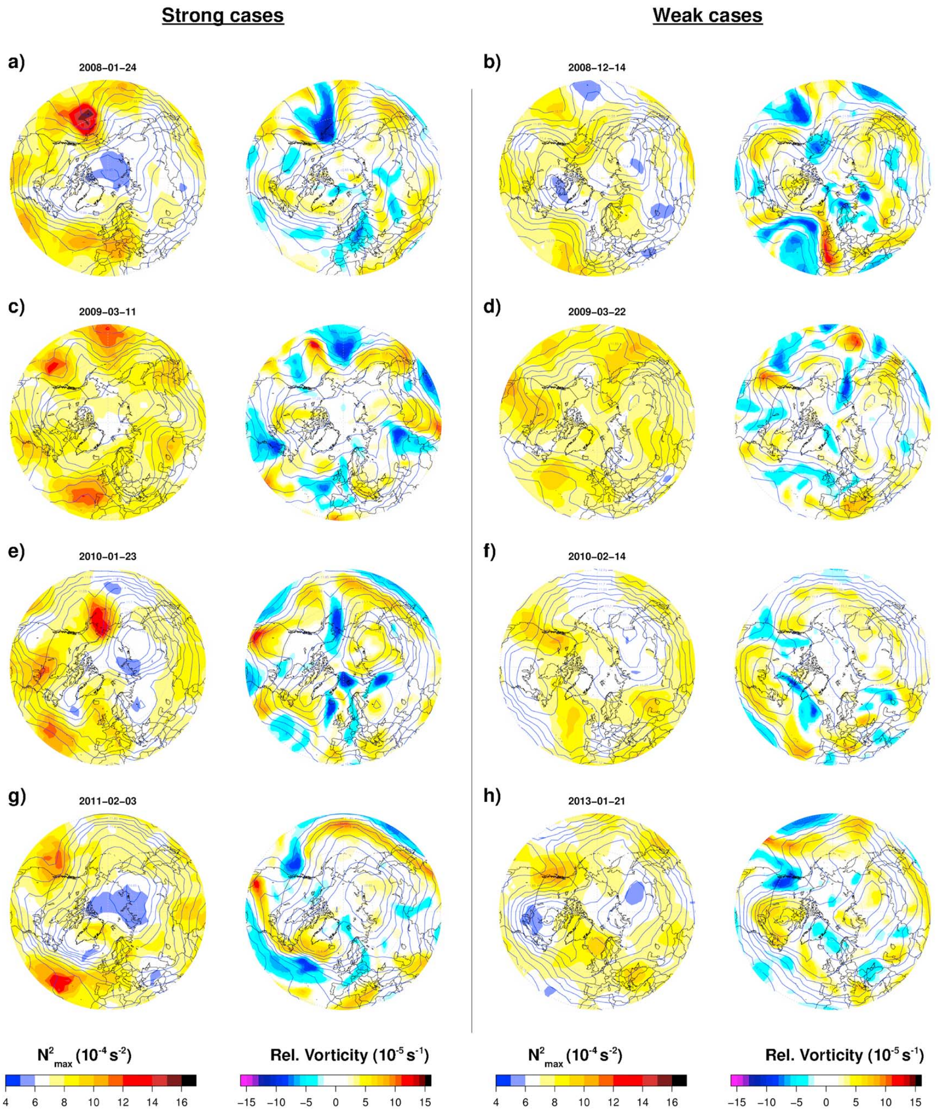

Figure 2. Same as Figure 1, but for different winter days. Separated are examples of situations with (a, c, e, and g) stronger N^2_{max} peaks and (b, d, f, and h) weaker N^2_{max} peaks.

stratospheric circulation in the winter hemisphere and upper tropospheric baroclinic wave activity at midlatitudes. The TIL adjusts to the synoptic circulation, showing a big trough-ridge contrast. Lower values of $6–7 \times 10^{-4}\text{s}^{-2}$ are found within troughs and peaks of at least $8–10 \times 10^{-4}\text{s}^{-2}$ within ridges (Figures 2b, 2d, 2f, and 2h), while the sTIL at polar regions is about $5–7 \times 10^{-4}\text{s}^{-2}$. The sTIL quite often reaches more than $12 \times 10^{-4}\text{s}^{-2}$ within midlatitude ridges, and depending on the wave structure of the jet, one (Figure 2a) or multiple strong peaks (Figures 2c, 2e, and 2g) can appear. As in summer, those strong peaks last for 1–2 days but are present more often: about 25% of all days. The trough-ridge contrast from Figure 2 is coherent with the TIL zonal structures derived from reanalysis by *Gettelman and Wang* [2015].

Why is the TIL within ridges in midlatitude winter of the same magnitude or stronger than in polar summer? During winter the stratospheric residual circulation is strongest (producing dynamical heating above the TP), tropopause lifting and cooling by upper-tropospheric eddies are strongest at midlatitudes (and especially within ridges since they have higher and colder TP), and even radiative cooling from cirrus clouds or high humidity at near-TP level is possible. *Taylor et al.* [2011] showed a case study of a nonconvective cirrus cloud associated with a negative temperature anomaly, and *Biondi et al.* [2012] studied the temperature inversion generally found at cloud tops with GPS-RO data.

While all three mechanisms can act together in ridges, this is not the case in troughs (lower TP, no high cirrus clouds) or polar summer (upper tropospheric eddies and stratospheric circulation are both weaker despite the stronger water vapor radiative cooling).

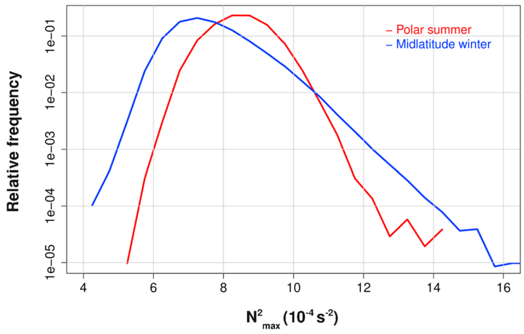

Figure 3. Histogram with relative frequencies of TIL strength (N^2_{max}), comparing Northern Hemisphere polar summer (red line, JJAS 70°−90°N) with midlatitude winter (blue line, DJFM 30°−60°N).

3.3. Polar Summer Versus Midlatitude Winter

Figure 3 summarizes the results from sections 3.1 and 3.2, showing the relative frequency of N^2_{max} in polar summer (red line) and midlatitude winter (blue line). The N^2_{max} occurrence is computed relative to all grid boxes (from maps as in Figures 1 and 2) within the selected latitudes and time. The seasonal mean state of the sTIL in polar summer ($8.5 \times 10^{-4}s^{-2}$) is stronger than in midlatitude winter ($7.6 \times 10^{-4}s^{-2}$). Note that the distributions are shown on a log-*y* scale, and due to the large sample size (2007−2013, daily for each season, multiple grid points, less area/grids in polar regions), this difference is very significant: 100 standard deviations of the distributions' means are $0.25 \times 10^{-4}s^{-2}$ for summer and $0.12 \times 10^{-4}s^{-2}$ for winter.

The midlatitude winter distribution (though having a lower mean) is much broader and skewed toward higher N^2_{max} values, which only occur within ridges as shown in the previous section. sTIL values surpassing the summer mean ($8.5 \times 10^{-4}s^{-2}$) represent an integrated relative frequency of 19.14% in the midlatitude winter distribution. Values above $10 \times 10^{-4}s^{-2}$ amount for a 3.24%, and the strongest peaks above $11 \times 10^{-4}s^{-2}$ are more frequent in midlatitude winter than in polar summer.

In summary, the synoptic-scale features shown in this section reveal that the strongest TIL is found in midlatitude winter, within ridges. Even in the weakest cases, the sTIL within midlatitude ridges in winter (Figure 2) is of the same magnitude ($8-10 \times 10^{-4}s^{-2}$) as in polar summer (Figure 1), and the strongest sTIL peaks are more frequent and reach higher values within winter ridges compared to polar summer (Figure 3). Due to the big trough-ridge contrast (weak-strong TIL), the zonal mean sTIL in midlatitude winter is weaker than in polar summer (Figure 3), in agreement with earlier climatologies [*Birner*, 2006; *Randel et al.*, 2007; *Randel and Wu*, 2010; *Grise et al.*, 2010].

All results from this section are also applicable to the Southern Hemisphere extratropical TIL. Plots similar to Figures 1−3 can be found in the supporting information (Figures S2−S4).

4. The Role of Curl and Shear Relative Vorticity

Figures 4a and 4b show diagrams of TIL strength (N^2_{max}) related to relative vorticity for polar summer and midlatitude winter, respectively. Thick lines show the mean N^2_{max} for each relative vorticity bin, while the vertical thin lines show one standard deviation of the bin's N^2_{max} distribution's mean. The black lines (total relative vorticity) in Figure 4b correspond to the results from *Randel et al.* [2007] and those in Figure 4a to the ones from *Randel and Wu* [2010]. Even using different reanalysis data and a different measure for the sTIL, its relationship with ζ is in very good agreement with those earlier studies: sTIL increases toward anticyclonic conditions in a very similar manner. Due to the larger sample size, high measure density by COSMIC mission [*Anthes et al.*, 2008] and a longer time period (2007−2013), a wider range of ζ can be explored.

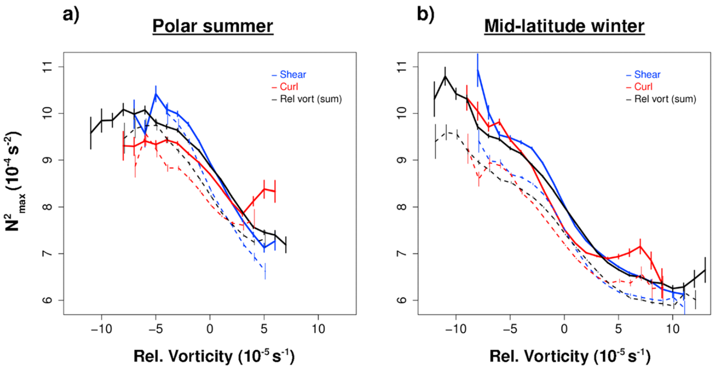

Figure 4. Diagrams of TIL strength (N^2_{max}) versus relative vorticity. (a) Polar summer (JAS 70°–90°N) and (b) midlatitude winter (JFM 30°–60°N). Blue, red, and black lines denote, respectively, shear, curl, and total relative vorticity. Dashed lines correspond to Southern Hemisphere seasons (summer JFM and winter JAS). Vertical bars denote one standard deviation of the mean value.

4.1. Curl in Cyclonic Circulation

The red and blue lines in Figure 4 correspond to the Curl$_\zeta$ and Shear$_\zeta$ terms. Figure 4 shows that the general tendency of decreasing sTIL with stronger cyclonic circulation is not followed by the Curl$_\zeta$ term (red line): the relation gets inverted at the strongest cyclonic Curl$_\zeta$ with values showing enhanced sTIL.

Nonlinear growth and breaking of baroclinic waves can generate high Curl$_\zeta$ amounts [*Bell and Keyser*, 1993], and the behavior of the Curl$_\zeta$ line in Figure 4 is particularly similar to the N^2_{max} versus relative vorticity relation described by *Erler and Wirth* [2011] after the anticyclonic breaking (LC1 type) of a baroclinic wave. Our results suggest that processes related to baroclinic wave growth and breaking (e.g., flow imbalance or gravity wave presence) [*Plougonven and Zhang*, 2014; *Kunkel et al.*, 2014] are responsible for the enhancement of the weaker TIL within cyclones.

4.2. Shear in Anticyclonic Circulation

Curl$_\zeta$ (red) and Shear$_\zeta$ (blue) terms in Figure 4 differ increasingly toward stronger anticyclonic conditions. Strong anticyclonic Shear$_\zeta$ is related to higher values of N^2_{max}. The difference of the mean sTIL at the same values of Curl$_\zeta$ and Shear$_\zeta$ is significant in Figure 4a: the blue and red lines are separated by more than one standard deviation (vertical lines). For midlatitude winter sTIL (Figure 4b) the lines differ less, though having the same tendency. The same behavior is observed regarding TP$_z$, with anticyclonic shear related to the highest TP$_z$ (see supporting information Figure S5) and differing significantly from the Curl$_\zeta$ term at any season. Polar winter has a similar behavior as in Figure 4a, and midlatitude summer resembles Figure 4b (see supporting information Figure S6).

Wirth [2003] explained the stronger TIL in anticyclones by hydrostatic and gradient wind balance. Since the wind shear dominates this balance, our results for the shear term further support these dynamics in producing the strong TIL within anticyclonic conditions. *Wirth* [2004] showed that the same dynamics, apart from making the tropopause higher and colder in the anticyclone, also form a secondary circulation with downwelling and convergence of vertical wind above the anticyclone, bringing the isentropes closer, increasing the potential temperature gradient and thus further stabilizing the TIL region.

As in section 3, the results of this section also apply to the Southern Hemisphere. The roles of the Curl$_\zeta$ and Shear$_\zeta$ terms are very similar (dashed lines in Figure 4, and supporting information Figures S5 and S6).

5. Concluding Remarks

Our study analyzed the TIL real-time behavior, showing important features adjusted to the synoptic situation at near-tropopause level, especially a strong trough-ridge contrast in midlatitude winter. The key finding of our study is that the TIL within midlatitude winter ridges is always as strong or even stronger than in polar summer. This means that while the climatological TIL is strongest in polar summer [*Birner*, 2006; *Randel et al.*, 2007; *Randel and Wu*, 2010; *Grise et al.*, 2010], this is no longer the case at the synoptic scale. This highlights the importance of synoptic-scale dynamics for the formation of the TIL.

We expanded the work by *Randel et al.* [2007] and *Randel and Wu* [2010] on the relationship of sTIL with relative vorticity. Shear relative vorticity is related to the strongest TIL in anticyclonic conditions, especially at polar latitudes, while the weaker TIL within cyclones is enhanced under the Curl_ζ term. This suggests that the processes responsible for the TIL enhancement are different in anticyclones (balanced hydrostatic dynamics) and cyclones (related to baroclinic wave growth and breaking).

All these findings also apply for the Southern Hemisphere. We are aware that the 200 hPa level chosen as the near-tropopause synoptic situation is often quite above the tropopause and more representative of the lowermost stratosphere: there is high variability in TP_z at midlatitudes, and TP_z at polar regions is typically below 250 hPa even in summer [*Son et al.*, 2011]. Nevertheless, it is very useful for comparison with earlier studies about the TIL.

Acknowledgments

This study was completed within the Helmholtz University Young Investigators Group NATHAN project, funded by the Helmholtz Association through the president's Initiative and Networking Fund and the GEOMAR, Helmholtz Centre for Ocean Research Kiel. We thank the ECMWF data server for the free availability of ERA-Interim data and UCAR for the COSMIC satellite mission temperature profiles. We are grateful to two anonymous reviewers for their valuable comments. We also appreciate the assistance accessing different data sets and discussions in the early stages of this study by Wuke Wang and Sebastian Wahl.

References

Anthes, R. A., et al. (2008), The COSMIC/FORMOSAT-3 mission: Early results, *Bull. Am. Meteorol. Soc.*, *89*, 313–333, doi:10.1175/BAMS-89-3-313.

Bell, G. D., and D. Keyser (1993), Shear and curvature vorticity and potential-vorticity interchanges: Interpretation and application to a cutoff cyclone event, *Mon. Weather Rev.*, *121*, 76–102, doi:10.1175/1520-0493(1993)121<0076:SACVAP>2.0.CO;2.

Biondi, R., W. J. Randel, S.-P. Ho, T. Neubert, and S. Syndergaard (2012), Thermal structure of intense convective clouds derived from GPS radio occultations, *Atmos. Chem. Phys.*, *12*, 5309–5318, doi:10.5194/acp-12-5309-2012.

Birner, T. (2006), Fine-scale structure of the extratropical tropopause region, *J. Geophys. Res.*, *111*, D04104, doi:10.1029/2005JD006301.

Birner, T. (2010), Residual circulation and tropopause structure, *J. Atmos. Sci.*, *67*, 2582–2600, doi:10.1175/2010JAS3287.1.

Birner, T., A. Dörnbrack, and U. Schumann (2002), How sharp is the tropopause at midlatitudes?, *Geophys. Res. Lett.*, *29*, 1700, doi:10.1029/2002GL015142.

Birner, T., D. Sankey, and T. G. Shepherd (2006), The tropopause inversion layer in models and analyses, *Geophys. Res. Lett.*, *33*, L14804, doi:10.1029/2006GL026549.

Das, U., and C. J. Pan (2014), Validation of FORMOSAT-3/COSMIC level 2 "atmPrf" global temperature data in the stratosphere, *Atmos. Meas. Tech.*, *7*, 731–742, doi:10.5194/amt-7-731-2014.

Dee, D. P., et al. (2011), The ERA-Interim reanalysis: Configuration and performance of the data assimilation system, *Q. J. R. Meteorol. Soc.*, *137*, 553–597, doi:10.1002/qj.828.

Erler, A. R., and V. Wirth (2011), The static stability of the tropopause region in adiabatic baroclinic life cycle experiments, *J. Atmos. Sci.*, *68*, 1178–1193, doi:10.1175/2010JAS3694.1.

Gettelman, A., and T. Wang (2015), Structural diagnostics of the tropopause inversion layer and its evolution, *J. Geophys. Res. Atmos.*, *120*, 46–62, doi:10.1002/2014JD021846.

Grise, K. M., D. W. J. Thompson, and T. Birner (2010), A global survey of static stability in the stratosphere and upper troposphere, *J. Clim.*, *23*, 2275–2292, doi:10.1175/2009JCLI3369.1.

Hegglin, M. I., C. D. Boone, G. L. Manney, and K. A. Walker (2009), A global view of the extratropical tropopause transition layer from Atmospheric Chemistry Experiment Fourier Transform Spectrometer O_3, H_2O, and CO, *J. Geophys. Res.*, *114*, D00B11, doi:10.1029/2008JD009984.

Kalnay, E., et al. (1996), The NCEP/NCAR 40-Year Reanalysis Project, *Bull. Am. Meteorol. Soc.*, *77*, 437–472, doi:10.1175/1520-0477(1996)077<0437:TNYRP>2.0.CO;2.

Kunkel, D., P. Hoor, and V. Wirth (2014), Can inertia-gravity waves persistently alter the tropopause inversion layer?, *Geophys. Res. Lett.*, *41*, 7822–7829, doi:10.1002/2014GL061970.

Kunz, A., P. Konopka, R. Müller, L. L. Pan, C. Schiller, and F. Rohrer (2009), High static stability in the mixing layer above the extratropical tropopause, *J. Geophys. Res.*, *114*, D16305, doi:10.1029/2009JD011840.

Miyazaki, K., S. Watanabe, Y. Kawatani, Y. Tomikawa, M. Takahashi, and K. Sato (2010a), Transport and mixing in the extratropical tropopause region in a high-vertical-resolution GCM. Part I: Potential vorticity and heat budget analysis, *J. Atmos. Sci.*, *67*, 1293–1314, doi:10.1175/2009JAS3221.1.

Miyazaki, K., S. Watanabe, Y. Kawatani, K. Sato, Y. Tomikawa, and M. Takahashi (2010b), Transport and mixing in the extratropical tropopause region in a high-vertical-resolution GCM. Part II: Relative importance of large-scale and small-scale dynamics, *J. Atmos. Sci.*, *67*, 1315–1336, doi:10.1175/2009JAS3334.1.

Plougonven, R., and F. Zhang (2014), Internal gravity waves from atmospheric jets and fronts, *Rev. Geophys.*, *52*, 33–76, doi:10.1002/2012RG000419.

Randel, W. J., and F. Wu (2010), The polar summer tropopause inversion layer, *J. Atmos. Sci.*, *67*, 2572–2581, doi:10.1175/2010JAS3430.1.

Randel, W. J., F. Wu, and P. Forster (2007), The extratropical tropopause inversion layer: Global observations with GPS data, and a radiative forcing mechanism, *J. Atmos. Sci.*, *64*, 4489–4496, doi:10.1175/2007JAS2412.1.

Schmidt, T., J.-P. Cammas, H. G. J. Smit, S. Heise, J. Wickert, and A. Haser (2010), Observational characteristics of the tropopause inversion layer derived from CHAMP/GRACE radio occultations and MOZAIC aircraft data, *J. Geophys. Res.*, *115*, D24304, doi:10.1029/2010JD014284.

Son, S.-W., and L. M. Polvani (2007), Dynamical formation of an extra-tropical tropopause inversion layer in a relatively simple general circulation model, *Geophys. Res. Lett.*, *34*, L17806, doi:10.1029/2007GL030564.

Son, S.-W., N. F. Tandon, and L. M. Polvani (2011), The fine-scale structure of the global tropopause derived from COSMIC GPS radio occultation measurements, *J. Geophys. Res.*, *116*, D20113, doi:10.1029/2011JD016030.

Taylor, J. R., W. J. Randel, and E. J. Jensen (2011), Cirrus cloud-temperature interactions in the tropical tropopause layer: A case study, *Atmos. Chem. Phys.*, *11*, 10,085–10,095, doi:10.5194/acp-11-10085-2011.

Wirth, V. (2001), Cyclone-anticyclone asymmetry concerning the height of the thermal and the dynamical tropopause, *J. Atmos. Sci.*, *58*, 26–37, doi:10.1175/1520-0469(2001)058<0026:CAACTH>2.0.CO;2.

Wirth, V. (2003), Static stability in the extratropical tropopause region, *J. Atmos. Sci.*, *60*, 1395–1409, doi:10.1175/1520-0469(2003)060<1395:SSITET>2.0.CO;2.

Wirth, V. (2004), A dynamical mechanism for tropopause sharpening, *Meteorol. Z.*, *13*, 477–484, doi:10.1127/0941-2948/2004/0013-0477.

Wirth, V., and T. Szabo (2007), Sharpness of the extratropical tropopause in baroclinic life cycle experiments, *Geophys. Res. Lett.*, *34*, L02809, doi:10.1029/2006GL028369.

World Meteorological Organization (1957), Meteorology—A three-dimensional science, *WMO Bull.*, *6*, 134–138.

GEOPHYSICAL RESEARCH LETTERS

Supporting Information for "Synoptic-scale Behavior of the Extratropical Tropopause Inversion Layer"

Robin Pilch Kedzierski[1], Katja Matthes[1,2], Karl Bumke[1]

Corresponding author: R. Pilch Kedzierski, Maritime Meteorology Department, GEOMAR Helmholtz Centre for Ocean Research Kiel, Düsternbrooker Weg 20, D-24105 Kiel (Germany) (rpilch@geomar.de)

[1]Marine Meteorology Department,
GEOMAR Helmholtz Centre for Ocean
Research Kiel, Kiel, Germany.

[2]Christian-Albrechts-Universität zu Kiel,
Kiel, Germany.

1. Overview

SI Figure 1 provides examples of the spatial distribution of the $Curl_{rv}$ and $Shear_{rv}$ terms compared to relative vorticity, with the split formulation explained in section 2.2 of the main article.

SI Figures 2, 3 and 4 are the Southern Hemisphere counterparts of Figs. 1, 2 and 3 in section 3 of the main article.

SI Figure 5 shows TP_z vs. relative vorticity diagrams, as Fig.4 in the main article for N^2_{max}.

SI Figure 6 shows diagrams for polar winter and mid-latitude summer, to complete section 4 of the main article where polar summer and mid-latitude winter are shown.

2. Comments on SI Figures 5 and 6

The wider ζ range reveals an S-shaped curve of tropopause height at mid-latitudes in winter (SI Fig. 5b) and summer (SI Fig. 6d). TP_z starts increasing at very strong cyclonic conditions, but also decreases at very strong anticyclonic conditions. This could be explained by the fact that the strongest anticyclonic and cyclonic relative vorticity values are usually found close and parallel to the jet stream, that separates troughs from ridges in a baroclinic wave. Those areas don't have the highest/lowest TP_z, but a strong TP_z slope. The higest (lowest) TP_z is located towards the center of a ridge (trough), where relative vorticity values are more modest.

Although less clear, a similar tendency is observed in polar winter (SI Fig. 6c), also attributable to baroclinic wave activity there.

Another issue is that the Lapse-Rate TP_z is not very reliable under very strong cyclonic conditions, which could explain the strange behavior of the TP_z vs relative vorticity lines (and the curl/shear terms) in SI Figures 5 and 6.

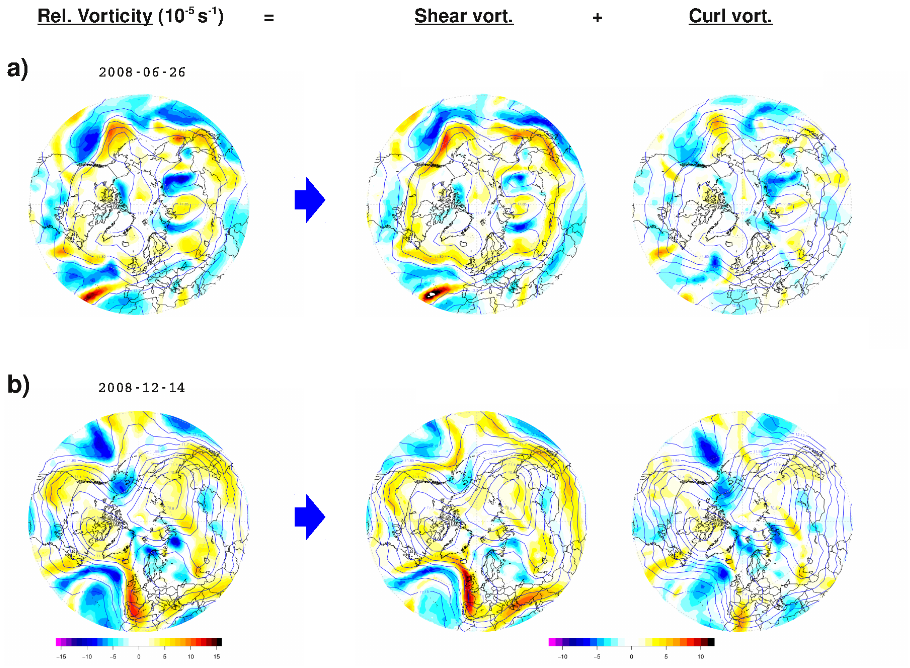

Figure 1. Examples of relative vorticity split into curl and shear terms. (a) corresponds to the same day as in Fig.1a in the main article, and (b) corresponds to Fig.2b.

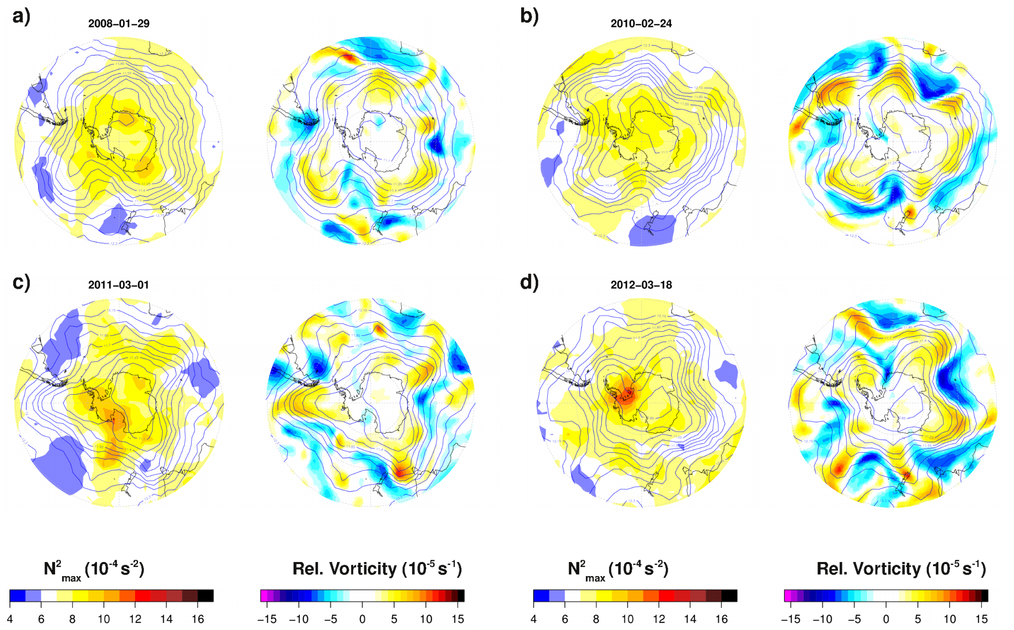

Figure 2. Southern Hemisphere polar stereographic maps of daily TIL strength (N^2_{max}, 1^{st} and 3^{rd} columns) and 200hPa relative vorticity (2^{nd} and 4^{th} columns), at different summer days. Corresponding color scales are at the bottom. Contour lines show 200hPa geopotential height (in km' with 150m' interval).

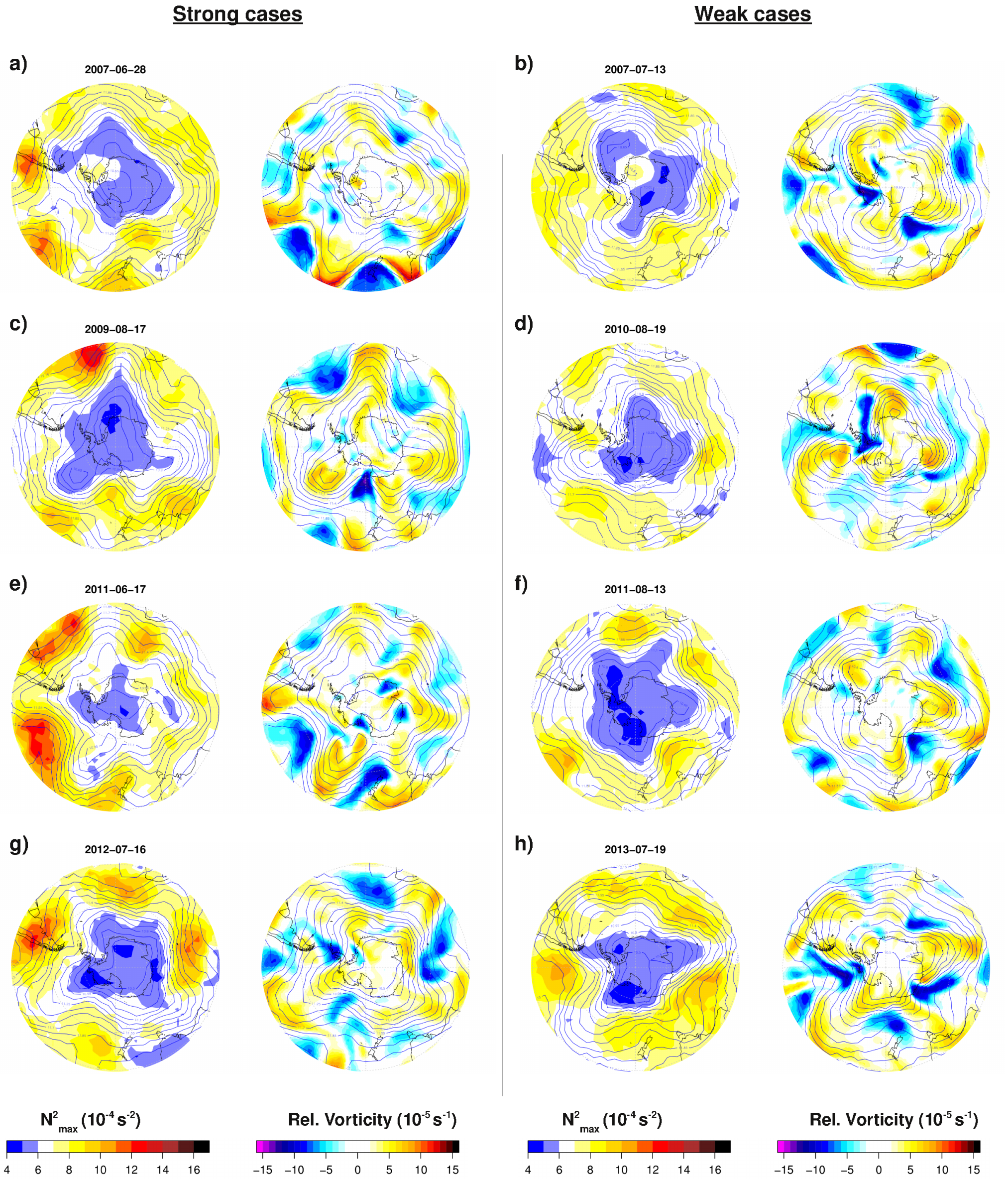

Figure 3. Same as SI Figure 2, but for different winter days in the Southern Hemisphere. Separated are examples of situations with stronger N^2_{max} peaks (on the left side: a,c,e,g), and weaker N^2_{max} peaks (on the right side: b,d,f,h).

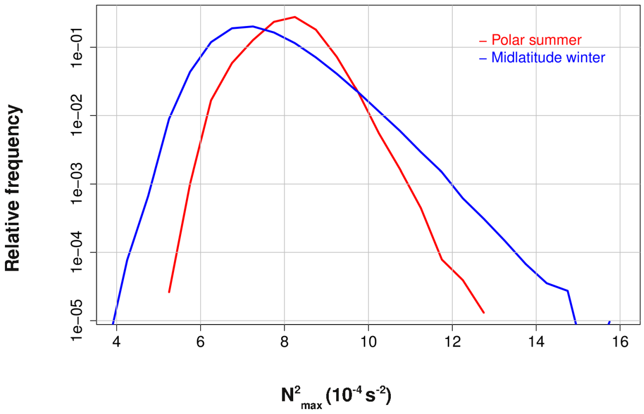

Figure 4. Histogram with relative frequencies of TIL strength (N^2_{max}), comparing Southern Hemisphere polar summer (red line, JFM 70°-90°S) with mid-latitude winter (blue line, JJA 30°-60°S).

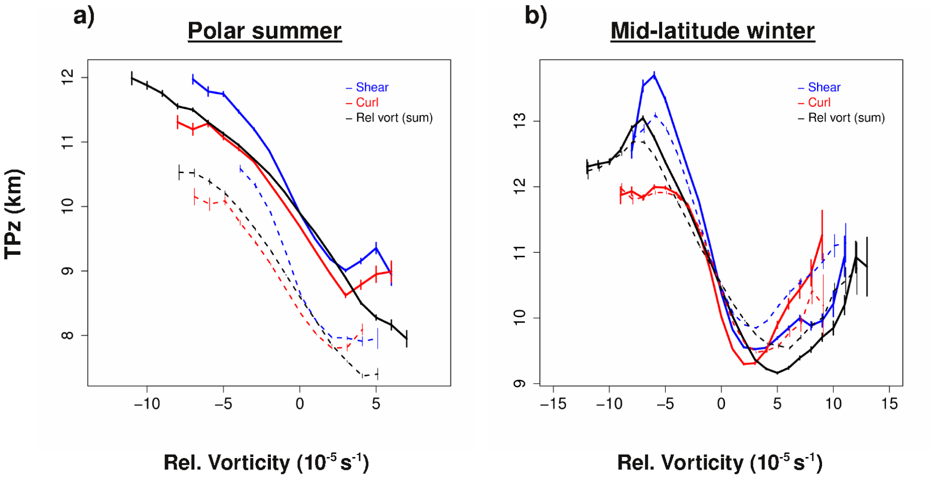

Figure 5. Diagrams of tropopause height versus relative vorticity. (a) belongs to polar summer (JAS 70°-90°N), and (b) to mid-latitude winter (JFM 30°-60°N). Blue, red and black lines denote, respectively: shear, curl and total relative vorticity. Dashed lines correspond to Southern Hemisphere seasons (SH summer JFM, SH winter JAS). Vertical bars denote one standard deviation of the mean value.

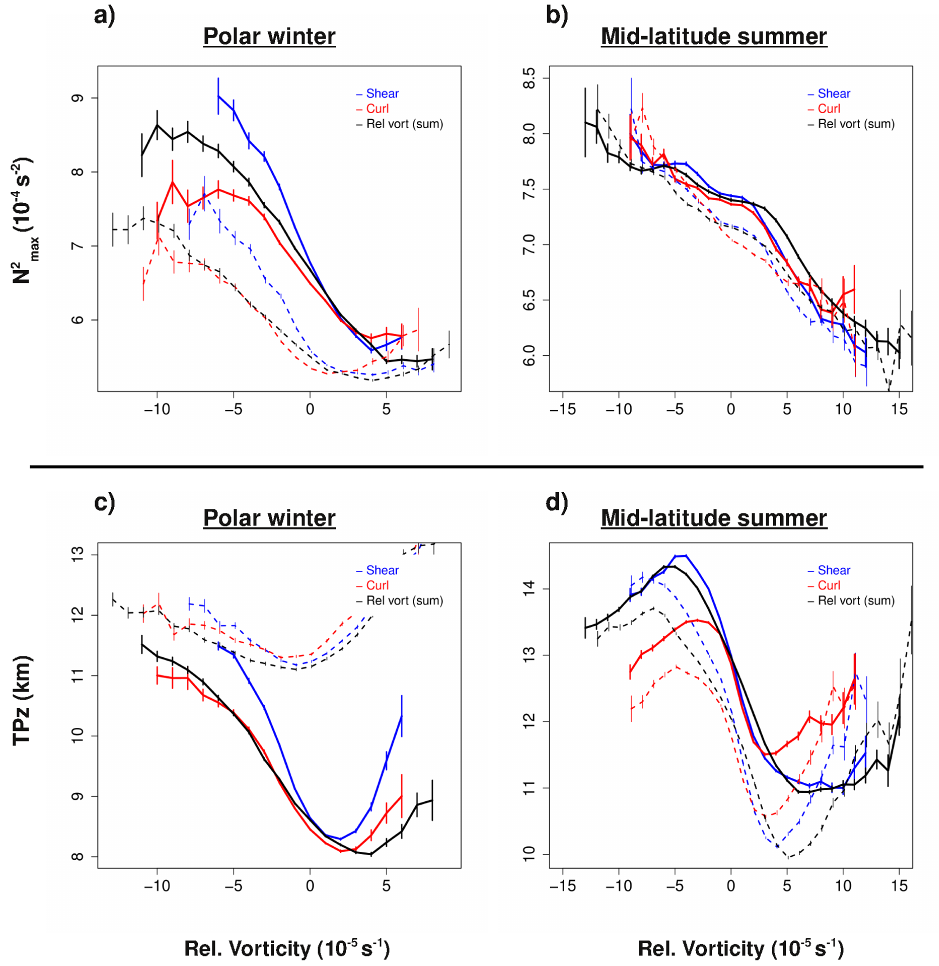

Figure 6. Diagrams of TIL strength (N^2_{max}, top row) and tropopause height (bottom row) versus relative vorticity. Left column belongs to polar winter (JFM 70°-90°N), and the right column to mid-latitude summer (JAS 30°-60°N). Blue, red and black lines denote, respectively: shear, curl and total relative vorticity. Dashed lines correspond to Southern Hemisphere seasons (SH winter JAS, SH summer JFM). Vertical bars denote one standard deviation of the mean value.

4.2 Wave Modulation of the Extratropical Tropopause Inversion Layer

Citation:

Pilch Kedzierski, R., K. Matthes, and K. Bumke (2016b), Wave modulation of the extratropical tropopause inversion layer, *Atmospheric Chemistry and Physics Discussions*, pp. 1-31, (submitted).

Author contributions to this publication:

- R. Pilch Kedzierski initiated the study, designed the method, did the analysis, produced all the figures and wrote the manuscript.
- K. Matthes contributed with ideas and discussions on the analysis, and commented the manuscript.
- K. Bumke contributed with ideas and discussions on the analysis, and commented the manuscript.

Manuscript prepared for Atmos. Chem. Phys.
with version 2015/04/24 7.83 Copernicus papers of the LaTeX class copernicus.cls.
Date: 2 August 2016

Wave Modulation of the Extratropical Tropopause Inversion Layer

Robin Pilch Kedzierski[1], Katja Matthes[1,2], and Karl Bumke[1]

[1]Marine Meteorology Department, GEOMAR Helmholtz Centre for Ocean Research Kiel, Kiel, Germany.
[2]Faculty of Mathematics and Natural Sciences, Christian-Albrechts-Universität zu Kiel, Kiel, Germany.

Correspondence to: Robin Pilch Kedzierski (rpilch@geomar.de)

Abstract.

This study aims to quantify how much of the extratropical Tropopause Inversion Layer (TIL) comes from the modulation by planetary and synoptic-scale waves. By analyzing high-resolution observations, it also puts other TIL enhancing mechanisms into context.

Using gridded COSMIC GPS-RO temperature profiles from 2007-2013 we are able to extract the extratropical wave signal by a simplified wavenumber-frequency domain filtering method, and to quantify the resulting TIL enhancement. By subtracting the extratropical wave signal, we show how much of the TIL is associated with other processes, at mid and high latitudes, for both Hemispheres and all seasons.

The instantaneous modulation by planetary and synoptic-scale waves is almost entirely responsible for the TIL in mid-latitudes. This means that wave-mean flow interactions, inertia-gravity waves or the residual circulation are of minor importance in mid-latitudes.

At polar regions, the extratropical wave modulation is dominant for the TIL strength as well, but there is also a clear fingerprint from sudden stratospheric warmings (SSWs) and final warmings in both hemispheres. Therefore, polar vortex breakups are partially responsible for the observed polar TIL strength in winter (if SSWs occur) and spring. Also, part of the polar summer TIL strength cannot be explained by extratropical wave modulation.

After many modelling studies that proposed different TIL enhancing mechanisms in the last decade, our study finally identifies which processes dominate the extratropical TIL strength and their relative contribution, by analyzing observations only. It remains to be determined, however, which roles the different planetary and synoptic-scale wave types play within the total extratropical wave modulation of the TIL; and what causes the observed amplification of extratropical waves near the tropopause.

1 Introduction

The extratropical Tropopause Inversion Layer (TIL) is a strong temperature inversion at the extratropical tropopause with a corresponding static stability maximum right above. It is a fine-scale feature discovered via tropopause-based averaging (Birner et al., 2002; Birner, 2006), consisting of a thin layer of about 1km depth. Satellite Global Positioning System radio occultation observations (GPS-RO) show that the TIL is present at all latitudes (Grise et al., 2010).

The TIL is established as an important feature of the extratropical upper troposphere and lower stratosphere (UTLS) (Gettelman et al., 2011), and it is of interest to the scientific community for the following reasons: high static stability values theoretically affect the dispersion relations of atmospheric waves like Rossby or Inertia-Gravity waves since this parameter is part of different wave theory approximations (see Birner (2006); Grise et al. (2010) and references therein). In an idealized model experiment, Sjoberg and Birner (2014) showed that the TIL acts as a partial barrier for upward wave propagation. The study by Zhang et al. (2015) supports this hypothesis by showing inhibited upward propagation of Inertia-Gravity waves (IGW) due to the TIL, with data from a single US radiosonde station. Also, the TIL shall inhibit the cross-tropopause exchange of chemical compounds: high static stability suppresses vertical motion and is correlated with strong trace gas gradients (Hegglin et al., 2009; Kunz et al., 2009; Schmidt et al., 2010). In the next paragraphs we shortly review what is known so far about the observed variability of the extratropical TIL and the mechanisms proposed for its formation/enhancement.

Climatological studies about the seasonal, zonal-mean state of the TIL show that it reaches maximum strength during polar summer while it displays a weaker relative maximum in winter mid-latitudes (Birner, 2006; Randel et al., 2007; Randel and Wu, 2010; Grise et al., 2010). From a synoptic-scale perspective, the TIL in mid-latitude winter has very pronounced zonal structures, and the TIL within ridges (anticyclones) in mid-latitude winter has the same strength or even higher than any TIL observed in polar summer (Pilch Kedzierski et al., 2015). The cyclone-anticyclone modulation with weaker-stronger TIL is found at all extratropical latitudes and seasons (Randel et al., 2007; Randel and Wu, 2010; Pilch Kedzierski et al., 2015).

Different mechanisms are responsible for the formation/maintenance of the extratropical TIL:

- Radiative cooling below the tropopause by water vapor due to its strong gradient across the tropopause acts to enhance the TIL (Randel et al., 2007; Hegglin et al., 2009; Kunz et al., 2009; Randel and Wu, 2010), and a high-resolution model study by Miyazaki et al. (2010b, a) showed that radiative effects are dominant in polar summer, while dynamics enhance the TIL otherwise.

- The downwelling branch of the stratospheric residual circulation was proposed to cause dynamical heating above the tropopause and TIL enhancement in a model experiment by Birner (2010). The first evidence of this was found by Wargan and Coy (2016) at high latitudes following major sudden stratospheric warmings (mSSW), mainly caused by the convergence of the vertical component of the residual circulation ($\overline{w*}$). During a mSSW there is an acceleration of the residual circulation, and the enhanced $\overline{w*}$ convergence is the reason of the downward-propagating positive temperature anomaly (Andrews et al., 1987), which in turn enhances the high-latitude TIL once the signal reaches the lowermost stratosphere in winter or spring.

- Baroclinic waves and their embedded cyclones-anticyclones can enhance the TIL by tropopause lifting and cooling, and also warming above the tropopause in anticyclones from vertical wind convergence (from model experiments by Wirth (2003, 2004); Wirth and Szabo (2007); Son and Polvani (2007)). These synoptic-scale dynamics partly explain the seasonality and latitude-dependence of the extratropical TIL strength. Also, the baroclinic life-cycle experiment by Erler and Wirth (2011) showed the importance of baroclinic wave breaking events in enhancing the TIL. However, so far there is only observational evidence of the role of synoptic-scale dynamics in the cyclone-anticyclone modulation of the (weaker-stronger) TIL (Randel et al., 2007; Randel and Wu, 2010; Pilch Kedzierski et al., 2015).

- And finally, small-scale inertia-gravity waves (IGW) also play a role in enhancing the TIL. Kunkel et al. (2014) showed transient TIL modulation and enhancement from the presence of IGW's in a baroclinic life-cycle experiment, and proposed that this could persistently enhance/maintain the TIL via wave-mean flow interaction. This was confirmed in the study by Zhang et al. (2015), who showed that the strong wind shear found within the TIL lead to IGW breaking, downward heat flux and tropopause cooling (from a single US high-resolution radiosonde station).

The goal of our study is two-fold: 1) quantify how much of the TIL strength in the extratropics comes from its modulation by planetary to synoptic-scale waves, and 2) by subtracting the wave signal, to identify other processes that enhance the TIL and thereby make an observational confirmation of their relative contribution. Only modelling studies have looked at these processes thus far (reanalysis in the case of mSSW in Wargan and Coy (2016)), or their observation is very sparse (one single US high-resolution radiosonde station in the IGW study by Zhang et al. (2015)). Therefore it is of interest to put the roles of the different TIL enhancing processes, as enumerated above, into context by using high amounts of high-resolution global GPS-RO observations from the COSMIC mission (Anthes et al., 2008), which is the primary source of high-resolution observations of the temperature structure near the tropopause. It has to be pointed out that our focus is oriented on knowing the total signal of the extratropical (planetary to synoptic-scale) waves, rather than separating every possible wave type at each given time, which is not possible in practice given the highly variable background wind regimes in the extratropics (see section 2 for more details).

We extract the extratropical wave signal by wavenumber-frequency domain filtering of gridded GPS-RO data. Our method is similar to that of Pilch Kedzierski et al. (2016), who quantified the role of the different equatorial wave types in modulating and enhancing the tropical TIL. Compared to the equatorial wave filtering, the method in this study is adapted and simplified to account for the distinct wave spectrum and the highly varying wind regimes that are found in the extratropics. We explain how this is done, justifying the filter settings, in section 2; and we provide a proof of concept in section 3, showing that our method is successful in representing the extratropical waves and their TIL modulation. In section 4 we quantify the average signal of the extratropical waves as well as the remaining TIL with this signal removed, for all seasons in the mid- and high-latitudes of the Northern and Southern Hemispheres. We summarize and discuss our main findings in section 5.

2 Data and Methods

2.1 Datasets

We analyze GPS-RO temperature profiles measured by the COSMIC satellite mission (Anthes et al., 2008). The dataset has a high vertical resolution of 100m from the surface up to 40km altitude, similar to high-resolution radiosonde data. The effective physical resolution of GPS-RO retrievals is normally $\sim$1km, but improves in regions where the stratification of the atmosphere changes, such as the tropopause and the top of the boundary layer where high vertical resolution is most needed (Kursinski et al., 1997). GPS-RO has the advantages of global coverage, high sampling density of $\sim$2000 profiles/day, and weather-independence. Also, the accuracy of GPS-RO profiles is even higher than that of radiosondes (Anthes et al., 2008; WMO, 1996). With the temperature profiles, vertical profiles of static stability are calculated as the Brunt-Väisälä frequency squared (N^2 [s^{-2}]):

$$N^2 = (g/\Theta) \cdot (\partial\Theta/\partial z)$$

where g is the gravitational acceleration and Θ the potential temperature. The tropopause height (TP_z) was calculated using the WMO lapse-rate tropopause criterion (WMO, 1957). Profiles with unphysical temperatures or N^2 values (temperature <-150°C, >150°C or N^2 >$100\times10^{-4}s^{-2}$) or those where the tropopause was not found were excluded (< 1%).

We also use daily-mean vertical profiles of zonal winds from the ERA-Interim reanalysis (Dee et al., 2011), for the years 2007-2013. To extract the extratropical wave signal from the GPS-RO dataset, we first grid the profiles (see subsection 2.2) and then apply wavenumber-frequency domain filters which require data on a regular longitude-time spacing (see subsection 2.3).

2.2 Gridding of GPS-RO profiles

The COSMIC GPS-RO temperature profiles at certain latitude bands are gridded daily, between 2007-2013, on a regular longitude grid with a 10° separation. The latitude bands chosen for this study are 40°N and 40°S to represent the mid-latitudes, and 80°N and 80°S for polar latitudes. These latitude bands were selected because they show the seasonal cycle of the tropopause and TIL best for mid and high latitudes. Throughout sections 4 and 5, results for the latitudes 40° and 80° will be disclosed for both Hemispheres. The same analyses were performed for the latitude bands in between, 50°-60°-70°, which have an intermediate behavior in each case.

At each grid point, the profiles of that day within +-5° latitude and +-5° longitude are selected to calculate a tropopause-based weighted average temperature profile and the corresponding N^2 vertical profile:

$$T_{grid}(\lambda, Z_{TP}, t) = \sum\nolimits_i w_i T_i(\lambda, Z_{TP}, t) / \sum\nolimits_i w_i$$

$$N^2_{grid}(\lambda, Z_{TP}, t) = \sum\nolimits_i w_i N^2_i(\lambda, Z_{TP}, t) / \sum\nolimits_i w_i$$

where λ is longitude, Z_{TP} is the height relative to the tropopause and t is time. The weight w_i is an exponentially-folding function that depends on the distance of the GPS-RO profile from the grid center, taking longitude, latitude and time (distance from 12UTC):

$w_i = exp(-[(D_x/5)^2 + (D_y/5)^2 + (D_t/12)^2])$, where D are the distances in °longitude (x subscript), °latitude (y) and hours (t). The maximum distance allowed from the grid point in each dimension is: 5° longitude, 5° latitude, and 12 hours from 12UTC, respectively.

The gridded tropopause height (λ,t) is calculated with the same weighting of all profiles' tropopauses. The gridded temperature and N^2 profiles are shifted, as the last step, from the tropopause-based vertical scale onto a ground-based vertical scale from 5km to 35km altitude, obtaining a longitude-height array for each day of 2007-2013.

Most often 2-3 profiles are selected for averaging at a grid point with these settings, although one GPS-RO profile is sufficient to estimate a grid point. However, in 14.8% of the cases the algorithm does not find any profile. To fill in the gaps, the longitude range to select the profiles is incremented to +-10° instead of +-5°, and the latitude range is also incremented to +-7.5° instead of +-5°, which then leaves a 1.8% of empty grid-points. For this minority, profiles are selected within +-1day and +-15° longitude (and same latitude settings). In all cases the weighting function remains the same. The remaining data gaps (0.06%) are filled by averaging neighbouring grid points (+-1 longitude grids, then +-1 day grids). These exceptions are for a very small portion of the gridded data, and therefore do not affect the retrieved wave signatures after filtering (the percentages showed in this paragraph are for the Northern Hemisphere, and they are similar in the SH).

This gridding method is very similar to the one used by Pilch Kedzierski et al. (2016) in the equator, developed after Randel and Wu (2005). The higher GPS-RO density in the extratropics allowed for a narrower latitude range to select profiles around a latitude band in order to minimize meridional smoothing of the extratropical TIL properties. The lower bottom of the vertical scale is set to 5km to account for the lower extratropical tropopause heights compared to the equator.

Once gridded, for each latitude band, we end up with a daily longitude-time array of temperature and N^2 for each level between 5-35km with 100m vertical spacing. With a daily temporal resolution, this dataset resolves waves with periods of 2 days or longer, or frequencies of 0.5 cycles per day (cpd) or lower, which is enough to capture all the planetary and synoptic-scale extratropical waves. Note that the inertial frequency in the extratropics ranges from ~1.3cpd at 40° latitude to 2cpd at the poles, so inertia-gravity waves (IGW), with frequencies between the inertial and the much higher buoyancy frequency, cannot be resolved with these settings (Andrews et al., 1987). However, by extracting the combined planetary and synoptic-scale wave signal and substracting it later, we can indirectly infer how important is the role of IGWs or other processes in enhancing the extratropical TIL.

2.3 Wavenumber-Frequency Domain Filtering

With the longitude-height-time array of gridded temperature and N^2 profiles obtained in the previous subsection 2.2, we make use of the freely available 'kf-filter' NCL function (Schreck, 2009) to filter in the wavenumber-frequency domain. For each vertical level (from 5km to 35km height with 100m vertical spacing), we retrieve a longitude-time array which is detrended, tapered in time and space-time bandpass filtered with a two-dimensional Fast Fourier Transform. This methodology is analogous to that of Pilch Kedzierski et al. (2016), who filtered gridded equatorial GPS-RO data in certain regions of the wavenumber-frequency domain, following the dispersion curves of the different equatorial wave types which have clear spectral signatures in those wavenumber-frequency domains (Wheeler and Kiladis, 1999). In the remaining of this section we will explain how the filter bounds in the wavenumber-frequency domain were chosen in this study to adapt the method of Pilch Kedzierski et al. (2016) to the extratropics.

The extratropical wave modes differ greatly from those at the equator: they are not equatorially trapped and can propagate in any direction, the Coriolis parameter has to be taken into account, and the zonal wind regimes in the extratropics are much more variable than the equatorial ones. At sub-seasonal time-scales, the Northern Annular Mode (NAM) can alter the strength of the prevailing westerlies in the extratropical troposphere and lowermost stratosphere; there is a strong seasonal cycle in the stratosphere with very strong westerlies (several tens of m/s) within the winter polar vortex, changing to easterlies (-10 to -20 m/s) in summer; and the polar vortex is disrupted very quickly during major sudden stratospheric warmings (mSSW). These modes of variability of the zonal winds in the extratropics have higher amplitude and frequency than any wind regime shifts found at the equator, which has a relatively weak seasonal cycle, and the quasi-biennial oscillation (QBO) in the stratosphere still has less amplitude and frequency compared to the polar winter vortex - summer anticyclone. Background winds affect the propagation of waves, by doppler-shifting their dispersion relations or even precluding their propagation, therefore it is of special importance to take them into account in the extratropics.

We make a comparison of the dispersion curves of the extratropical Rossby wave under different background zonal wind regimes in Figure 1. The Rossby wave dispersion relation is defined as the most common form of large-scale wave disturbance found in the extratropics: a planetary wave forced from the troposphere, and propagating vertically and zonally in a quasi-geostrophic flow.

Assuming N^2 and background mean zonal winds (Ū) to be constant, and no meridional propagation for simplicity, the following dispersion relation can be obtained (following Andrews et al. (1987)):

$$w = s\bar{U} - s\beta[s^2 + f^2/gh]^{-1}$$

where *w* is the frequency, *s* is the zonal wavenumber, *f* the Coriolis parameter, β its meridional derivative at a certain latitude (the Beta-plane approximation), *g* the gravity acceleration and *h* the equivalent depth. Since we assume no meridional propagation for simplicity, the meridional wavenumber is set to zero so it is absent in this formula (compared to Andrews et al. (1987)). The term (sŪ) accounts for the doppler-shifting of the dispersion relation by the background zonal winds; and the (f^2 /gh) term is an approximation to account for the vertical propagation of the wave.

In Figure 1, we show how the dispersion curve of a Rossby wave changes depending on its equivalent depth (different line types), and the background zonal mean winds (zero winds black, blue for easterlies, red for westerlies, see specific arrows outside the diagram). Note that each dispersion curve is not valid for the entire year for the Rossby wave. For example, a Rossby wave in winter would propagate following the red (10m/s) dispersion relation in the lowermost stratosphere (i.e. the bottom of the polar vortex); at higher levels (the core of the polar vortex) stronger westerlies are found and the same Rossby wave would propagate following the red (40m/s) curve. At some point in spring and autumn, the black curve (Ū = 0 m/s) is theoretically valid, and so is the blue curve (-10m/s) in summer, with easterlies throughout the stratosphere.

The dispersion relations in Fig. 1 show the difficulty of defining a wave type in the extratropics: the dispersion curve for a given wave type (idealized Rossby wave in this case) can be in basically every possible place within the wavenumber-frequency domain, depending on the background winds. Therefore, it is impossible to define one filter to extract Rossby waves that is valid for the entire time period (2007-2013) and that could be used at all levels between 5 and 35km altitude.

We overcome this difficulty by simplifying the method of Pilch Kedzierski et al. (2016). Instead of defining certain dispersion curves, we use wide boxes in the wavenumber-frequency domain, only differentiating eastward-westward propagating oscillations with respect to the ground and their periods (faster 2-4 day waves; slower 4-25 day waves; and 30-96 day or quasi-stationary waves), which are displayed as the six grey boxes in Fig. 1. We also define a seventh filter for wavenumber zero (s = 0, brown box in the middle of the diagram in Fig. 1) for completeness. This way, the Rossby waves will be captured by one or another filter, independently of the background zonal winds.

With this method we prioritize knowing the total effect of planetary and synoptic-scale extratropical waves on the TIL, at the cost of not differentiating baroclinic, barotropic, standing, travelling (etcetera) wave modes. We find this to be a fair compromise, since our study targets TIL modulation and enhancement by extratropical waves (successfully, see sections 3, 4 and 5), and not to disclose particular properties of these waves.

If waves are present, their filtered signal is outstanding compared to the (unavoidable to filter) background noise, which appears as a continuum of low-amplitude fluctuations (Wheeler and Kiladis, 1999), and the instantaneous modulation of the tropopause and the TIL by these waves shall be captured since these oscillations are resolved by the gridded dataset (see subsection 2.2).

As mentioned above, the extratropical wave anomalies are filtered from a longitude-time array: each vertical level of the gridded GPS-RO profiles is filtered independently, and then stored together in a longitude-height-time array of wave anomalies. Therefore, for a given latitude band, we end up with arrays of gridded GPS-RO profiles (temperature and N^2), and the corresponding anomalies (also of temperature and N^2) from the seven wave filter bounds defined in Fig. 1, all gridded with 10° longitude, 100m height and 1-day spacing.

When one specific day is selected from these arrays, a longitude-height snapshot of the wave anomalies is obtained. Extratropical waves have vertical tilts in their temperature structures, and if the anomalies are large, they can effectively modulate tropopause height. As shown in Figure 2, the tropopause height, usually the coldest point in the uppermost troposphere, would vary zonally as a consequence of the idealized wave anomaly structure. A tropopause-based mean of these anomalies would yield a dipole of cold anomalies centered at the tropopause, warm anomalies above, and a net TIL enhancement just from the presence of the wave in the tropopause region. Note that the ground-based zonal average temperature profile and the zonal mean tropopause height would remain the same despite the presence of wave anomalies in Fig. 2: only the tropopause-based zonal mean profile is affected.

We expect that our filtered wave anomalies will modulate the tropopause in a similar fashion as sketched in Fig. 2 for temperature. Once a wave is away from the tropopause region or dissipated, no filtered signal shall affect the TIL, therefore permanent effects from wave-mean flow interaction (wave dissipation or breaking) are not quantified by our method.

Next in section 3, we show examples of the filtered signals and the tropopause adjustment to the extratropical waves, in order to proof the validity of our method to study the extratropical TIL wave modulation.

3 Proof of Concept

Figure 3 shows snapshots of the longitude-height N^2 anomalies (colors) filtered in the wavenumber-frequency domains defined in Fig. 1 (see previous subsection 2.3), together with the tropopause height (black line), for the 50°N latitude band. Each snapshot is selected for a different winter date, in order to portray cases when there is a clear modulation of the tropopause's zonal structures from the extratropical wave anomalies. We do not include the s=0 filter since it lacks zonal structures by definition. In Fig. 3 the eastward and westward propagation refers to the movement of the wave relative to the ground as defined in subsection 2.3.

In Fig. 3 there are several analogies to the tropopause and TIL modulation by equatorial waves described in the study by Pilch Kedzierski et al. (2016). In our extratropical case, we also show tropopause modulation by the wave anomalies when their amplitude is large, with predominant positive N^2 anomalies above the tropopause, and negative N^2 anomalies below, which correspond to the temperature anomalies that modulate tropopause height as sketched in Fig. 2. The modulation by extratropical waves is especially clear in Fig. 3c for eastward-propagating waves with periods of 4-25 days: strong positive N^2 anomalies are detected right above the tropopause between -180°E and -25°E, while negative N^2 are located below the tropopause between 25°E and 180°E. Similarly, in Fig. 3d (westward-propagating 4-to-25-day waves) tropopause height follows the positive N^2 anomalies between -75°E and 180°E. Sometimes positive N^2 anomalies can be located below the tropopause and viceversa, as in the cases shown in Fig. 3 a, b, e and f; but the zonal mean is still dominated by positive N^2 anomalies right above the tropopause. Note that the different wave types in Fig. 3 can be present at the same time, so some tropopause zonal structures in the snapshots can be the result of modulation by another wave type.

It can also be observed in all cases in Fig. 3 that there is a relative maximum of wave activity around the tropopause regardless of the amount of wave activity in the stratosphere, in line with the findings of Pilch Kedzierski et al. (2016) who reported wave amplification near the tropopause for every equatorial wave type.

The westward tilt of the Rossby waves can be discernible in many cases (Fig. 3 a-d) throughout the stratosphere: most clearly in the intermediate periods of 4-25 days which are the most common for travelling Rossby waves, but also visible sometimes in the 30-96 day periods, indicating the presence of quasi-stationary Rossby waves. This is a good indicator that these waves are properly captured by our filters, which are used at each vertical level independently: the vertical structure of the waves is obtained without filtering in the vertical direction. Note that in Fig. 3, planetary and synoptic-scale waves are all superimposed, so the overall appearance is increasingly patchy when short and fast waves are present, which is why Fig. 3 e and f show these structures the most.

The wavenumber-frequency domain filtering method used for extratropical waves (see subsection 2.3 and Fig. 1), although simplified compared to Pilch Kedzierski et al. (2016) and unable to differentiate particular wave types, is able to capture the overall planetary and synoptic-scale extratropical wave signal and how it modulates the tropopause and the TIL as shown in Fig. 3.

The examples shown in Fig. 3 are for the 50°N latitude band in winter, but similar conclusions can be drawn from any extratropical latitude or season. The tropopause-based, seasonal mean of the extratropical wave signal shall show an overall TIL enhancement, and this will be quantified next in section 4 for mid and high latitudes, winter and summer, Northern and Southern Hemisphere.

4 Wave Modulation of the Extratropical Tropopause Inversion Layer

Figure 3 in section 3 showed the tropopause adjustment to the horizontal and vertical structure of the filtered extratropical wave anomalies, with positive N^2 anomalies generally placed above the tropopause, and negative N^2 anomalies below. Therefore, a tropopause-based average of the wave signals should give a net TIL enhancement. We perform the same analysis with the filtered temperature anomalies, which we expect to show a net tropopause cooling and a warm anomaly aloft (the dipole needed to enhance N^2 right above the tropopause). When using the terms cooling/warming, we refer to the net effect of extratropical waves on the tropopause-based zonal mean profile, since certain levels are cooler/warmer in the seasonal mean profile due to these waves.

Also, by substracting the extratropical wave signal from the gridded GPS-RO data, it is possible to show the remaining TIL that is caused by mechanisms other than the extratropical wave modulation. We will present the daily evolution of the vertical tropopause-based N^2 profile, comparing the observed N^2 vertical structure to the one without the extratropical wave signal, which should show a weaker TIL.

Note that the wavenumber-frequency domain filters are not able to extract the wave anomalies at the beginning and end of the 2007-2013 time-period of our study. The highest period filtered is 96 days (see section 2, Fig. 1), therefore data from the first 100 days of 2007 and the last 100 days of 2013 are not used for any figures of this section, in order to make sure that there is no signal missing.

Throughout this section, we will present the two kinds of analysis explained in the previous paragraphs: seasonal, tropopause-based averages of the extratropical wave temperature and N^2 signals; and the time evolution of observed N^2 zonal-mean profiles, with and without the daily extratropical wave signal. Both analyses will be presented for mid-latitudes (40°N, subsection 4.1) and polar latitudes (80°N, subsection 4.2), first in the Northern Hemisphere, and then the exact same methodology is applied to the same latitude bands in the Southern Hemisphere (80°S in subsection 4.3; 40°S in Appendix A).

4.1 Northern Hemisphere Mid-latitudes

Figure 4 shows the seasonally averaged signature of the different extratropical wave types (defined in subsection 2.3, figure 1) at 40°N, as their mean anomaly in the tropopause-based zonal-mean vertical profiles of temperature (left column) and N^2 (right column). All the defined extratropical wave types show a cooling effect maximizing at the tropopause (Fig. 4 a and c), and a N^2 increase directly above the tropopause (Fig. 4 b and d). This is also in line with the findings by Pilch Kedzierski et al. (2016), who found the same effect of all equatorial wave types on the tropical TIL, only varying in the amplitude of the mean wave signature. The mean wave signatures in Figure 4 show that extratropical waves enhance the TIL in a very similar manner by tropopause adjustment to the wave signal and the resulting cooling of the tropopause (and warming above to a lesser degree).

In Fig. 4 (a-d), the strongest signal belongs to eastward-propagating waves with periods of 4 to 25 days (red lines), in both winter (top row) and summer (bottom row). Baroclinic Rossby waves, the most common wave type occuring at mid-latitudes (with prevailing westerlies during all year at near-tropopause level, therefore their eastward propagation respect to the ground), fit within this broadly defined wavenumber-frequency domain. This also explains why the extratropical wave signal is stronger in winter at mid-latitudes, since the mid-latitude jet strength and the baroclinic wave activity both peak there during winter. We also note that quasi-stationary waves (periods of 30-96 days, black and dashed magenta lines) and the s=0 wave type (grey line) play a minor role in enhancing the TIL.

The total extratropical wave signal (Fig. 4 e and f) at 40°N is a tropopause cooling of $\sim$3.5K and a TIL enhancement of $\sim 1.6\times10^{-4}s^{-2}$ in winter (red line). In summer (black line) the modulation is weaker: tropopause cooling of $\sim$2.3K and $\sim 1.1\times10^{-4}s^{-2}$ of TIL enhancement. The total extratropical wave signature in NH mid-latitude summer has a very similar magnitude compared to the equatorial wave signal obtained by Pilch Kedzierski et al. (2016).

Figure 5a shows the daily evolution of the tropopause-based N^2 profile (2007-2013) at 40°N. In Fig. 5a the TIL is clearly discernible in winter with higher N^2 values right above the tropopause, ranging between $5.5\times10^{-4}s^{-2}$ (orange) and $6.5\times10^{-4}s^{-2}$ (red). Above the TIL in winter, the lowermost stratosphere has a relative minimum in N^2 of $\sim 3.5\times10^{-4}s^{-2}$ centered at 15km height, and levels higher than 18km have N^2 values of $\sim 5\times10^{-4}s^{-2}$. In summer months the tropopause is higher, and although the TIL and the stratospheric N^2 values are separated by a weak relative N^2 minimum (white, blueish sometimes), both layers have N^2 values of 5-5.5 $\times10^{-4}s^{-2}$ (yellow, orange sometimes). Fig. 5a agrees with previous climatologies of the mid-latitude N^2 vertical structure (e.g. Birner (2006); Grise et al. (2010)), while also showing its short-term variability without time-averages.

Fig. 5b shows the same N^2 profile evolution, but with the daily extratropical wave signal subtracted, therefore displaying the tropopause-based N^2 structures without the instantaneous modulation by planetary to synoptic-scale extratropical waves. Therefore, any TIL observed in Fig. 5b should be caused by other processes. It can be observed that the TIL in Fig. 5b is almost completely gone: N^2 right above the tropopause is always lower than the stratospheric values above 18km. However, in winter and spring a very weak relative maximum of N^2 can be observed above the tropopause (4-4.5 $\times10^{-4}s^{-2}$, white and light-blue colors compared to the N^2 minimum of $3.5\times10^{-4}s^{-2}$ at 15km height), occasionally reaching N^2 values close to $5\times10^{-4}s^{-2}$ (sparse light-yellow spots) in late winter and spring. In summer, there is no relative N^2 maximum above the tropopause at all in Fig. 5b.

The conclusion that Fig. 5b gives is that most of the mid-latitude TIL is explained by the instantaneous modulation by planetary to synoptic-scale extratropical waves. Other possible sources of TIL enhancement in the extratropics like IGW modulation, wave-mean flow interactions of any wave type, residual circulation or radiative effects; all together they play a minor role in forming the zonal-mean TIL structure. The TIL enhancement by IGWs (Zhang et al., 2015) can be of importance locally in space and time, but its contribution to the zonal-mean TIL (even if it explained all the structures in Fig. 5b) would be less than the effect of the filtered planetary and synoptic-scale extratropical waves.

Separating the different extratropical wave types and their contribution to TIL enhancement is beyond the scope of this study, but of interest for future research. Two questions arise from our results:

1) Which wave type is dominant? Figs. 3 and 4 point towards the baroclinic Rossby wave, the most common and strongest wave type occurring in the extratropics, and we find the biggest signals in the broad wavenumber-frequency domain that would include this wave type, but this still needs robust confirmation. Our current method would need significant refinement to separate the baroclinic Rossby wave from other wave modes present in the extratropics.

2) Which is the process that leads to the amplification of extratropical waves next to the tropopause level? This is visible in Fig. 3 for all wave types defined in subsection 2.3, and analogous to the near-tropopause amplification of all equatorial wave types in the tropics observed by Pilch Kedzierski et al. (2016). It would be of high interest to know whether this amplification follows Linear Wave Theory (Andrews et al., 1987) or not.

The conclusions from this subsection for 40°N also apply to the Southern Hemisphere. The equivalent analyses for 40°S can be found in Appendix A.

4.2 Northern Hemisphere Polar latitudes

We proceed to apply the same analysis from the previous subsection 4.1 to polar latitudes. Figure 6 shows the seasonal average signature of the different extratropical wave types (defined in subsection 2.3, Fig. 1) at 80°N, as their mean anomaly in the tropopause-based zonal-mean vertical profiles of temperature (left column) and N^2 (right column). As in mid-latitudes (subsection 4.1), all the defined extratropical wave types show a cooling effect maximized at the tropopause (Fig. 6 a and c), and a N^2 increase right above the tropopause (Fig. 6 b and d). However, at polar latitudes the seasonality of the extratropical wave forcing is inverted compared to mid-latitudes. The total wave signatures in Fig. 6 e and f are weaker in winter (red line), with a tropopause cooling of ~2.6K and a TIL enhancement of $\sim 1.1 \times 10^{-4} s^{-2}$, similar to that found in mid-latitude summer. In summer (black line), there is a total tropopause cooling of ~3.9K and a TIL enhancement of $\sim 1.9 \times 10^{-4} s^{-2}$, similar to that found in mid-latitude winter.

Note that in Fig. 6 (a-d) the eastward-propagating 4-25 day band (red line) is no longer as dominant as in Fig. 4. This can be explained by the fact that zonal mean westerly winds are weaker at polar latitudes, therefore the wave spectrum does not get Doppler-shifted as much as at mid-latitudes, and more waves are observed to be westward-propagating with respect to the ground. As to why the extratropical wave signature is stronger in polar summer, as opposed to mid-latitudes (stronger in winter), we explain the inverted seasonalities by the position of the jet stream and the baroclinic wave activity, which migrate polewards in summer while being at the mid-latitudes in winter. However, it is still surprising that the total extratropical wave signature on the TIL region is of the same magnitude at mid-latitudes and polar latitudes, despite the opposed seasonal cycles as explained above. Since the meridional temperature gradients and the jet stream are weaker in summer, one would expect the extratropical wave signature on the TIL to follow this tendency. It is possible that extratropical waves at polar regions get amplified near the tropopause and reach the same amplitude as at mid-latitudes (at opposing seasons), but as noted in subsection 4.1 this amplifying mechanism near the tropopause needs further research.

Figure 7a shows the daily evolution of the tropopause-based N^2 profile (2007-2013) at 80°N. There is a distinct TIL throughout the year, with N^2 values right above the tropopause of $\sim 5\times 10^{-4}s^{-2}$ in winter (white to yellow colors) and between 7-8 $\times 10^{-4}s^{-2}$ in summer (brown and black sometimes). Stratospheric N^2 values are around $4\times 10^{-4}s^{-2}$ (dark and light blue) at levels within 14-26km height, with increasing N^2 at higher levels. The N^2 structures showed in Fig. 7a (as in Fig. 5a) agree with previous climatologies of the high-latitudes N^2 vertical structure (Birner, 2006; Grise et al., 2010), and the daily temporal resolution shows the high variability associated with sudden stratospheric warmings (SSWs) in the stratosphere. Higher N^2 values in the stratosphere are observed during SSWs, with positive N^2 anomalies propagating downward and reaching the TIL region. The SSWs signals at particular events will be discussed next, since they will be easier to differentiate once the extratropical wave signal is removed in Fig. 7b.

Fig. 7b shows the N^2 profile evolution without the daily extratropical wave signal, displaying the tropopause-based N^2 structures caused by other processes. The TIL in Fig. 7b is significantly weakened without the extratropical wave modulation: in winter it almost disappears, but in summer the TIL is still distinct (5-6 $\times 10^{-4}s^{-2}$, yellow and orange) from the background stratospheric N^2 structure (blue). The extratropical wave modulation explains an important part of the TIL's N^2 structure in polar latitudes (a similar amount of N^2 enhancement as in mid-latitudes, with inverted seasonality, Fig. 6), but other sources of TIL enhancement are also present as it can be observed in Fig. 7b (unlike in Fig. 5b for mid-latitudes, where almost no TIL is visible without the extratropical wave signal). Most notably, the removal of the extratropical wave signal makes the time evolution of the vertical N^2 structures in Fig. 7b much smoother compared to Fig. 7a, and allows a clearer appearance of the downward-propagating signal from SSWs and how it affects the tropopause region. In Fig. 7b, major SSW events are marked with black arrows (2008, 2009, 2010, 2013), and one minor event is marked with a grey arrow in 2012. The major SSW event from February 2007 is not marked, since the first 100 days of 2007 are cut off for the analyses in this section.

During major SSWs, the residual circulation is accelerated, and the convergence of its vertical component ($\overline{w*}$) forces a positive temperature anomaly that propagates downward into the lowermost stratosphere (Andrews et al., 1987). In the study by Wargan and Coy (2016) it was shown that $\overline{w*}$ convergence is associated with a downward-propagating positive N^2 anomaly as well, that enhances the TIL once the SSW signal reaches the tropopause region. Wargan and Coy (2016) calculated a $\sim$1.5$\times$10$^{-4}s^{-2}$ increase of the zonal-mean N^2 maximum above the tropopause due to the 2009 major SSW, and slightly lower N^2 increases in other SSW cases. In Fig. 7b, it can be observed that N^2 right above the tropopause in early 2009 increases from $\sim$4$\times$10$^{-4}s^{-2}$ (blue) before the SSW, up to $\sim$5.5$\times$10$^{-4}s^{-2}$ (orange) after the SSW. Also, a positive N^2 anomaly from the 2009 major SSW can be seen in Fig. 7b propagating downwards throughout the stratosphere (white and yellow instead of blue), and the TIL enhancement coincides with the time when this downward-propagating anomaly reaches the tropopause region, as well as a marked decrease in the zonal-mean tropopause height. This perfectly fits the findings of Wargan and Coy (2016). In Fig. 7b the same can be observed in the major SSW cases of 2008, 2010 and 2013, although the N^2 anomalies are slightly lower than in 2009 which was an exceptionally strong event.

Interestingly, in Fig. 7b we observe the downward-propagating positive N^2 anomaly, TIL enhancement and tropopause lowering in a minor SSW in early 2012, and also during the final warmings of 2011 and 2013. The coherency in time of these signals, and their similarity to the cases described by Wargan and Coy (2016) suggests that they are also driven by an acceleration of the residual circulation (increased $\overline{w*}$ convergence) from the disturbed polar vortex. The 2013 case is quite particular: once the major SSW is finished, the polar vortex recovers, the TIL is no longer enhanced and the tropopause slowly increases its height; but then there is a strong final warming event, another downward-propagating N^2 signal, immediate TIL enhancement and a slight lowering of the zonal-mean tropopause. After this, the zonal-mean tropopause gets steadily higher into the summer. In the final warming of 2011 there is an abrupt transition from a strong polar vortex to anticyclonic circulation, and the downward-propagating N^2 signal, TIL enhancement and abrupt zonal-mean tropopause lowering is also visible in Fig. 7b. In the case of the minor SSW of 2012, the TIL enhancement and zonal-mean tropopause lowering are also in clear coincidence with the disrupted westerlies.

Figure 7b shows evidence, directly from observations, that the TIL is enhanced due to major SSWs, and also from other polar vortex disturbances: minor SSWs and abrupt final stratospheric warmings. The similarity of our results with Wargan and Coy (2016), who studied major SSWs, in terms of the time evolution of the N^2 signal, TIL enhancement and tropopause height; suggests that accelerated residual circulation (increased $\overline{w*}$ convergence) is the main contributor to TIL enhancement during all kinds of polar vortex disturbances, not only major SSWs. This would need confirmation with a more detailed study of (non-major) polar vortex disturbances and the associated residual circulation variability.

Fig. 6f showed TIL enhancement of $\sim$1.1$\times$10$^{-4}s^{-2}$ by extratropical wave modulation in polar winter. In Fig. 7b, we show that polar vortex disturbances in general can enhance the TIL in winter (major and minor SSWs) and spring (final warmings) with a similar magnitude. The remaining TIL in polar summer in Fig. 7b (∼$5.5\times10^{-4}s^{-2}$, orange) is not explained by extratropical wave modulation, nor by residual circulation. The only other mechanism restricted to polar summer that could enhance the TIL is water vapor radiative cooling of the tropopause (Randel and Wu, 2010; Miyazaki et al., 2010b), but this would also require an additional study to be confirmed.

We also note that the meridional advection of the SSW signals in the lowermost stratosphere could be the cause of the very weak hints of the mid-latitude TIL without the extratropical wave signal found in Fig. 4b, that mainly appears in late winter and spring and was strongest in 2009, 2010 and 2013, coinciding with major SSW events.

Given that the polar vortex behavior affects the TIL more clearly at polar latitudes, we expect more differences between the NH and the SH, since the polar vortex in the SH is much less disturbed than in the NH, and the only mSSW observed in the SH happened in 2002.

4.3 Southern Hemisphere Polar latitudes

Figure 8 is the Southern Hemisphere (SH) equivalent of Fig. 6. The total extratropical wave signal at 80°S (Fig. 8 e and f) is a tropopause cooling of ∼1.4K and a TIL enhancement of ∼$0.9\times10^{-4}s^{-2}$ in winter (compared to ∼$1.4\times10^{-4}s^{-2}$ TIL enhancement in the NH in Fig. 6). In summer there is a tropopause cooling of ∼2.5K and ∼$1.3\times10^{-4}s^{-2}$ of TIL enhancement (∼$1.9\times10^{-4}s^{-2}$ in the NH, Fig. 6). The extratropical wave signatures in Fig. 8 show the same seasonality as in Fig. 6, with stronger (weaker) signals in summer (winter) months, but the overall magnitude of the extratropical wave forcing at polar latitudes is lower in the SH than in the NH.

The lower extratropical wave activity and the smaller mean signal at the tropopause near the South pole is explained by the isolation of the SH polar latitudes: no land-sea contrast or high mountain ranges in the meridional direction (less wave sources), and a stronger and more stable polar vortex that does not allow waves to propagate so deep into high latitudes, as opposed to the NH. The behavior of the extratropical wave forcing in SH polar latitudes (Fig. 8) is similar to the NH (Fig. 6) but weaker. In subsection 4.2 (NH polar latitudes) it was shown that, after subtracting the extratropical wave signal, the TIL enhancement from SSWs (major or minor) and final warmings could be seen clearly. In the 2007-2013 period, no SSW occurred in the SH, so we only aim to see what is the effect of final warmings.

Figure 9a shows the daily evolution of the tropopause-based N^2 profile at 80°S. There is a clear TIL during summer months, with N^2 values of ∼$7\times10^{-4}s^{-2}$ (brown) right above the tropopause. In winter, the TIL is harder to discern, but a weak maximum of ∼$4.5\times10^{-4}s^{-2}$ (white, light yellow) is present above the winter tropopause. The TIL near the South Pole in winter is known to be very weak or absent (Tomikawa et al., 2009; Pilch Kedzierski et al., 2015). Compared to the NH, the SH polar vortex is stronger, less disturbed during winter, and has a longer lifetime: it breaks later in spring, almost into the summer.

Note that in Fig. 9 the tropopause is higher during winter (unlike in Figs. 5 and 7). This seasonal cycle in the high-latitude SH tropopause agrees with previous climatologies from GPS-RO (Son et al., 2011), and is attributed to the very cold and stable polar vortex (Zängl and Hoinka, 2001) and the seasonal cycle in the strength of the Brewer-Dobson circulation (Yulaeva et al., 1994). Also, there is some indeterminacy in the exact height of the thermal tropopause, since the background temperature lapse-rate in SH high-latitudes is close to the WMO lapse-rate tropopause criterion (WMO, 1957) of 2K/km for several kilometers in the upper troposphere during winter. We discuss the downward-propagating signal of the SH polar vortex breakup next.

Fig. 9b shows the N^2 profile evolution without the daily extratropical wave signal, displaying the tropopause-based N^2 structures caused by other processes. In summer, the TIL is significantly weaker but clearly present in Fig. 9b. In winter, the TIL cannot be detected without the extratropical wave signal, and the vertical N^2 structures are smoother and enable a clearer view of the downward-propagating N^2 signal from the SH vortex breakup in late spring. Once the signal reaches the tropopause region, there is an abrupt increase in N^2 right above the tropopause, from values of $\sim$4$\times$10$^{-4}s^{-2}$ (blue) to $\sim$5.5$\times$10$^{-4}s^{-2}$ (yellow-orange), in line with the findings of Wargan and Coy (2016) and our previous subsection 4.2 and Fig. 7b. Even a slight and short-lived relative minimum in tropopause height can be observed with the arrival of the vortex breakup signal. Note that in Fig. 9b, no TIL is discernible until the downward-propagating N^2 signal from the SH polar vortex breakup arrives. For example, the contrast between the summers of 2011/12 and 2012/13: in the first summer, the signal reaches the tropopause region right at the beginning of 2012, and the TIL is observed since; whereas in the next summer the polar vortex breaks up early, and the strong TIL is observed more than a month before the beginning of 2013.

Later in the summer, the TIL generally reaches N^2 values of $\sim$6$\times$10$^{-4}s^{-2}$ every year in Fig. 9b. As in the previous subsection 4.2, we also suggest that the remaining TIL in Fig. 9b in summer is enhanced by water vapor radiative effects which would need further study.

5 Concluding Remarks

Our study used a simplified method to extract the total extratropical (planetary to synoptic-scale) wave signal from gridded COSMIC GPS-RO profiles. By tropopause-based zonal averaging of these signals at certain latitude bands, we were able to quantify how much of the extratropical TIL at mid- and polar latitudes is explained by the instantaneous modulation of the tropopause region by the planetary and synoptic-scale waves. By subtracting the extratropical wave signal, we show how much of the TIL is left due to other processes.

We found that extratropical wave modulation explains almost all of the observed TIL strength at mid-latitudes in both hemispheres (Figs. 5 and A2). Therefore we conclude that wave-mean flow interactions, inertia-gravity waves or the residual circulation are of minor importance as TIL enhancing mechanisms there.

At polar regions, extratropical wave modulation is dominant as well in explaining the TIL strength, but there is also a clear signal from SSWs, major and minor, in the Northern Hemisphere, and final warmings in both hemispheres (Figs. 7 and 9). The similarity in the time evolution of all signals from the disturbed polar vortexes in both hemispheres suggests that they are forced by the same mechanism: $\overline{w*}$ convergence from accelerated residual circulation as in the major SSW study by Wargan and Coy (2016).

Also, part of the polar summer TIL strength is not explained by extratropical wave modulation nor by residual circulation. We suggest that the only other mechanism restricted to polar summer that could enhance the TIL is water vapor radiative cooling of the tropopause (Randel and Wu, 2010; Miyazaki et al., 2010b), which requires additional study to be confirmed.

Two questions arise from our results: 1) what are the separate roles of the different planetary and synoptic-scale wave types within the total extratropical wave modulation of the TIL, and 2) which is the mechanism for wave amplification near the tropopause as seen in Fig. 3.

Our study, working only with COSMIC GPS-RO observations, has identified and quantified an important mechanism for extratropical TIL enhancement: extratropical wave modulation, which is dominant in the extratropics and especially at mid-latitudes. We suggest that the remaining TIL in polar regions can be explained by accelerated residual circulation from polar vortex disturbances (given the similarities of our results with Wargan and Coy (2016)) and water vapor radiative effects in polar summer, although these would need to be confirmed by additional studies.

Appendix A: Wave modulation of the TIL in SH Mid-latitudes

Figure A1 is the Southern Hemisphere equivalent of Fig. 4 (which was for 40°N). The signatures of the different extratropical waves in Fig. A1 lead to the same conclusions for the SH mid-latitudes: all defined waves show a net cooling effect maximizing at the tropopause, a slight warming above it, and a net N^2 increase directly above the tropopause (Fig. A1 a-d). The strongest wave signal belongs to eastward-propagating waves with periods of 4 to 25 days (red lines), which is even more dominant in Fig. A1 than in Fig. 4 due to the stronger westerlies found in the SH. Quasi-stationary waves (periods of 30-96 days, black and dashed magenta lines) and the s=0 wave type (grey line) play a minor role in enhancing the TIL in both hemispheres.

The total extratropical wave signal (Fig. A1 e-f) at 40°S is a $\sim$3.6K colder tropopause in the seasonal zonal-mean, tropopause-based profile, and a TIL enhancement of $\sim 1.7\times10^{-4}s^{-2}$ in winter (red line). In summer (black line) the modulation is weaker: tropopause cooling of $\sim$3.0K and $\sim 1.4\times10^{-4}s^{-2}$ of TIL enhancement. The total extratropical wave signature in SH mid-latitudes has the same winter-summer seasonality as the NH, and a slightly higher magnitude throughout the year.

Figure A2 compares the daily evolution of the zonal-mean, tropopause-based vertical N^2 profile at 40°S, with (Fig. A2a) and without the extratropical wave signal (Fig. A2b). Fig. A2 is the SH equivalent of Fig. 5, and also leads to the same conclusions: there is a distinct TIL in Fig. A2a throughout the year ($\sim 6 \times 10^{-4} s^{-2}$, orange-red in winter; $\sim 5 \times 10^{-4} s^{-2}$ yellow in summer), which is almost completely gone once the daily extratropical wave signal is subtracted. The weak hints of a TIL seen in Fig. 5b are even weaker in Fig. A2b, suggesting that other TIL enhancing processes play an even humbler role in the SH. We conclude from Fig. A2 that the TIL modulation by planetary and synoptic-scale waves explains most of the TIL strength in the tropopause-based N^2 structure at mid-latitudes also in the SH.

The findings of subsection 4.1 (NH mid-latitudes, Figs. 4 and 5) also apply to the SH (Figs. A1 and A2) in a nearly-coincident way.

Acknowledgements. This study was completed within the Helmholtz-University Young Investigators Group NATHAN project, funded by the Helmholtz Association through the president's Initiative and Networking Fund and the GEOMAR Helmholtz-Centre for Ocean Research in Kiel. We thank the ECMWF data server for the freely available ERA-Interim data; and UCAR for the COSMIC, satellite missions' temperature profiles. The assistance accessing different datasets and discussions with Sandro Lubis, Wuke Wang and Sebastian Wahl are also appreciated.

References

Andrews, D. G., Holton, J. R., and Leovy, C. B.: Middle atmosphere dynamics, International Geophysics Series, Vol. 40, Academic Press, 1987.

Anthes, R. A., Bernhardt, P. A., Chen, Y., Cucurull, L., Dymond, K. F., Ector, D., Healy, S. B., Ho, S.-P., Hunt, D. C., Kuo, Y.-H., Liu, H., Manning, K., McCormick, C., Meehan, T. K., Randel, W. J., Rocken, C., Schreiner, W. S., Sokolovskiy, S. V., Syndergaard, S., Thompson, D. C., Trenberth, K. E., Wee, T.-K., Yen, N. L., and Zeng, Z.: The COSMIC/FORMOSAT-3 Mission: Early Results, Bulletin of the American Meteorological Society, 89, 313, doi:10.1175/BAMS-89-3-313, 2008.

Birner, T.: Fine-scale structure of the extratropical tropopause region, Journal of Geophysical Research (Atmospheres), 111, D04104, doi:10.1029/2005JD006301, 2006.

Birner, T.: Residual Circulation and Tropopause Structure, Journal of Atmospheric Sciences, 67, 2582–2600, doi:10.1175/2010JAS3287.1, 2010.

Birner, T., Dörnbrack, A., and Schumann, U.: How sharp is the tropopause at midlatitudes?, Geophysical Research Letters, 29, 1700, doi:10.1029/2002GL015142, 2002.

Dee, D. P., Uppala, S. M., Simmons, A. J., Berrisford, P., Poli, P., Kobayashi, S., Andrae, U., Balmaseda, M. A., Balsamo, G., Bauer, P., Bechtold, P., Beljaars, A. C. M., van de Berg, L., Bidlot, J., Bormann, N., Delsol, C., Dragani, R., Fuentes, M., Geer, A. J., Haimberger, L., Healy, S. B., Hersbach, H., Hólm, E. V., Isaksen, L., Kållberg, P., Köhler, M., Matricardi, M., McNally, A. P., Monge-Sanz, B. M., Morcrette, J.-J., Park, B.-K., Peubey, C., de Rosnay, P., Tavolato, C., Thépaut, J.-N., and Vitart, F.: The ERA-Interim reanalysis: configuration and performance of the data assimilation system, Quarterly Journal of the Royal Meteorological Society, 137, 553–597, doi:10.1002/qj.828, 2011.

Erler, A. R. and Wirth, V.: The Static Stability of the Tropopause Region in Adiabatic Baroclinic Life Cycle Experiments, Journal of Atmospheric Sciences, 68, 1178–1193, doi:10.1175/2010JAS3694.1, 2011.

Gettelman, A., Hoor, P., Pan, L. L., Randel, W. J., Hegglin, M. I., and Birner, T.: The Extratropical Upper Troposphere and Lower Stratosphere, Reviews of Geophysics, 49, RG3003, doi:10.1029/2011RG000355, 2011.

Grise, K. M., Thompson, D. W. J., and Birner, T.: A Global Survey of Static Stability in the Stratosphere and Upper Troposphere, Journal of Climate, 23, 2275–2292, doi:10.1175/2009JCLI3369.1, 2010.

Hegglin, M. I., Boone, C. D., Manney, G. L., and Walker, K. A.: A global view of the extratropical tropopause transition layer from Atmospheric Chemistry Experiment Fourier Transform Spectrometer O_3, H_2O, and CO, Journal of Geophysical Research (Atmospheres), 114, D00B11, doi:10.1029/2008JD009984, 2009.

Kunkel, D., Hoor, P., and Wirth, V.: Can inertia-gravity waves persistently alter the tropopause inversion layer?, Geophysical Research Letters, 41, 7822–7829, doi:10.1002/2014GL061970, 2014.

Kunz, A., Konopka, P., Müller, R., Pan, L. L., Schiller, C., and Rohrer, F.: High static stability in the mixing layer above the extratropical tropopause, Journal of Geophysical Research (Atmospheres), 114, D16305, doi:10.1029/2009JD011840, 2009.

Kursinski, E. R., Hajj, G. A., Schofield, J. T., Linfield, R. P., and Hardy, K. R.: Observing Earth's atmosphere with radio occultation measurements using the Global Positioning System, Journal of Geophysical Research: Atmospheres, 102, 23 429–23 465, doi:10.1029/97JD01569, 1997.

Miyazaki, K., Watanabe, S., Kawatani, Y., Sato, K., Tomikawa, Y., and Takahashi, M.: Transport and Mixing in the Extratropical Tropopause Region in a High-Vertical-Resolution GCM. Part II: Relative Importance of Large-Scale and Small-Scale Dynamics, Journal of Atmospheric Sciences, 67, 1315–1336, doi:10.1175/2009JAS3334.1, 2010a.

Miyazaki, K., Watanabe, S., Kawatani, Y., Tomikawa, Y., Takahashi, M., and Sato, K.: Transport and Mixing in the Extratropical Tropopause Region in a High-Vertical-Resolution GCM. Part I: Potential Vorticity and Heat Budget Analysis, Journal of Atmospheric Sciences, 67, 1293–1314, doi:10.1175/2009JAS3221.1, 2010b.

Pilch Kedzierski, R., Matthes, K., and Bumke, K.: Synoptic-scale behavior of the extratropical tropopause inversion layer, Geophysical Research Letters, 42, 10,018–10,026, doi:10.1002/2015GL066409, 2015GL066409, 2015.

Pilch Kedzierski, R., Matthes, K., and Bumke, K.: The Tropical Tropopause Inversion Layer, Atmospheric Chemistry and Physics Discussions, pp. 1–26, doi:10.5194/acp-2016-178, 2016.

Randel, W. J. and Wu, F.: Kelvin wave variability near the equatorial tropopause observed in GPS radio occultation measurements, Journal of Geophysical Research (Atmospheres), 110, D03102, doi:10.1029/2004JD005006, 2005.

Randel, W. J. and Wu, F.: The Polar Summer Tropopause Inversion Layer, Journal of Atmospheric Sciences, 67, 2572–2581, doi:10.1175/2010JAS3430.1, 2010.

Randel, W. J., Wu, F., and Forster, P.: The Extratropical Tropopause Inversion Layer: Global Observations with GPS Data, and a Radiative Forcing Mechanism, Journal of Atmospheric Sciences, 64, 4489, doi:10.1175/2007JAS2412.1, 2007.

Schmidt, T., Cammas, J.-P., Smit, H. G. J., Heise, S., Wickert, J., and Haser, A.: Observational characteristics of the tropopause inversion layer derived from CHAMP/GRACE radio occultations and MOZAIC aircraft data, Journal of Geophysical Research (Atmospheres), 115, D24304, doi:10.1029/2010JD014284, 2010.

Schreck, C.: Extract equatorial waves by filtering in the Wheeler-Kiladis wavenumber-frequency domain., https://www.ncl.ucar.edu/Document/Functions/User_contributed/kf_filter.shtml, 2009.

Sjoberg, J. P. and Birner, T.: Stratospheric Wave-Mean Flow Feedbacks and Sudden Stratospheric Warmings in a Simple Model Forced by Upward Wave Activity Flux, Journal of Atmospheric Sciences, 71, 4055–4071, doi:10.1175/JAS-D-14-0113.1, 2014.

Son, S.-W. and Polvani, L. M.: Dynamical formation of an extra-tropical tropopause inversion layer in a relatively simple general circulation model, Geophysical Research Letters, 34, L17806, doi:10.1029/2007GL030564, 2007.

Son, S.-W., Tandon, N. F., and Polvani, L. M.: The fine-scale structure of the global tropopause derived from COSMIC GPS radio occultation measurements, Journal of Geophysical Research (Atmospheres), 116, D20113, doi:10.1029/2011JD016030, 2011.

Tomikawa, Y., Nishimura, Y., and Yamanouchi, T.: Characteristics of Tropopause and Tropopause Inversion Layer in the Polar Region, SOLA, 5, 141–144, doi:10.2151/sola.2009-036, 2009.

Wargan, K. and Coy, L.: Strengthening of the Tropopause Inversion Layer during the 2009 Sudden Stratospheric Warming: A MERRA-2 Study, Journal of Atmospheric Sciences, 73, 1871–1887, doi:10.1175/JAS-D-15-0333.1, 2016.

Wheeler, M. and Kiladis, G. N.: Convectively Coupled Equatorial Waves: Analysis of Clouds and Temperature in the Wavenumber-Frequency Domain., Journal of Atmospheric Sciences, 56, 374–399, doi:10.1175/1520-0469(1999)056<0374:CCEWAO>2.0.CO;2, 1999.

Wirth, V.: Static Stability in the Extratropical Tropopause Region., Journal of Atmospheric Sciences, 60, 1395–1409, doi:10.1175/1520-0469(2003)060<1395:SSITET>2.0.CO;2, 2003.

Wirth, V.: A dynamical mechanism for tropopause sharpening, Meteorologische Zeitschrift, 13, 477–484, doi:10.1127/0941-2948/2004/0013-0477, 2004.

Wirth, V. and Szabo, T.: Sharpness of the extratropical tropopause in baroclinic life cycle experiments, Geophysical Research Letters, 34, 2809, doi:10.1029/2006GL028369, 2007.

WMO: Meteorology-A three-dimensional science, WMO Bull., 6, 134–138, 1957.

WMO: Guide to Meteorological Instruments and Methods of Observation, 6th ed. WMO No. 8, 1996.

Yulaeva, E., Holton, J. R., and Wallace, J. M.: On the Cause of the Annual Cycle in Tropical Lower-Stratospheric Temperatures., Journal of Atmospheric Sciences, 51, 169–174, doi:10.1175/1520-0469(1994)051<0169:OTCOTA>2.0.CO;2, 1994.

Zängl, G. and Hoinka, K. P.: The Tropopause in the Polar Regions., Journal of Climate, 14, 3117–3139, doi:10.1175/1520-0442(2001)014<3117:TTITPR>2.0.CO;2, 2001.

Zhang, Y., Zhang, S., Huang, C., Huang, K., Gong, Y., and Gan, Q.: The interaction between the tropopause inversion layer and the inertial gravity wave activities revealed by radiosonde observations at a midlatitude station, Journal of Geophysical Research: Atmospheres, 120, 8099–8111, doi:10.1002/2015JD023115, 2015.

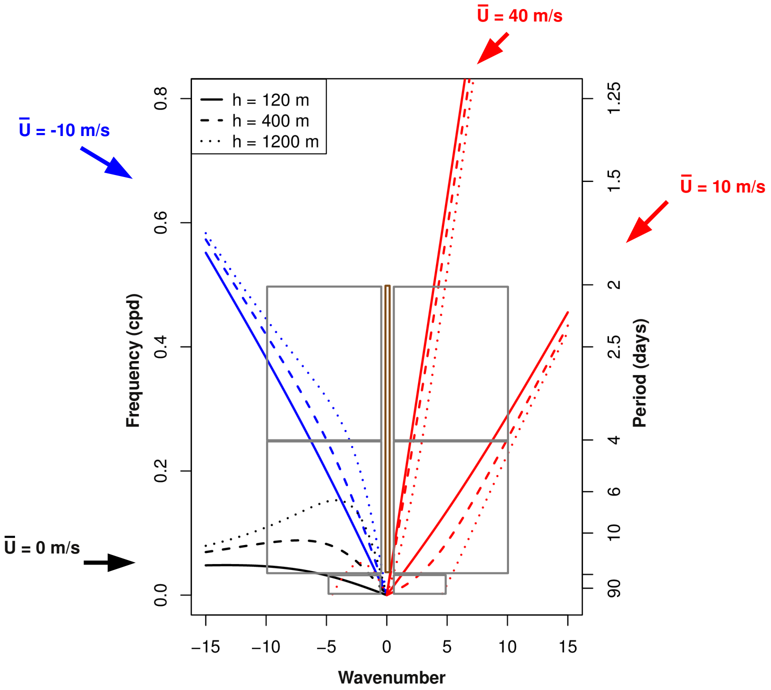

Figure 1. Dispersion curves for forced Planetary Waves at 50°N under different mean zonal wind regimes (line colors, winds specified outside the diagram), and differentiating equivalent depths (line type, top-left box). Filter bounds in the wavenumber-frequency domain are shown as grey boxes (brown for wavenumber zero).

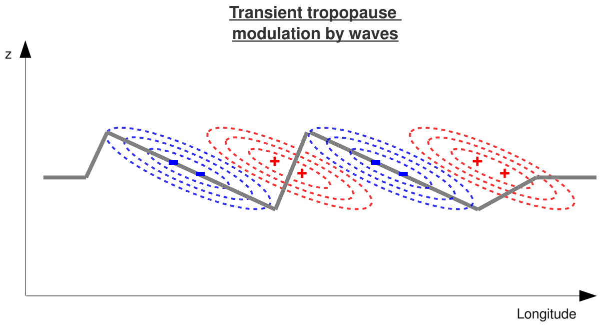

Figure 2. Schematic of transient tropopause modulation by an idealized wave with westward vertical tilt, as a snapshot of the wave's temperature anomalies (dashed contours: positive red, negative blue) and the undulating tropopause (thick and solid grey line).

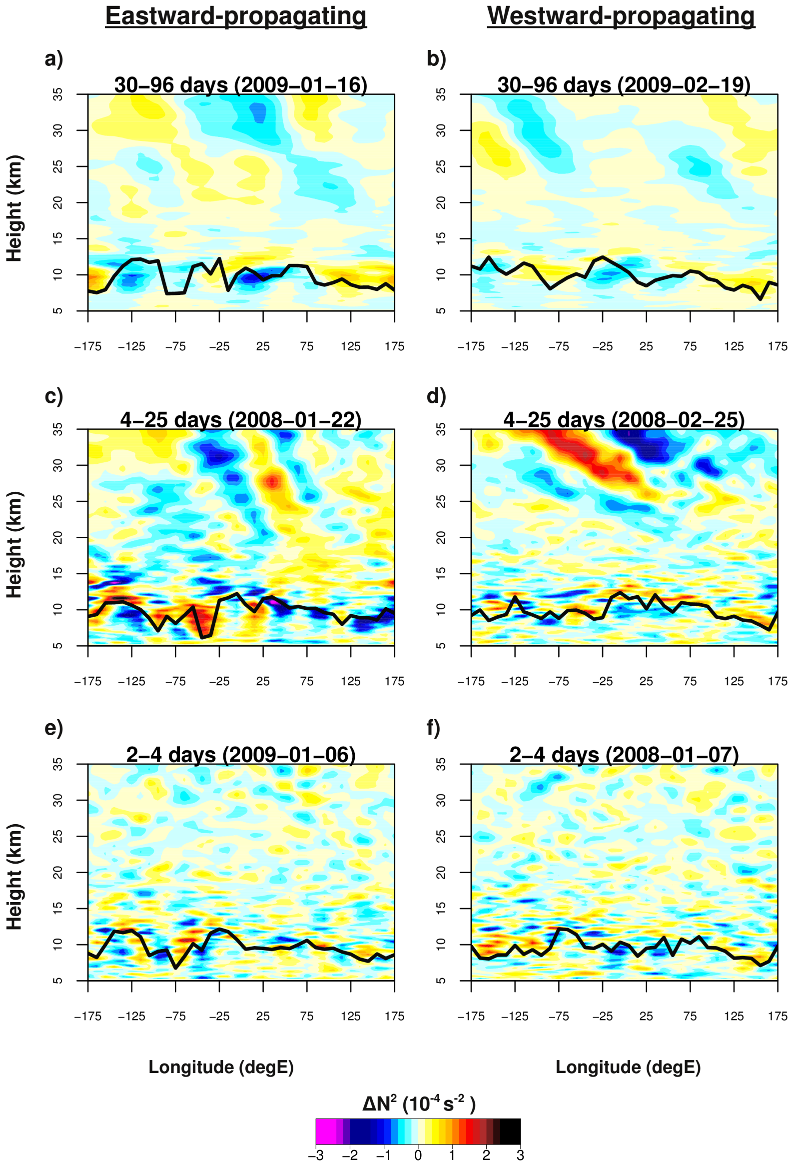

Figure 3. Longitude-height snapshots of the N^2 anomalies of the different wave types at certain dates, for the 50°N latitude band. Wave types correspond to the wavenumber-frequency domains defined in Fig. 1, except for wavenumber zero. Left column are eastward-propagating waves, right column are westward-propagating waves, and their periods are specified along with the date. The black line denotes the thermal tropopause.

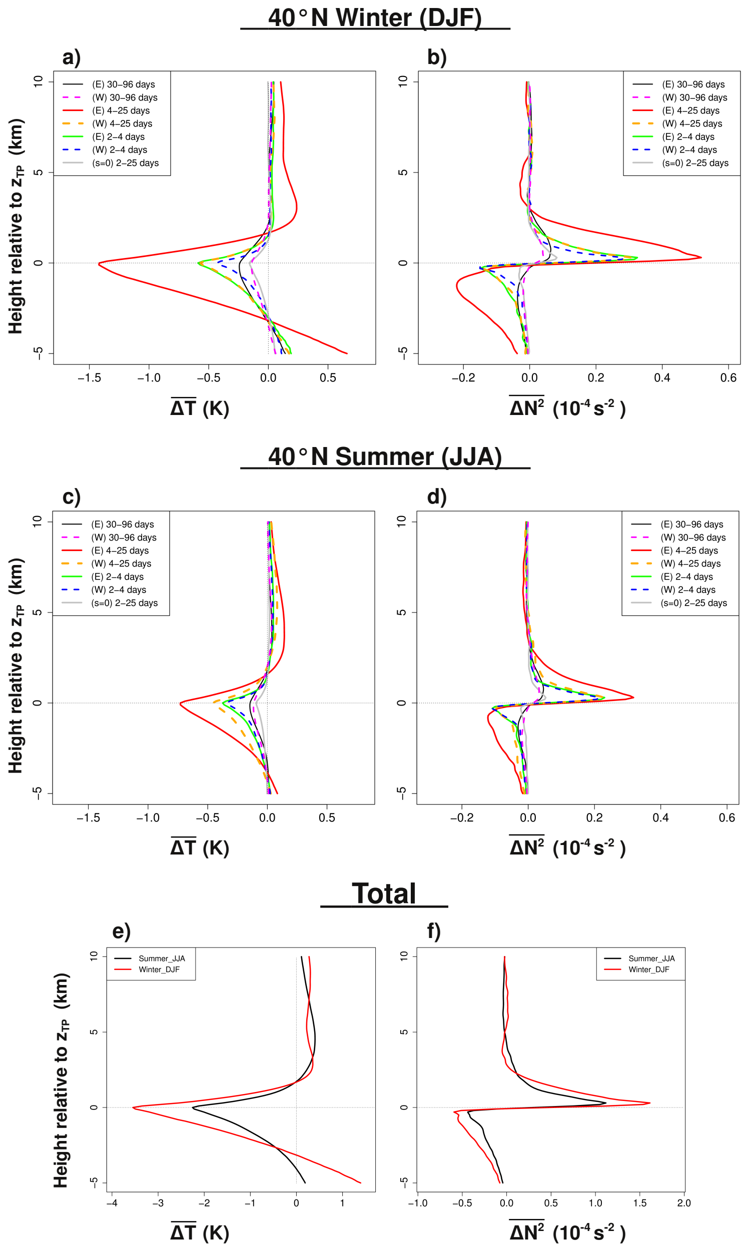

Figure 4. Average signature of the different wave types at 40°N, as the mean anomaly in the zonal-mean vertical profiles of temperature ($\overline{\Delta T}$, left column) and static stability ($\overline{\Delta N^2}$, right column). Top row (a and b) for winter (DJF), middle row (c and d) for summer (JJA). Bottom row (e and f) compares the total seasonal wave signatures.

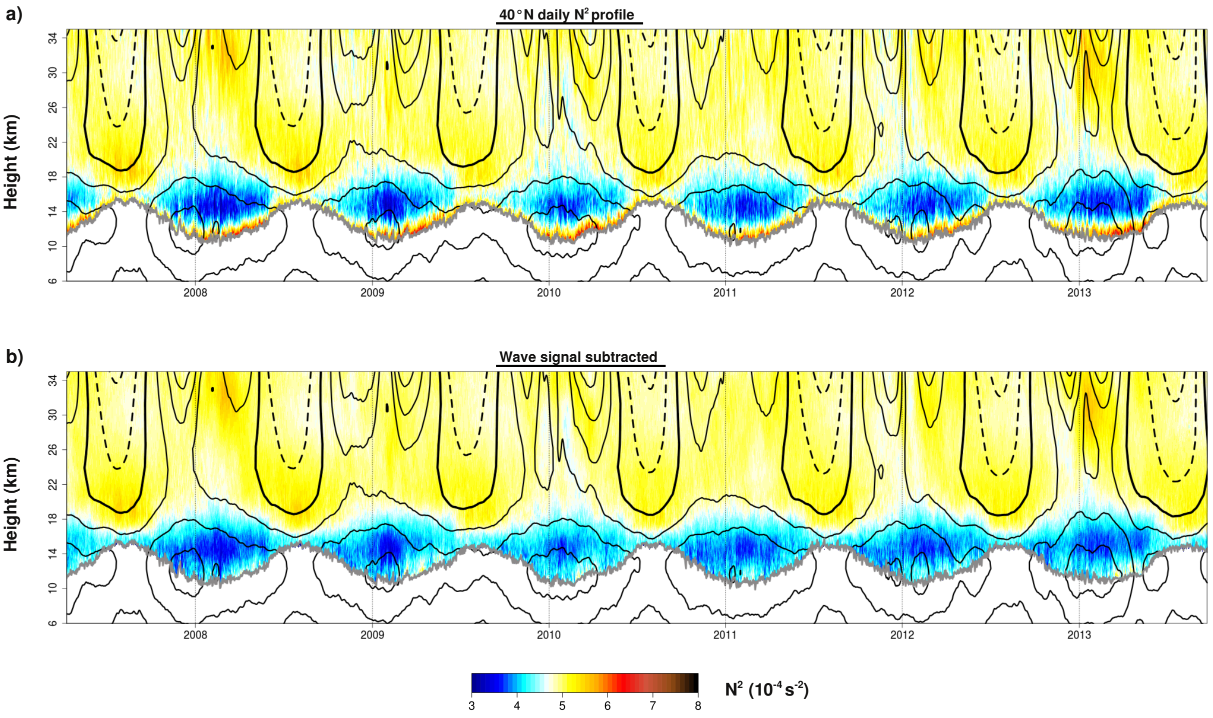

Figure 5. a) Daily evolution of the tropopause-based, 40°N zonal mean N^2 vertical profile between 2007-2013 (colors) from COSMIC GPS-RO profiles. The grey line denotes the tropopause height (TP_z). Thin black contours denote positive (westerly) mean zonal wind, with a thicker contour for the zero line, dashed contours for negative (easterly) winds, and a 10m/s separation. To improve visibility, the winds are displayed with a running mean of +-15 days. No running mean is applied to the N^2 vertical profile or TP_z in order to allow the subtraction of the extratropical wave signal. b) Same as in Fig. 5a, but the daily wave signal has been subtracted from the N^2 vertical profile.

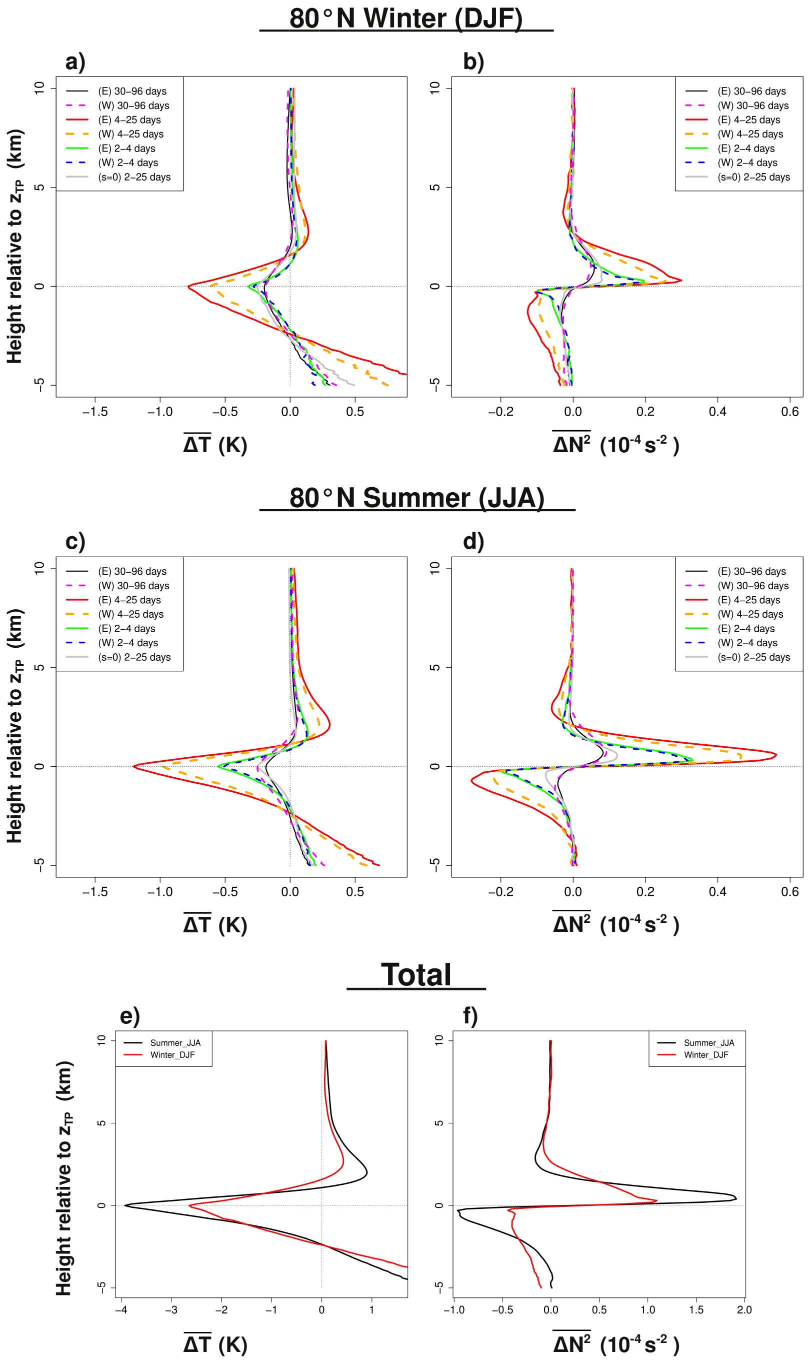

Figure 6. As in Fig. 4, but for 80°N.

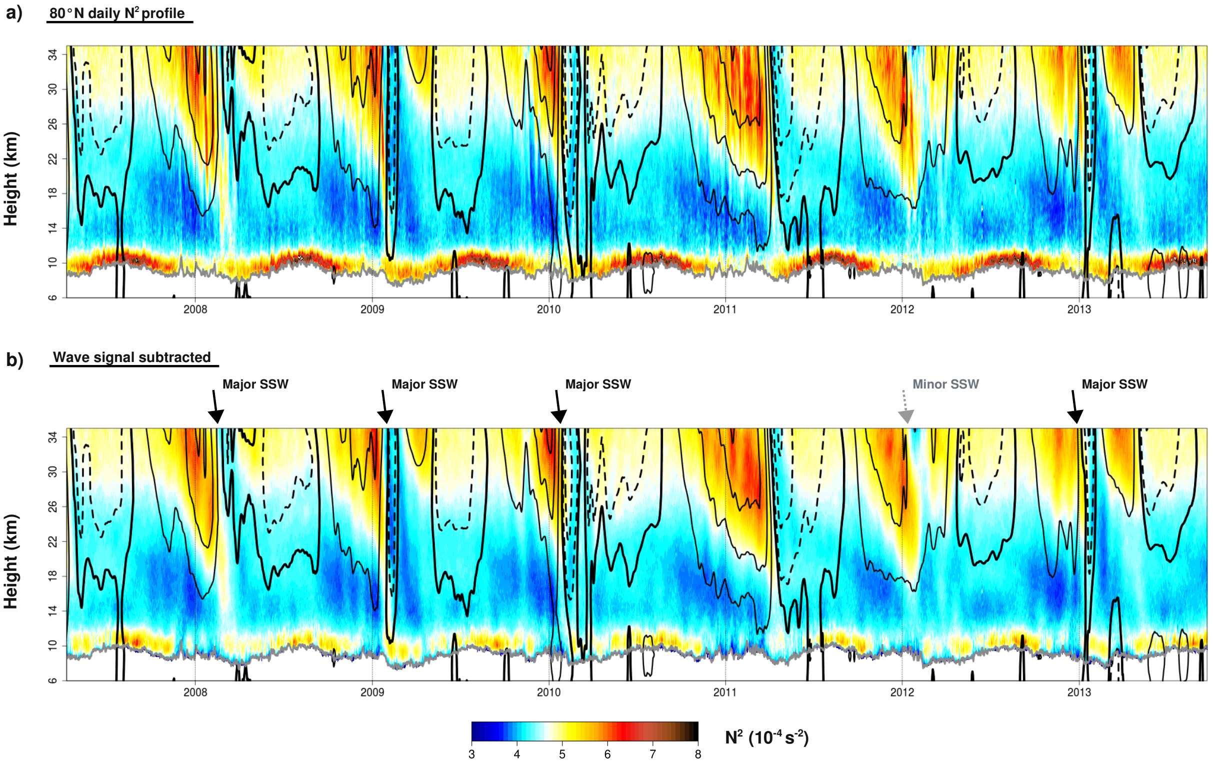

Figure 7. As in Fig. 5, but for 80°N. Major and minor SSWs are marked above Fig. 7b. First easterly wind contour (dashed line) at -3m/s for better visibility. The rest of wind contours are 10m/s intervals as in Fig. 5.

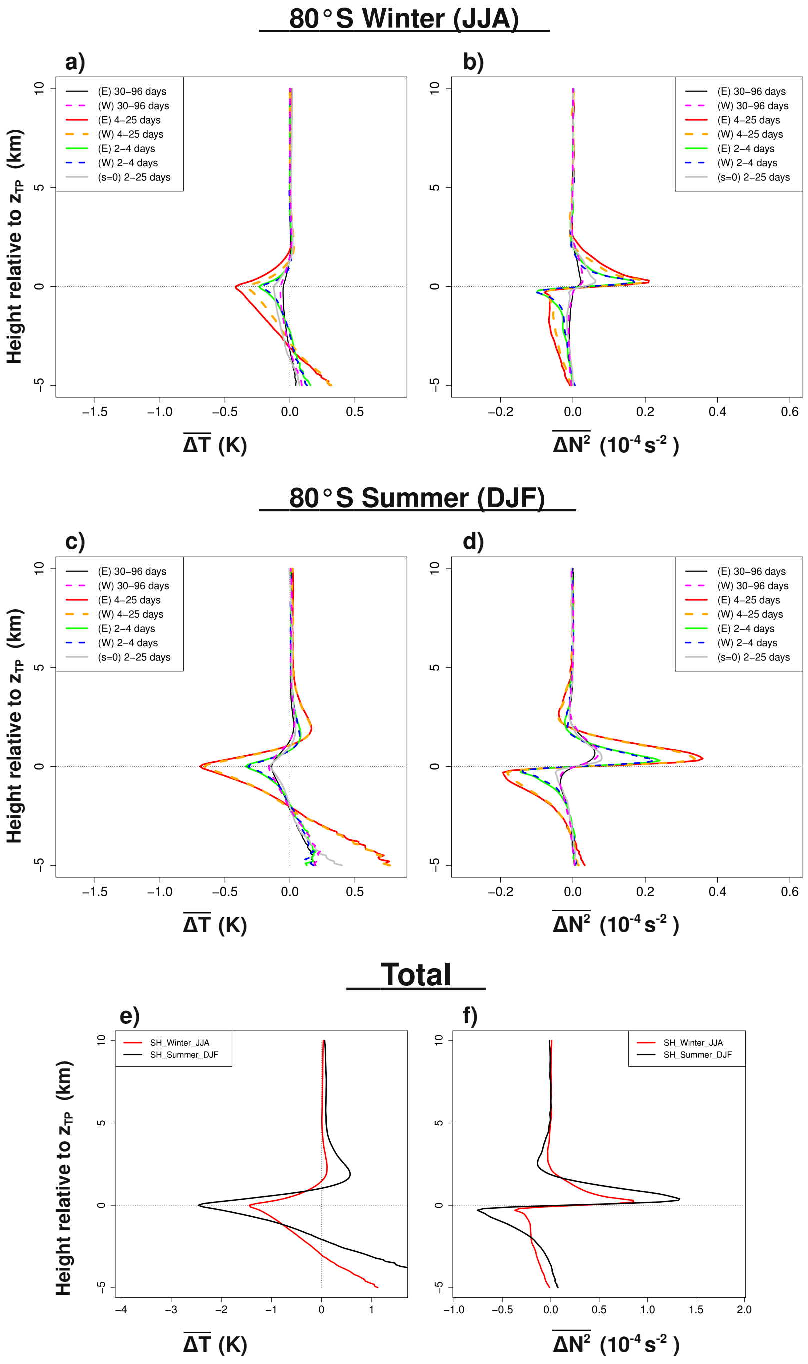

Figure 8. As in Figs. 4 and 6, but for 80°S.

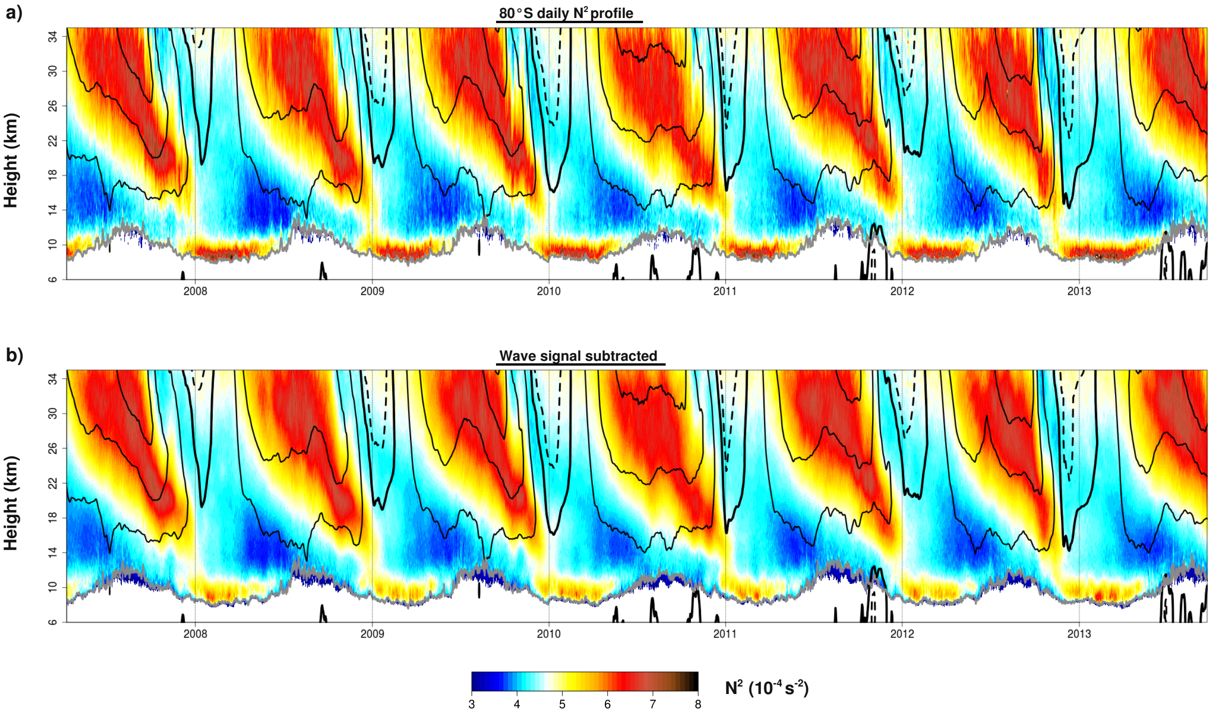

Figure 9. As in Fig. 5 and 7, but for 80°S. First easterly wind contour (dashed line) at -3m/s for better visibility. The rest of wind contours are 10m/s intervals as in Fig. 5.

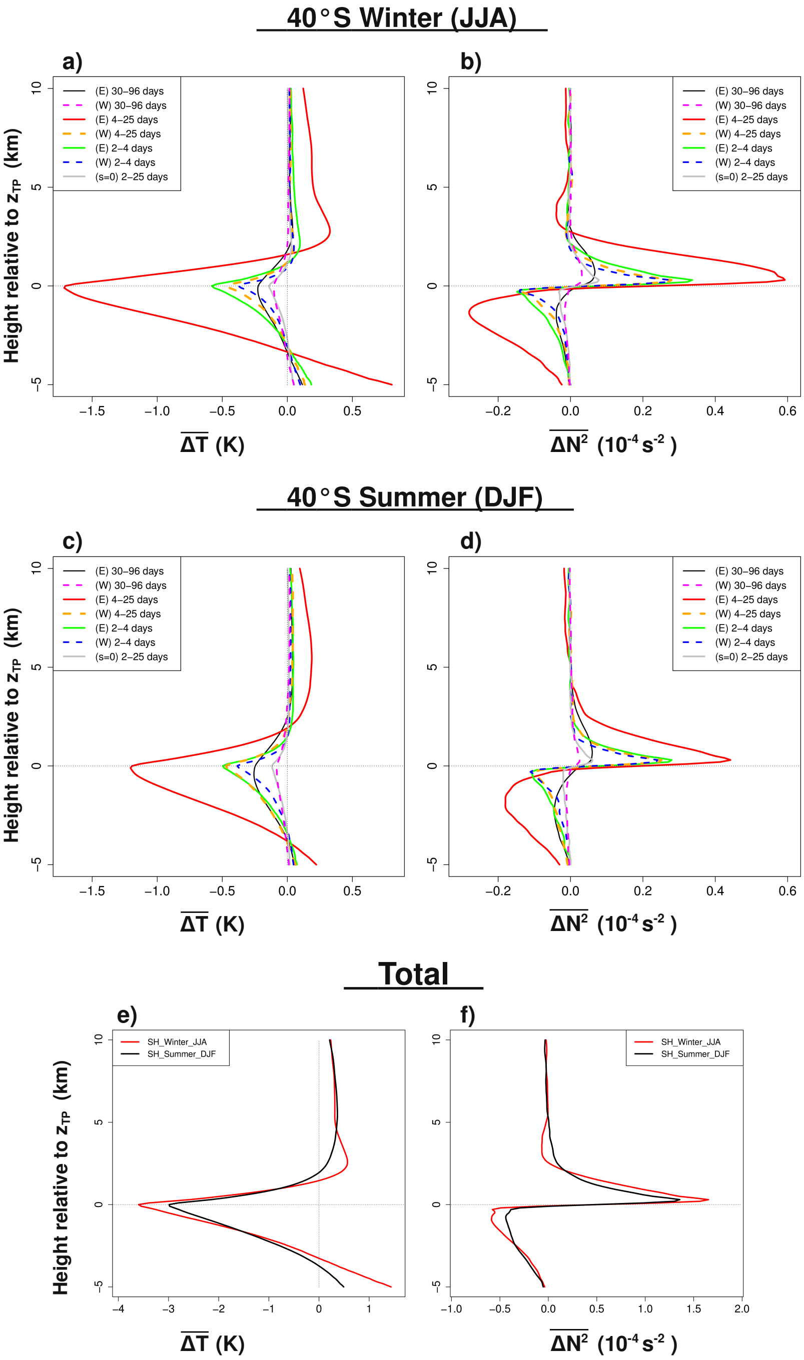

Figure A1. As in Figs. 4, 6 and 8, but for 40°S.

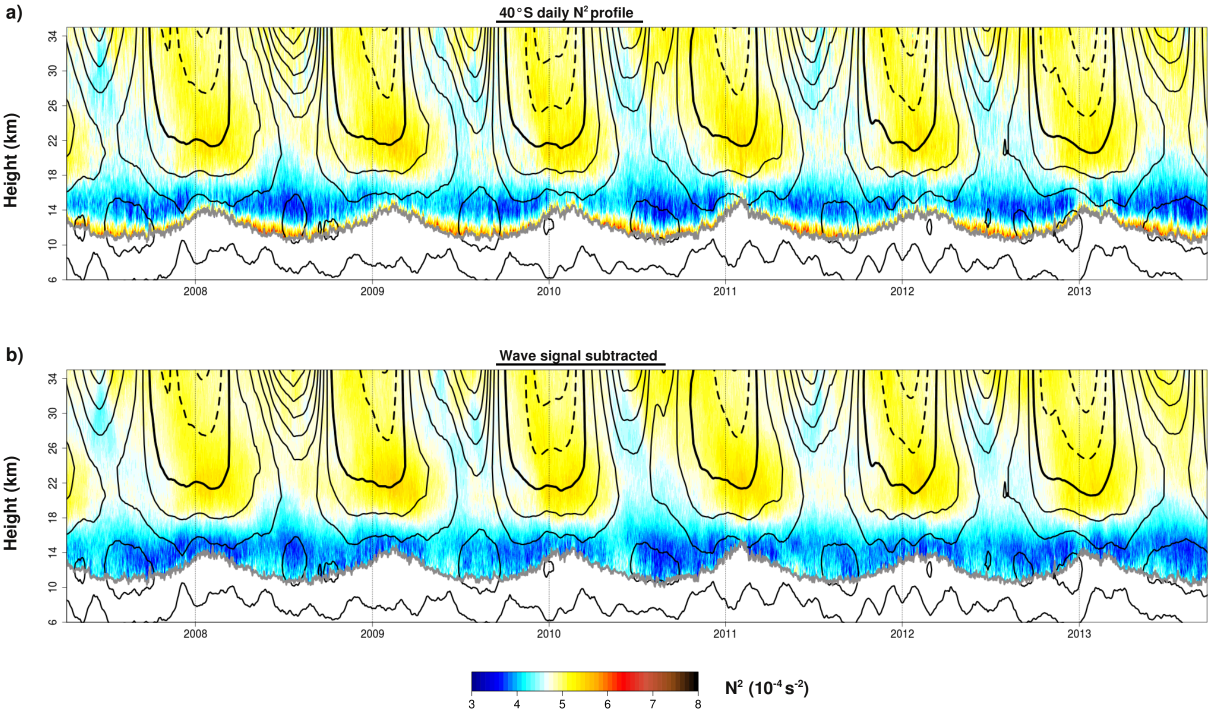

Figure A2. As in Fig. 5, but for 40°S.

5 Tropopause Sharpening by Data Assimilation

This chapter is a reprint of the article of the same name accepted for publication in *Geophysical Research Letters*. The hypothesis by *Birner et al.* [2006], that data assimilation smooths out the model's TIL, is tested by directly analyzing the assimilation increments from ERA-Interim reanalysis and the ECMWF operational forecast system. In the process, the representation of the TIL in the analyses of both systems is described. The calculations are done at the highest vertical resolution available, i.e. from the model hybrid levels instead of pressure levels.

Citation:

Pilch Kedzierski, R., L. Neef, and K. Matthes (2016c), Tropopause sharpening by data assimilation, *Geophysical Research Letters*, *43*, pp. 1-18, doi:10.1002/2016GL069936, (accepted / in press).

Author contributions to this publication:

- R. Pilch Kedzierski initiated the study, designed the method, did the analysis, produced all the figures and wrote the manuscript.

- L. Neef contributed with ideas and discussions on the analysis, and commented the manuscript.

- K. Matthes contributed with ideas and discussions on the analysis, and commented the manuscript.

Confidential manuscript submitted to *Geophysical Research Letters*

Tropopause Sharpening by Data Assimilation

R. Pilch Kedzierski[1*], **L. Neef**[1], **K. Matthes**[1,2]

[1]Marine Meteorology Department, GEOMAR Helmholtz Centre for Ocean Research Kiel, Kiel, Germany.
[2]Faculty of Mathematics and Natural Sciences, Christian-Albrechts-Universität zu Kiel, Kiel, Germany.

Key Points:

- Data Assimilation improves the TIL in modern systems.
- Direct analysis of 4D-Var increments.
- ERA-Interim and ECMWF operational forecast system compared to GPS-RO.

---

[*] Marine Meteorology Department, GEOMAR Helmholtz Centre for Ocean Research Kiel, Düsternbrooker Weg 20, D-24105 Kiel (Germany)

Corresponding author: Robin Pilch Kedzierski, `rpilch@geomar.de`

Abstract

Data assimilation was recently suggested to smooth out the sharp gradients that characterize the Tropopause Inversion Layer (TIL) in systems that did not assimilate TIL-resolving observations. We investigate whether this effect is present in the ERA-Interim reanalysis and the ECMWF operational forecast system (which assimilate high-resolution observations) by analyzing the 4D-Var increments and how the TIL is represented in their data assimilation systems. For comparison, we also diagnose the TIL from high-resolution GPS radio occultation temperature profiles from the COSMIC satellite mission, degraded to the same vertical resolution as ERA-Interim and ECMWF operational analyses. Our results show that more recent reanalysis and forecast systems improve the representation of the TIL, updating the earlier hypothesis. However, the TIL in ERA-Interim and ECMWF operational analyses is still weaker and further away from the tropopause than GPS-RO observations of the same vertical resolution.

1 Introduction

The Tropopause Inversion Layer (TIL) consists of a sharp temperature inversion and a corresponding maximum in static stability right above the thermal tropopause [*Birner et al.*, 2002], that is present globally [*Birner*, 2006; *Grise et al.*, 2010]. The high static stability values within the TIL can affect the dispersion relations of atmospheric Rossby or Inertia-Gravity waves [*Birner*, 2006; *Grise et al.*, 2010], and inhibit the cross-tropopause exchange of chemical compounds by preventing vertical motion, since stability correlates with trace-gas gradients [*Hegglin et al.*, 2009; *Kunz et al.*, 2009; *Schmidt et al.*, 2010].

The TIL is a fine-scale feature whose properties can only be captured by data of high vertical resolution ($\sim$100 m), i.e. GPS radio occultation (GPS-RO) by satellites, and high-resolution radiosonde measurements. Atmospheric models are very limited in this sense, generally having a vertical resolution near the tropopause of around 1 km. *Hegglin et al.* [2010] and *Gettelman et al.* [2010] compared the TIL in various models within the Chemistry Climate Model Validation project 2 (CCMVal2). They degraded the vertical resolution of GPS-RO observations to the models' standard pressure levels and found that, even after accounting for vertical resolution differences, the modelled TILs were always further away from the tropopause and generally weaker than the TIL retrieved from degraded observations.

Birner et al. [2006] investigated the TIL in two data assimilation systems, the NCEP/NCAR reanalysis [*Kalnay et al.*, 1996], and the Canadian Middle Atmosphere Model assimilating observations (CMAM+DA, *Polavarapu et al.* [2005]). The atmospheric models in both systems have a vertical resolution of roughly 1km near the tropopause, and both systems use three-dimensional variational (3D-Var) data assimilation. *Birner et al.* [2006] found that the TIL from the free-running CMAM was stronger than the TIL from CMAM with data assimilation and the NCAR reanalysis, and showed how data assimilation weakened the TIL in CMAM immediately after being switched on. Therefore *Birner et al.* [2006] suggested that data assimilation smooths out the sharp gradients that lead to the formation of the TIL. It has to be pointed out that neither of those systems assimilated GPS-RO data.

Recently, modern reanalyses have been used to study the TIL, as is the case in *Gettelman and Wang* [2015] who produced a set of TIL diagnostics from ERA-Interim [*Dee et al.*, 2011], and *Wargan and Coy* [2016] who showed TIL enhancement during a sudden stratospheric warming in MERRA-2 [*Molod et al.*, 2015]. The reanalyses used in these studies include innumerable improvements from those analyzed by *Birner et al.* [2006]: model resolution has increased, bias correction has become more sophisticated, as well as the parameterizations (clouds, convection, gravity waves, etc.), the data assimilation procedures have evolved (e.g. four-dimension variational data assimilation, 4D-Var [*Rabier et al.*, 2000], has been implemented in ERA-Interim), large amounts of high-resolution GPS-RO profiles (especially from the COSMIC satellite mission [*Anthes et al.*, 2008]) are assimilated, among many other improvements that result in a better representation of the atmosphere.

Our goal is to test whether the hypothesis of *Birner et al.* [2006], that data assimilation smoothes out the TIL, is still valid in newer systems. To achieve this, we will study the TIL and how it is affected by data assimilation in ERA-Interim and a more recent version of the ECMWF operational forecast model. The latter has greater horizontal and vertical resolution, and is used to test whether the effect of data assimilation is still the same despite the different versions of the assimilating model. Our results show TIL improvement by data assimilation with very similar structures in both systems. As discussed in the previous paragraph, there are innumerable differences between the assimilation systems in *Birner et al.* [2006] and modern ones, thus specifying which factors in particular are responsible for the better representation of the TIL is beyond the scope of our study and requires further research and experiments.

As a first step, we will show the TIL in the ERA-Interim reanalysis and the ECMWF operational analyses, comparing both to the TIL from GPS-RO observations degraded to the corresponding model levels. Secondly, we investigate the effect of data assimilation by analyzing the 4D-Var analysis increments, i.e. the difference in the model states before and after data assimilation, in terms of static stability. This two-step approach is necessary to discern how data assimilation affects the TIL, since the 4D-Var increments have to be subtracted from the analysis states (obtained at the first step) to enable the calculation of the static stability structures in both systems before data assimilation was done (see section 2 for methodology details).

The time period for our analysis is January 2010. In this month, our results show a TIL representative of a Northern Hemisphere's winter climatology in both the ERA-Interim reanalysis and ECMWF operational (see section 3), and systematic structures in the mean increments of static stability across all latitudes in both data assimilation systems (see section 4), indicating that these results are robust.

We describe the data used in this study, the procedure to degrade high resolution GPS-RO profiles to the models' pressure levels, and how the increments in static stability are calculated, in section 2. We show how the TIL is represented in the ERA-Interim reanalysis and the ECMWF forecast model compared to degraded observations in section 3. The effect of data assimilation on the TIL strength is discussed in section 4, and we summarize the main conclusions in section 5.

2 Data and Methods

2.1 GPS-RO observations, the ERA-Interim reanalysis and the ECMWF operational forecast model

We use temperature profiles from GPS radio occultation (GPS-RO) measurements made by the COSMIC satellite mission [*Anthes et al.*, 2008]. The profiles have a vertical resolution of 100 m and extend from the surface up to 40 km altitude; which is similar to high-resolution radiosonde measurements, but with the advantage of weather-independence, a much higher measurement density (around 2000 profiles per day), and global coverage. The assimilation of GPS-RO observations has had a major impact in both reanalysis and numerical weather prediction systems, having improved the representation of upper tropospheric and stratospheric temperatures: although GPS-RO data are not the largest observation source (satellite radiances), they do have the highest assimilation rate among datasets in the ERA-Interim reanalysis [*Poli et al.*, 2010], (60-65 % of the observations are assimilated, compared to a 50 % rate of assimilation for radiosondes); and GPS-RO data are among the top influencers on analyses and forecasts in the ECMWF numerical weather prediction system, especially between 10-20 km altitude [*Cardinali and Healy*, 2014].

The ERA-Interim reanalysis [*Dee et al.*, 2011] uses the ECMWF operational forecast model from early 2007 (IFS Cycle 31r2), which has 60 vertical model levels with the top at 0.1 hPa ($\sim$65 km) altitude, a vertical resolution of 700-800 m near the extratropical tropopause and a T255 ($\sim$80 km) horizontal grid.

We also analyze data from a newer version of the ECMWF operational weather forecast system valid in January 2010 (IFS Cycle 35r3), which has 91 vertical model levels with the top at 0.01 hPa ($\sim$80 km) altitude, a 400-500 m vertical resolution near the tropopause and a T1279 ($\sim$16 km) horizontal grid. This allows us to compare the results from ERA-Interim reanalysis to a newer version of the same atmospheric model. Since the operational analysis has better vertical resolution, it should capture the gradients that lead to the TIL better than ERA-Interim, though the main purpose of this comparison is to test whether the effect of data assimilation on the TIL is changed or not in the two versions of the same assimilating model. Both data assimilation systems use four-dimensional variational assimilation (4D-Var, e.g. *Rabier et al.* [2000]) to fit their atmospheric models to the observations (see *ECMWF* [2007a] for an in-depth description).

We use the following 6-hourly output variables from the ECMWF reanalysis and operational systems: surface geopotential, surface pressure, the hybrid coordinates of the model levels (L60 in the reanalysis, L91 in the operational system), and the temperature and specific humidity at the model levels. Also, we use the 4D-Var increments (the difference in the model states before and after data assimilation) of surface pressure, temperature and specific humidity.

From the surface pressure and the hybrid levels, the model levels' pressure can be calculated; and combining the information of surface geopotential and the model levels' pressure, temperature and specific humidity, the geopotential height of each level can be obtained. For a detailed description of the equations used for this in the ECMWF reanalysis and operational atmospheric models, see the vertical discretization chapter in the IFS documentation of *ECMWF* [2007b] (developed after *Simmons and Burridge* [1981]). All datasets are analyzed for January

2010. As discussed in the introduction, we suggest that one month of data is enough given the systematic and similar structures found in both data assimilation systems, regarding 4D-Var increments and differences between the models and degraded GPS-RO observations (see sections 3 and 4).

2.2 Degradation of GPS-RO profiles onto model levels

For each GPS-RO profile, we take the grid point and time nearest to the observation and retrieve the pressure of each hybrid model level (L60 for the reanalysis, L91 for the operational system). Each GPS-RO temperature profile comes together with height and pressure information, and the degraded GPS-RO profile is simply a subsample with the information of the 60 (or 91) levels with pressure closest to the reanalysis (or operational) model levels' pressures. Our method is very similar to the one used by *Gettelman et al.* [2010] and *Hegglin et al.* [2010], but instead of standard pressure levels, we use the local pressure of the models' hybrid levels, allowing variability in space and time.

2.3 TIL Calculations

Using the temperature, height and pressure profiles in ERA-Interim, the ECMWF operational analysis (calculated in section 2.1) and the GPS-RO observations degraded to the same vertical grid as the atmospheric models (see section 2.2), we calculate static stability vertical profiles as the Brunt-Väisälä frequency squared, i.e.:

N^2 (s^{-2}) =$g/\Theta \cdot \partial\Theta/\partial z$, where g is the gravitational acceleration and Θ the potential temperature. Profiles where the tropopause cannot be found and those with temperature $<$-150 °C or $>$150 °C or $N^2 >$ 100×10^{-4} s^{-2} (unrealistic values that we would like to avoid) are excluded, amounting to less than one percent of the profiles.

We define tropopause height (TP_z) as the height of the lapse-rate tropopause following the WMO criterion [*WMO*, 1957], and use it as the reference level for averaging, to obtain tropopause-based zonal-mean N^2 profiles, as in *Birner et al.* [2002]. We calculate the TIL strength as the maximum static stability value (N^2_{max}) in the first 3 km above the tropopause (although our algorithm finds it most often in the first kilometer). This TIL strength measure has the advantage of being independent of its distance from the tropopause and is commonly used [*Birner et al.*, 2006; *Wirth and Szabo*, 2007; *Erler and Wirth*, 2011; *Pilch Kedzierski et al.*, 2015].

2.4 Obtaining the Prior States with 4D-Var increments

To obtain prior values for ERA-Interim and the ECMWF operational system, the 4D-Var increments of surface pressure, temperature and specific humidity are subtracted (each iteration at a time, backwards) from the analysis (or posterior) values. After each subtraction, the calculations from sections 2.1 and 2.3 are done again, obtaining the N^2 profiles and N^2_{max} values in the atmospheric models before each iteration of the data assimilation procedure. In ERA-Interim reanalysis 2 iterations are done during the 4D-Var procedure, whereas 3 iterations are used in the ECMWF operational system.

Note that while the analysis output variables are 6-hourly (00, 06, 12, 18 UTC), the 4D-Var assimilation is done over 12-hour windows, so the increments are also 12-hourly (09 and 21 UTC for the operational system, 03 and 15 UTC for ERA-Interim). The increments are subtracted from the immediately afterward 6-hourly analyses.

This way, we have the same TIL diagnostics of the following datasets: the analysis output from ERA-Interim and the ECMWF forecast model, which are produced after the 4D-Var data assimilation (see sections 2.1 and 2.3), GPS-RO observations with their vertical resolution equaled to the atmospheric models' (sections 2.2 and 2.3), and the model states prior to data assimilation and in between each iteration.

3 The TIL in ECMWF forecasts and reanalysis

Before analyzing the effect of data assimilation on the TIL, this section shows how the TIL is represented in the ERA-Interim reanalysis [*Dee et al.*, 2011] and the newer, higher-resolution ECMWF operational analysis, comparing it to the TIL from degraded GPS-RO observations, which eliminates vertical resolution as a source of differences.

The top row of Figure 1 shows the zonal-mean, tropopause-based N^2 profiles at all latitudes for (a) the ECMWF operational analysis and (b) ERA-Interim, averaged over January 2010. Both panels show N^2 maximized near 1-1.5 km above the tropopause at all latitudes, meaning that the TIL is captured globally in both the operational system and the ERA-Interim reanalysis. The TIL from Figs. 1a and 1b resembles the observed climatological winter structure of the TIL, with relative maxima in the winter (NH) mid-latitudes and the summer (SH) pole [*Birner*, 2006; *Grise et al.*, 2010], and higher N^2 values near the equator, which are present all year round, [*Grise et al.*, 2010] due to the large negative lapse rate in the background temperature profile of the equatorial stratosphere.

Comparing the ECMWF operational system (L91, Fig. 1a) to ERA-Interim (L60, Fig. 1b), the first has a slightly stronger TIL, situated a few hundred meters closer to the tropopause. Given that the operational system in 2010 had a better vertical resolution than the model version used in ERA-Interim (see section 2.1), its ability to capture sharper gradients near the tropopause is straightforward. But when the operational system and ERA-Interim are compared to GPS-RO observations degraded to their respective vertical resolutions (Figs. 1c and 1d), a very similar pattern appears globally: relative to the degraded observations, both ECMWF operational and ERA-Interim have lower N^2 values in the layer 0-1 km above the tropopause (between -0.5 and -1 $\times 10^{-4}$ s^{-2}, blue-purple colors), and higher values in the layer 1-2 km above the tropopause (between 0.25 and 0.5 $\times 10^{-4}$ s^{-2}, yellow-orange colors). This pattern indicates that the TIL in both the 2010 ECMWF operational analysis and ERA-Interim is further away from the tropopause than in the degraded GPS-RO observations. The negative differences in the layer 0-1 km above the tropopause (blue in Figs. 1c and 1d) are about double that of the positive difference in the layer 1-2 km above the tropopause; this suggests that the TIL of the degraded observations is still slightly stronger in both cases (which is confirmed in section 4, Fig.3). We also find that the ECMWF operational analysis and ERA-Interim have higher N^2 in the uppermost troposphere, especially in the extratropics (Figs. 1c and 1d), meaning that the transition from tropospheric values to the higher N^2 in the TIL is less sharp than in degraded observations.

To summarize this section, both ERA-Interim and the ECMWF operational system have a TIL slightly weaker and further away from the tropopause than expected from GPS-RO observations with the same vertical resolution, a difference which persists across all latitudes and has a very similar structure in both systems (Figs. 1c and 1d). *Gettelman et al.* [2010] and *Hegglin et al.* [2010] reported a similar tendency in free-running atmospheric models from CCMVal2 (see figure 12 from *Gettelman et al.* [2010]), with the TIL shifted away from the tropopause and generally weaker than degraded observations. Although to a much lower degree, we see here that this issue is also present in ERA-Interim and the ECMWF forecast system.

4 The Effect of Data Assimilation on the TIL Strength

Figure 2 shows the 4D-Var increments in terms of N^2, calculated as tropopause-based zonal means for January 2010. The largest increments occur in the first iteration of the 4D-Var data assimilation process for both the ECMWF operational system (Fig. 2a) and ERA-Interim [*Dee et al.*, 2011] (Fig. 2d). The first iteration (Figs. 2a and 2d), on average increases

N^2 in the first 1.5 km above the tropopause at all latitudes, and decreases N^2 above and below that layer. The second iteration (Figs. 2b and 2e) has the opposite tendency, but at only about 1/4 of the magnitude, counteracting a small part of the positive increments of the first iteration. The operational system's third iteration (Fig. 2c) has no coherent structures.

Since the overall effect of the 4D-Var data assimilation process is the sum of all iterations, the net increment in N^2 in the first 1.5 km above the tropopause at all latitudes is an increase of $\sim 0.1 \times 10^{-4}\ s^{-2}$ for the operational system and $\sim 0.07 \times 10^{-4}\ s^{-2}$ for ERA-Interim. Although the magnitude is slightly different in the two versions of the assimilating model, the latitude-vertical structures are nearly the same. The N^2 increments have relative maxima where the TIL is stronger during NH winter: near the South Pole, the NH mid-latitudes and at the equator. Although the N^2 increments amount to only about 1.3 % of the actual TIL strength, the timescale of assimilation (12 h) is fast relative to the dynamics associated with the TIL, and an atmospheric model initiated with a TIL as in Fig. 1 cannot drift and smooth out the TIL significantly in a 12 h period. Figure 2 demonstrates that without data assimilation, both versions of the ECMWF atmospheric model tend towards a weaker N^2 in the TIL region. The TIL being further away from the tropopause in the data assimilation systems compared to degraded GPS-RO observations (Fig. 1) cannot be explained by the 4D-Var increments in Fig. 2, since they rather act to slightly compensate this bias.

We conclude from Fig. 2 that the 4D-Var data assimilation systematically increases N^2 in the TIL region at all latitudes, with the TIL prior to the data assimilation steps being consistently slightly weaker in both systems. This is the main result of our study, and it contradicts the hypothesis of *Birner et al.* [2006] that the data assimilation process smoothes out the TIL. Our results show that when high-resolution data (GPS-RO) are assimilated into models with better vertical resolution (ECMWF operational and ERA-Interim) with the most advanced data assimilation techniques (4D-Var), the representation of the TIL is improved. However, we cannot discern which factor contributes the most, e.g. quantifying how much of the improvement in the TIL representation comes from assimilating GPS-RO in contrast with the update from 3D-Var to 4D-Var is impossible nowadays because there is no reanalysis using 3D-Var and GPS-RO data, neither one using 4D-Var without GPS-RO. Additional experiments with one model version (and varying observational input and assimilation techniques) could be carried out in order to point out the key factors.

Nevertheless, from Figs. 1 and 2 we can see that varying horizontal and vertical resolution does not affect the main results in two versions of the same assimilating model: vertical resolution is undoubtedly a limiting factor to resolve the TIL, but the differences between the analyses and degraded observations in ERA-Interim and ECMWF operational have very similar structures (Fig. 1). In the case of the N^2 increments, their structures are also similar, and the TIL is enhanced in both systems (Fig. 2).

Figure 3 summarizes the findings of our study, showing the TIL strength scores over all latitudes, calculated as N^2_{max} (a TIL strength measure independent of the distance from the tropopause, see section 2.3) for ERA-Interim and the operational system (blue and red lines, respectively), their states prior to data assimilation (dotted lines of the same colors), and the observations degraded to the same vertical resolution (L60 light blue; L91 orange, vertically subsampled from the black line). For both ERA-Interim and the operational system, the prior states lie just below the TIL strength scores of the posterior states (blue and red lines) at all latitudes, showing that data assimilation slightly strengthens the TIL globally. However, the degraded observations (light blue and orange) have even better TIL strength scores, meaning that the TIL in both analyses is still weaker than expected from GPS-RO observations degraded to the same vertical resolution (as shown before in Fig. 1). Although data assimilation improves the TIL in ERA-Interim and ECMWF (figures 2 and 3), the TIL there is still weaker and further away from the tropopause than observed, even if we eliminate vertical resolution as an issue (Figures 1 and 3).

5 Concluding remarks

Our study is the first to analyze the TIL in the ERA-Interim reanalysis [*Dee et al.*, 2011] at full vertical resolution, directly from its hybrid model levels, the first to show how the TIL is represented in a newer version of the assimilating model (the 2010 ECMWF operational weather forecast system) and to describe how the TIL is improved by data assimilation. We summarize our results as follows:

1) Our main finding is that the 4D-Var data assimilation system strengthens the TIL in both ERA-Interim and ECMWF operational systems, as seen in globally positive mean N^2 increments in the TIL region (Fig. 2). Therefore, our study updates the findings of *Birner et al.* [2006], who found a weaker TIL in analyses relative to free running models.

2) To the above, we add that although data assimilation improves the representation of the TIL, it doesn't completely compensate a common issue in AGCMs where the TIL is too far away from the tropopause and generally weaker than expected from GPS-RO observations of the same vertical resolution [*Gettelman et al.*, 2010; *Hegglin et al.*, 2010] (Figs. 1 and 3).

3) Both ERA-Interim and a newer version of the same model and assimilation system (ECMWF operational), although having different horizontal/vertical resolutions, show the same structures in terms of N^2 difference from degraded observations, also the same structures of N^2 increments from data assimilation, and both lead to the same conclusions only varying slightly in magnitude. This means that the effect of data assimilation on the TIL remains qualitatively the same when two versions of the same assimilating model with different horizontal/vertical resolutions are compared, suggesting that other factors are of more importance (the model itself, the assimilation technique, the datasets assimilated). Further experiments would need to be carried out to discern which factors are key.

Our study was conducted for January 2010. Although it is only one month, our results show consistent and systematic structures (see sections 3 and 4) across all latitudes in two assimilation systems, indicating their robustness. We showed how data assimilation affects the TIL by analyzing the 4D-Var increments directly. Data assimilation can also improve the representation of dynamics with larger time-scale than the assimilation step, like eddies or the residual circulation, and thereby improve the representation of the TIL in the model. A follow-on study regarding this subject is in preparation.

Acknowledgments

This study was completed within the Helmholtz-University Young Investigators Group NATHAN project, funded by the Helmholtz Association through the president's Initiative and Networking Fund and the GEOMAR Helmholtz-Centre for Ocean Research in Kiel. We thank the ECMWF data server for the availability of data from the ERA-Interim reanalysis and the ECMWF deterministic forecast model (for 4D-Var increments and forecast datasets, MARS access is required since the end of 2015: https://software.ecmwf.int/wiki/display/WEBAPI/Access+MARS) and UCAR for the COSMIC satellite mission temperature profiles (http://cdaac-www.cosmic.ucar.edu/cdaac/products.html We are grateful to two anonymous reviewers for their helpful comments. The discussions and assistance in accessing different datasets by Sebastian Wahl and Wuke Wang are greatly appreciated.

References

Anthes, R. A., P. A. Bernhardt, Y. Chen, L. Cucurull, K. F. Dymond, D. Ector, S. B. Healy, S.-P. Ho, D. C. Hunt, Y.-H. Kuo, H. Liu, K. Manning, C. McCormick, T. K. Meehan, W. J. Randel, C. Rocken, W. S. Schreiner, S. V. Sokolovskiy, S. Syndergaard, D. C. Thompson, K. E. Trenberth, T.-K. Wee, N. L. Yen, and Z. Zeng (2008), The COSMIC/FORMOSAT-3 Mission: Early Results, *Bulletin of the American Meteorological Society*, *89*, 313, doi:10.1175/BAMS-89-3-313.

Birner, T. (2006), Fine-scale structure of the extratropical tropopause region, *Journal of Geophysical Research (Atmospheres)*, *111*, D04104, doi:10.1029/2005JD006301.

Birner, T., A. Dörnbrack, and U. Schumann (2002), How sharp is the tropopause at midlatitudes?, *Geophysical Research Letters*, *29*, 1700, doi:10.1029/2002GL015142.

Birner, T., D. Sankey, and T. G. Shepherd (2006), The tropopause inversion layer in models and analyses, *Geophysical Research Letters*, *33*, L14804, doi: 10.1029/2006GL026549.

Cardinali, C., and S. Healy (2014), Impact of gps radio occultation measurements in the ecmwf system using adjoint-based diagnostics, *Quarterly Journal of the Royal Meteorological Society*, *140*(684), 2315–2320, doi:10.1002/qj.2300.

Dee, D. P., S. M. Uppala, A. J. Simmons, P. Berrisford, P. Poli, S. Kobayashi, U. Andrae, M. A. Balmaseda, G. Balsamo, P. Bauer, P. Bechtold, A. C. M. Beljaars, L. van de Berg, J. Bidlot, N. Bormann, C. Delsol, R. Dragani, M. Fuentes, A. J. Geer, L. Haimberger, S. B. Healy, H. Hersbach, E. V. Hólm, L. Isaksen, P. Kållberg, M. Köhler, M. Matricardi, A. P. McNally, B. M. Monge-Sanz, J.-J. Morcrette, B.-K. Park, C. Peubey, P. de Rosnay, C. Tavolato, J.-N. Thépaut, and F. Vitart (2011), The ERA-Interim reanalysis: configuration and performance of the data assimilation system, *Quarterly Journal of the Royal Meteorological Society*, *137*, 553–597, doi: 10.1002/qj.828.

ECMWF (2007a), IFS Documentation - Cy31r1 - PART II: DATA ASSIMILATION.

ECMWF (2007b), IFS Documentation - Cy31r1 - PART III: DYNAMICS AND NUMERICAL PROCEDURES.

Erler, A. R., and V. Wirth (2011), The Static Stability of the Tropopause Region in Adiabatic Baroclinic Life Cycle Experiments, *Journal of Atmospheric Sciences*, *68*, 1178–1193, doi:10.1175/2010JAS3694.1.

Gettelman, A., and T. Wang (2015), Structural diagnostics of the tropopause inversion layer and its evolution, *Journal of Geophysical Research (Atmospheres)*, *120*, 46–62, doi:10.1002/2014JD021846.

Gettelman, A., M. I. Hegglin, S.-W. Son, J. Kim, M. Fujiwara, T. Birner, S. Kremser, M. Rex, J. A. Añel, H. Akiyoshi, J. Austin, S. Bekki, P. Braesike, C. Brühl, N. Butchart, M. Chipperfield, M. Dameris, S. Dhomse, H. Garny, S. C. Hardiman, P. Jöckel, D. E. Kinnison, J. F. Lamarque, E. Mancini, M. Marchand, M. Michou, O. Morgenstern, S. Pawson, G. Pitari, D. Plummer, J. A. Pyle, E. Rozanov, J. Scinocca, T. G. Shepherd, K. Shibata, D. Smale, H. Teyssèdre, and W. Tian (2010), Multi-model assessment of the upper troposphere and lower stratosphere: Tropics and global trends, *Journal of Geophysical Research (Atmospheres)*, *115*, D00M08, doi: 10.1029/2009JD013638.

Grise, K. M., D. W. J. Thompson, and T. Birner (2010), A Global Survey of Static Stability in the Stratosphere and Upper Troposphere, *Journal of Climate*, *23*, 2275–2292, doi:10.1175/2009JCLI3369.1.

Hegglin, M. I., C. D. Boone, G. L. Manney, and K. A. Walker (2009), A global view of the extratropical tropopause transition layer from Atmospheric Chemistry Experiment Fourier Transform Spectrometer O_3, H_2O, and CO, *Journal of Geophysical Research (Atmospheres)*, *114*, D00B11, doi:10.1029/2008JD009984.

Hegglin, M. I., A. Gettelman, P. Hoor, R. Krichevsky, G. L. Manney, L. L. Pan, S.-W. Son, G. Stiller, S. Tilmes, K. A. Walker, V. Eyring, T. G. Shepherd, D. Waugh, H. Akiyoshi, J. A. Añel, J. Austin, A. Baumgaertner, S. Bekki, P. Braesicke, C. Brühl, N. Butchart, M. Chipperfield, M. Dameris, S. Dhomse, S. Frith, H. Garny, S. C. Hardiman, P. Jöckel, D. E. Kinnison, J. F. Lamarque, E. Mancini, M. Michou, O. Morgenstern, T. Nakamura, D. Olivié, S. Pawson, G. Pitari, D. A. Plummer, J. A. Pyle, E. Rozanov, J. F. Scinocca, K. Shibata, D. Smale, H. Teyssèdre, W. Tian, and Y. Yamashita (2010), Multimodel assessment of the upper troposphere and lower stratosphere: Extratropics, *Journal of Geophysical Research (Atmospheres)*, *115*, D00M09, doi:10.1029/2010JD013884.

Kalnay, E., M. Kanamitsu, R. Kistler, W. Collins, D. Deaven, L. Gandin, M. Iredell, S. Saha, G. White, J. Woollen, Y. Zhu, A. Leetmaa, B. Reynolds, M. Chelliah, W. Ebisuzaki, W. Higgins, J. Janowiak, K. C. Mo, C. Ropelewski, J. Wang, R. Jenne, and D. Joseph (1996), The NCEP/NCAR 40-Year Reanalysis Project., *Bulletin of the American Meteorological Society*, *77*, 437–472, doi:10.1175/1520-0477(1996)077¡0437:TNYRP¿2.0.CO;2.

Kunz, A., P. Konopka, R. Müller, L. L. Pan, C. Schiller, and F. Rohrer (2009), High static stability in the mixing layer above the extratropical tropopause, *Journal of Geophysical Research (Atmospheres)*, *114*, D16305, doi:10.1029/2009JD011840.

Molod, A., L. Takacs, M. Suarez, and J. Bacmeister (2015), Development of the geos-5 atmospheric general circulation model: evolution from merra to merra2, *Geoscientific Model Development*, *8*(5), 1339–1356, doi:10.5194/gmd-8-1339-2015.

Pilch Kedzierski, R., K. Matthes, and K. Bumke (2015), Synoptic-scale behavior of the extratropical tropopause inversion layer, *Geophysical Research Letters*, *42*(22), 10,018–10,026, doi:10.1002/2015GL066409, 2015GL066409.

Polavarapu, S., S. Ren, Y. Rochon, D. Sankey, N. Ek, J. Koshyk, and D. Tarasick (2005), Data assimilation with the canadian middle atmosphere model, *Atmosphere-Ocean*, *43*(1), 77–100, doi:10.3137/ao.430105.

Poli, P., S. B. Healy, and D. P. Dee (2010), Assimilation of Global Positioning System radio occultation data in the ECMWF ERA-Interim reanalysis, *Quarterly Journal of the Royal Meteorological Society*, *136*, 1972–1990, doi:10.1002/qj.722.

Rabier, F., H. Jrvinen, E. Klinker, J.-F. Mahfouf, and A. Simmons (2000), The ecmwf operational implementation of four-dimensional variational assimilation. i: Experimental results with simplified physics, *Quarterly Journal of the Royal Meteorological Society*, *126*(564), 1143–1170, doi:10.1002/qj.49712656415.

Schmidt, T., J.-P. Cammas, H. G. J. Smit, S. Heise, J. Wickert, and A. Haser (2010), Observational characteristics of the tropopause inversion layer derived from CHAMP/GRACE radio occultations and MOZAIC aircraft data, *Journal of Geophysical Research (Atmospheres)*, *115*, D24304, doi:10.1029/2010JD014284.

Simmons, A. J., and D. M. Burridge (1981), An Energy and Angular-Momentum Conserving Vertical Finite-Difference Scheme and Hybrid Vertical Coordinates, *Monthly Weather Review*, *109*, 758, doi:10.1175/1520-0493(1981)109¡0758:AEAAMC¿2.0.CO;2.

Wargan, K., and L. Coy (2016), Strengthening of the Tropopause Inversion Layer during the 2009 Sudden Stratospheric Warming: A MERRA-2 Study, *Journal of Atmospheric Sciences*, *73*, 1871–1887, doi:10.1175/JAS-D-15-0333.1.

Wirth, V., and T. Szabo (2007), Sharpness of the extratropical tropopause in baroclinic life cycle experiments, *Geophysical Research Letters*, *34*, 2809, doi:10.1029/2006GL028369.

WMO (1957), Meteorology-A three-dimensional science, *WMO Bull.*, *6*, 134–138.

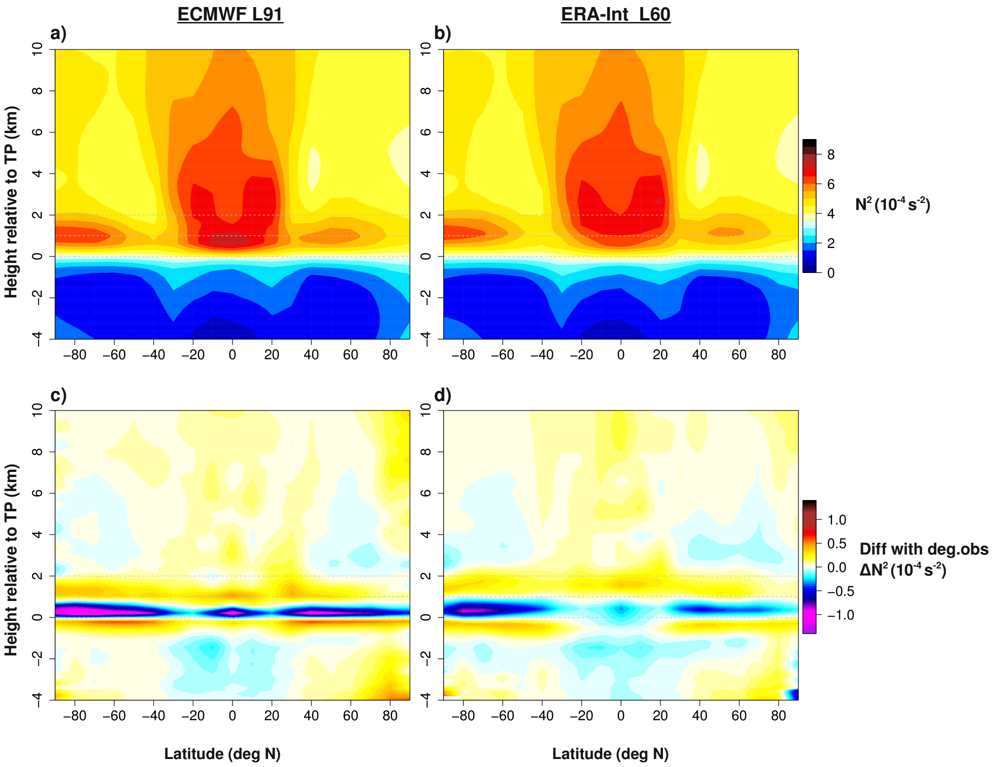

Figure 1. Latitude-height sections of tropopause-based zonal mean N^2 in (a) the ECMWF L91 forecast model and (b) the ERA-Interim reanalysis. The bottom row shows the differences from observations degraded to (c) the pressure of ECMWF's 91 model levels and (d) the pressure of ERA-Interim's 60 model levels. Averaged for January 2010. For orientation, dashed grey lines denote the tropopause and +1/+2 km.

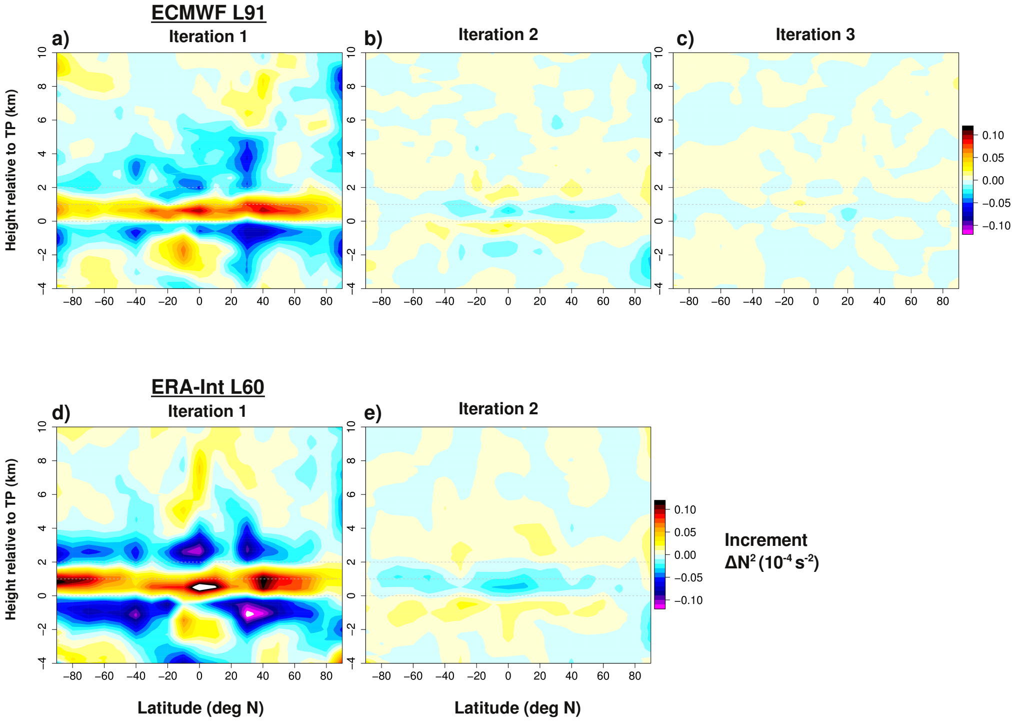

Figure 2. Zonal mean, tropopause-based N^2 increments over successive iterations of the 4D-Var assimilation procedure for the ECMWF L91 forecast model (top row) and the ERA-Interim reanalysis (bottom row). Averaged for January 2010. For orientation, dashed grey lines denote the tropopause and +1/+2 km.

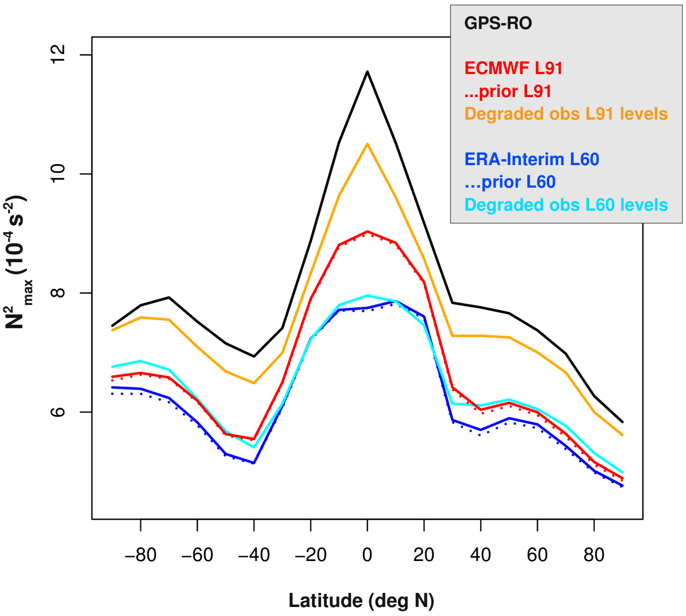

Figure 3. Zonal-mean TIL strength over all latitude bands measured as N^2_{max}. The color lines corresponding to the different datasets are shown in the top-right corner. Averaged for January 2010.

6 Conclusions and Outlook

6.1 Conclusions

This thesis, mainly based on high-resolution GPS-RO observations for the years 2007-2013, has taken a novel approach by studying the TIL from a day-to-day, synoptic-scale point of view, which has provided new information about its intraseasonal and horizontal variability [*Pilch Kedzierski et al.*, 2015; *Pilch Kedzierski et al.*, 2016a]. The quantification of the transient TIL modulation and enhancement by waves (equatorial and extratropical) is a significant step forward in the knowledge of the processes that lead to the formation and maintenance of the TIL [*Pilch Kedzierski et al.*, 2016a,b], and has helped to identify which permanent effects are dominant in the extratropics. Finally, the representation of the TIL in the ERA-Interim reanalysis and the ECMWF operational forecast system has been studied, as well as its improvement by data assimilation directly from the assimilation increments [*Pilch Kedzierski et al.*, 2016c]. This is a fundamental study which updates the hypothesis by *Birner et al.* [2006] and sets a new paradigm about how data assimilation affects modeled TIL.

The goals of this thesis were listed in the introduction (section 1.5), and the results achieved during the doctoral work are grouped accordingly:

(a) Discovery of unknown TIL properties from observations:

Tropics. The TIL properties that are new in literature for the tropics are disclosed below:

- The daily variability of the equatorial vertical N^2 profile shows a TIL seasonal cycle in agreement with previous studies [*Grise et al.*, 2010], and uncovers a new feature above the TIL region: a secondary N^2 maximum close to TIL strength forced by the descending westerly QBO phase, which is not directly modulated by equatorial waves as the TIL [*Pilch Kedzierski et al.*, 2016a].

- Snapshots of the horizontal structures of the TIL show maxima of TIL strength centered at the equator, agreeing with previous studies [*Grise et al.*, 2010; *Kim and Son*, 2012; *Son et al.*, 2011]. In the zonal direction, a stronger TIL is collocated with horizontally divergent flow [*Pilch Kedzierski et al.*, 2016a], which was related to the hydrostatic adjustment to deep convection [*Holloway and Neelin*, 2007; *Paulik and Birner*, 2012]. The TIL-divergence relation is analogous to that of stronger TIL with anticyclonic relative vorticity in the extratropics [*Randel and Wu*, 2010; *Randel et al.*, 2007a].

- The TIL is on average stronger with westerly QBO [*Pilch Kedzierski et al.*, 2016a], unlike in the layer 1-3 km above the tropopause and the rest of the stratosphere, that show higher N^2 values with easterly QBO [*Grise et al.*, 2010].

Extratropics. As above for the tropics, during the doctoral work new properties of the extratropical TIL have been discovered as well:

- The synoptic-scale behavior of the TIL in the extratropics shows that the TIL within ridges (anticyclonic flow) in mid-latitude winter reaches equal or even stronger N^2_{max} values than any TIL found in polar summer [*Pilch Kedzierski et al.*, 2015]. Although the seasonal zonal mean TIL strength in polar summer is the highest [*Birner*, 2006; *Grise et al.*, 2010; *Randel and Wu*, 2010; *Randel et al.*, 2007a], at synoptic-scales the strongest TIL is found within the ridges embedded within baroclinic waves in mid-latitude winter [*Pilch Kedzierski et al.*, 2015].

- In anticyclonic situations, the shear relative vorticity dominates the formation of the strongest TIL [*Pilch Kedzierski et al.*, 2015] as expected from adiabatic balanced dynamics [*Wirth*, 2003, 2004]. However, in strong cyclonic situations the curl relative vorticity gives relatively higher TIL strength [*Pilch Kedzierski et al.*, 2015], suggesting that processes linked to flow imbalance also act to enhance the weaker TIL within cyclones or troughs.

Apart from new TIL properties, a mechanism for TIL formation/maintenance has also been studied in detail within this thesis: how the presence of waves in the tropopause region modulate the zonal structures of the tropopause and enhance the TIL in the zonal mean, as sketched in Fig. 1.7 in the introduction. After extracting the wave anomalies and quantifying their contribution to the zonal-mean TIL, this mechanism turned out to be of primary importance as explained next.

(b) Quantifying the TIL modulation by atmospheric waves:

Tropics. Here the dominant waves are equatorially-trapped modes, which have distinct dispersion curves and are relatively easy to separate in the wavenumber-frequency domain [*Wheeler and Kiladis*, 1999].

- The TIL modulation and enhancement by each equatorial wave type was quantified. All wave types show a maximum net cooling effect centered at the thermal tropopause, and warming above resulting in a net TIL enhancement [*Pilch Kedzierski et al.*, 2016a]. The main contributors are Kelvin waves, followed by IGWs and Rossby waves [*Pilch Kedzierski et al.*, 2016a]. The MJO plays a minor but also important role in modulating temperature and N^2 near the tropopause.

- When the equatorial wave signal is removed, the remaining TIL is much weaker right above the tropopause, but deeper N^2 structures and the secondary N^2 maximum below the descending westerly QBO phase remain [*Pilch Kedzierski et al.*, 2016a].

Extratropics. The method to extract wave anomalies in the tropics was adapted and simplified to fit to the different constraints that extratropical waves have.

- In this case the total signal of planetary and synoptic-scale extratropical waves could be retrieved, without differentiating specific wave types. The instantaneous modulation and transient enhancement of the TIL by these waves is almost entirely responsible for the TIL found at tropopause-based profiles in mid-latitudes [*Pilch Kedzierski et al.*, 2016b], which leads to the conclusion that wave-mean flow interactions, IGWs or the residual circulation are of minor importance there.

- At polar regions, extratropical wave modulation is also dominant, but in addition a clear downward-propagating signal from SSWs or final warmings is visible once the extratropical wave anomalies are removed [*Pilch Kedzierski et al.*, 2016b]. In the NH, major SSWs are responsible for the strongest signals whereas in the SH only final warmings are present during the period 2007-2013. The increases of TIL strength once the downward-propagating signals reach the tropopause region are consistent with a case study by *Wargan and Coy* [2016] who showed that this signal is caused by the accelerated residual circulation from polar vortex breakups.

- The signal from vortex breakups lasts no more than a few weeks, but part of the polar summer TIL is not explained by extratropical wave modulation [*Pilch Kedzierski et al.*, 2016b]. We propose that this is caused by water vapor radiative cooling of the tropopause, since it is the only other mechanism that could enhance the TIL that is restricted to polar summer [*Miyazaki et al.*, 2010a; *Randel and Wu*, 2010].

- After many modelling studies proposing different mechanisms for extratropical TIL formation/maintenance, *Pilch Kedzierski et al.* [2016b] propose that the dominant processes are just three: extratropical wave modulation at all extratropical latitudes; at polar regions also the accelerated residual circulation from polar vortex breakups, and water vapor radiative cooling of the tropopause in polar summer. Although the results by *Pilch Kedzierski et al.* [2016b] point to this direction, the latter two mechanisms would need additional research to be confirmed in a robust manner, i.e. by a direct quantification.

All the TIL-related findings explained above were obtained from GPS-RO observations, but the doctoral work also included the study of reanalysis output, targeting the effect of data assimilation on the reanalysis' TIL. The last part of the thesis encompasses this subject.

(c) Testing the hypothesis of *Birner et al.* [2006] in modern reanalyses:

- The 4D-Var increments of N^2 from ERA-Interim reanalysis and the ECMWF operational forecast system show robust evidence that data assimilation in these systems improves the representation of the TIL, both its strength and location [*Pilch Kedzierski et al.*, 2016c]. Therefore the paradigm that data assimilation smooths out the TIL, valid a decade ago from *Birner et al.* [2006], is updated for newer assimilation systems.

- The TIL in the analyses from both systems is still a bit weaker and further away from the tropopause compared to observations of the same vertical resolution [*Pilch Kedzierski et al.*, 2016c]. This indicates that, although data assimilation improves the TIL representation in these systems, it does not compensate completely for this common bias in atmospheric models [*Gettelman et al.*, 2010; *Hegglin et al.*, 2010].

Overall, this thesis has made significant contributions to the knowledge of observational properties of the TIL and the mechanisms responsible for its formation and maintenance, and sets a new paradigm about how data assimilation affects modeled TIL.

6.2 Outlook

This section will review ongoing or prospective research that has not been included within this thesis. The methods developed during the doctoral work are being used in separated studies that will result in two future papers and a Bachelor thesis.

The methodology developed for this thesis is used in the following projects:

- Different TIL diagnostics used in this thesis will be applied for the analysis of simulations carried out within our research group. The WACCM model assimilating data with the Data Assimilation Research Testbed (WACCM+DART) has produced a 'home-brewed' reanalysis that our group is using to study different processes in the UTLS. The resulting paper about the effect of data assimilation on the TIL, separating the direct assimilation increments from changes of the large-scale circulation, is in preparation by Lisa Neef with myself as the second author, along with Katja Matthes, Sebastian Wahl and Wuke Wang.

- Tropopause data calculated from COSMIC GPS-RO are used in a paper in preparation, studying UTLS water vapor variability, written by Ming Shangguan with myself as the last coauthor, along with Wuke Wang and Katja Matthes.

- Tropopause data calculated from COSMIC GPS-RO will also be used for a Bachelor thesis of a *Physics of the Earth System B.Sc.* student, to be supervised by Karl Bumke and myself.

Some results from this thesis triggered questions that would require a very different or refined approach to be tackled. Although all this could not be investigated during the doctoral work, it shows the potential of the TIL topic to open new and interesting lines for future research.

The questions that arose from the results of this thesis are disclosed next:

- This thesis has focused on properties of the TIL and how it is affected by different processes. Research can be done the reverse way: now how does the TIL affect atmospheric processes? The propagation of various wave types in the tropics and the extratropics, the implications of TIL interaction with baroclinic life cycles, or quantifying the transport of chemical tracers across the tropopause with varying TIL strengths could be topics of high interest for the scientific community.
- The wave amplitudes of all wave types, equatorial or extratropical, are observed to maximize near the tropopause in chapters 3 and 4.2, as observed by *Randel and Wu* [2005] for Kelvin waves. The mechanisms or feedbacks that force this amplification near the tropopause are still unknown.
- What are the roles of particular wave types in enhancing/modulating the TIL in the extratropics? In chapter 3, the separation of different wave types was possible thanks to their distinct dispersion curves, but this was not possible in the extratropics: so far all planetary and synoptic-scale waves are summed-up together in section 4.2, and the methodology to extract the wave signal of a certain wave type (e.g. only the baroclinic Rossby wave) needs to be refined to avoid including other waves into the signal (e.g. barotropic or vertically-trapped modes).

To finish, other analyses were carried out parallel to the doctoral work, which could yield publishable results if investigated further.

Other possible research topics for the future are listed below:

- Wave filtering method: by separating certain wavenumbers, the vertical propagation of Kelvin waves 1, 2, 3 and 4 is possible to track at the equator. A similar method can be applied to track the activity of wavenumbers 1 and 2 in time and height with unprecedented resolution in the extratropics. NH winter and the polar vortex behavior, especially during major SSWs, are of special interest.
- The amplitude variations of these waves can be tested against linear theory: through wave energy density conservation, a relation between the wave amplitude and N^2 (and/or wind shear) should follow, and deviations from this can be detected to show where and when non-linearities occur.

- When power spectrum diagrams as in Fig. 2.3 are made for the extratropics for a certain season, the peaks above the background could coincide with the corresponding lines depicted in Fig. 2.4 for the Rossby wave. Preliminary analyses point to this direction, and an update of *Wheeler and Kiladis* [1999] for the extratropics could be possible upon success of further in-depth tests and case-studies.

- The use of reanalyses for TIL research is encouraged by the results in chapter 5. The time variability of the observed TIL can be compared to the TIL produced by reanalyses, and if the correlations are good, the TIL can be reconstructed back in time. This way the TIL variability associated with QBO, solar cycle, ENSO or volcanic eruptions can be estimated with a multilinear regression analysis. Preliminary results in collaboration with Matt Toohey, using monthly TIL strength indexes from MERRA reanalysis and GPS-RO, show good agreement in the time variability of modeled and observed TIL strength. Also, the multilinear regression analysis is able to separate the different modes of variability associated to the processes mentioned above thanks to their different time-scales.

References

Andrews, D. G., J. R. Holton, and C. B. Leovy (1987), *Middle atmosphere dynamics*, 489 pp., International Geophysics Series, Vol. 40, Academic Press.

Anthes, R. A., P. A. Bernhardt, Y. Chen, L. Cucurull, K. F. Dymond, D. Ector, S. B. Healy, S.-P. Ho, D. C. Hunt, Y.-H. Kuo, H. Liu, K. Manning, C. McCormick, T. K. Meehan, W. J. Randel, C. Rocken, W. S. Schreiner, S. V. Sokolovskiy, S. Syndergaard, D. C. Thompson, K. E. Trenberth, T.-K. Wee, N. L. Yen, and Z. Zeng (2008), The COSMIC/FORMOSAT-3 Mission: Early Results, *Bulletin of the American Meteorological Society*, *89*, 313, doi:10.1175/BAMS-89-3-313.

Baldwin, M. P., L. J. Gray, T. J. Dunkerton, K. Hamilton, P. H. Haynes, W. J. Randel, J. R. Holton, M. J. Alexander, I. Hirota, T. Horinouchi, D. B. A. Jones, J. S. Kinnersley, C. Marquardt, K. Sato, and M. Takahashi (2001), The quasi-biennial oscillation, *Reviews of Geophysics*, *39*, 179–229, doi:10.1029/1999RG000073.

Bell, G. D., and D. Keyser (1993), Shear and Curvature vorticity and Potential-Vorticity Interchanges: Interpretation and Application to a Cutoff Cyclone Event, *Monthly Weather Review*, *121*, 76, doi:10.1175/1520-0493(1993)121<0076:SACVAP>2.0.CO;2.

Bell, S. W., and M. A. Geller (2008), Tropopause inversion layer: Seasonal and latitudinal variations and representation in standard radiosonde data and global models, *Journal of Geophysical Research (Atmospheres)*, *113*, D05109, doi:10.1029/2007JD009022.

Beyerle, G., T. Schmidt, G. Michalak, S. Heise, J. Wickert, and C. Reigber (2005), GPS radio occultation with GRACE: Atmospheric profiling utilizing the zero difference technique, *Geophysical Research Letters*, *32*, L13806, doi:10.1029/2005GL023109.

Biondi, R., W. J. Randel, S.-P. Ho, T. Neubert, and S. Syndergaard (2012), Thermal structure of intense convective clouds derived from GPS radio occultations, *Atmospheric Chemistry & Physics*, *12*, 5309–5318, doi:10.5194/acp-12-5309-2012.

Birner, T. (2006), Fine-scale structure of the extratropical tropopause region, *Journal of Geophysical Research (Atmospheres)*, *111*, D04104, doi:10.1029/2005JD006301.

Birner, T. (2010), Residual Circulation and Tropopause Structure, *Journal of Atmospheric Sciences*, *67*, 2582–2600, doi:10.1175/2010JAS3287.1.

Birner, T., A. Dörnbrack, and U. Schumann (2002), How sharp is the tropopause at midlatitudes?, *Geophysical Research Letters*, *29*, 1700, doi:10.1029/2002GL015142.

Birner, T., D. Sankey, and T. G. Shepherd (2006), The tropopause inversion layer in models and analyses, *Geophysical Research Letters*, *33*, L14804, doi:10.1029/2006GL026549.

Bosilovich, M. G., and Coauthors (2015), MERRA-2: Initial Evaluation of the Climate, *Series on Global Modeling and Data Assimilation Tech. Rep. NASA/TM–2015-104606*, *43*, 145.

Cardinali, C., and S. Healy (2014), Impact of gps radio occultation measurements in the ecmwf system using adjoint-based diagnostics, *Quarterly Journal of the Royal Meteorological Society*, *140*(684), 2315–2320, doi:10.1002/qj.2300.

Das, U., and C. J. Pan (2014), Validation of FORMOSAT-3/COSMIC level 2 ”atmPrf” global temperature data in the stratosphere, *Atmospheric Measurement Techniques*, *7*, 731–742, doi:10.5194/amt-7-731-2014.

Dee, D. P., S. M. Uppala, A. J. Simmons, P. Berrisford, P. Poli, S. Kobayashi, U. Andrae, M. A. Balmaseda, G. Balsamo, P. Bauer, P. Bechtold, A. C. M. Beljaars, L. van de Berg, J. Bidlot, N. Bormann, C. Delsol, R. Dragani, M. Fuentes, A. J. Geer, L. Haimberger, S. B. Healy, H. Hersbach, E. V. Hólm, L. Isaksen, P. Kållberg, M. Köhler, M. Matricardi, A. P. McNally, B. M. Monge-Sanz, J.-J. Morcrette, B.-K. Park, C. Peubey, P. de Rosnay, C. Tavolato, J.-N. Thépaut, and F. Vitart (2011), The ERA-Interim reanalysis: configuration and performance of the data assimilation system, *Quarterly Journal of the Royal Meteorological Society*, *137*, 553–597, doi:10.1002/qj.828.

ECMWF (2007a), IFS Documentation - Cy31r1 - PART III: DYNAMICS AND NUMERICAL PROCEDURES.

ECMWF (2007b), IFS Documentation - Cy31r1 - PART II: DATA ASSIMILATION.

Erler, A. R., and V. Wirth (2011), The Static Stability of the Tropopause Region in Adiabatic Baroclinic Life Cycle Experiments, *Journal of Atmospheric Sciences*, *68*, 1178–1193, doi:10.1175/2010JAS3694.1.

Fueglistaler, S., A. E. Dessler, T. J. Dunkerton, I. Folkins, Q. Fu, and P. W. Mote (2009), Tropical tropopause layer, *Reviews of Geophysics*, *47*, RG1004, doi:10.1029/2008RG000267.

Gettelman, A., and T. Birner (2007), Insights into Tropical Tropopause Layer processes using global models, *Journal of Geophysical Research (Atmospheres)*, *112*, D23104, doi:10.1029/2007JD008945.

Gettelman, A., and T. Wang (2015), Structural diagnostics of the tropopause inversion layer and its evolution, *Journal of Geophysical Research (Atmospheres)*, *120*, 46–62, doi:10.1002/2014JD021846.

Gettelman, A., M. I. Hegglin, S.-W. Son, J. Kim, M. Fujiwara, T. Birner, S. Kremser, M. Rex, J. A. Añel, H. Akiyoshi, J. Austin, S. Bekki, P. Braesike, C. Brühl, N. Butchart, M. Chipperfield, M. Dameris, S. Dhomse, H. Garny, S. C. Hardiman, P. Jöckel, D. E. Kinnison, J. F. Lamarque, E. Mancini, M. Marchand, M. Michou, O. Morgenstern, S. Pawson, G. Pitari, D. Plummer, J. A. Pyle, E. Rozanov, J. Scinocca, T. G. Shepherd, K. Shibata, D. Smale, H. Teyssèdre, and W. Tian (2010), Multimodel assessment of the upper troposphere and lower stratosphere: Tropics and global trends, *Journal of Geophysical Research (Atmospheres)*, *115*, D00M08, doi:10.1029/2009JD013638.

Gettelman, A., P. Hoor, L. L. Pan, W. J. Randel, M. I. Hegglin, and T. Birner (2011), The Extratropical Upper Troposphere and Lower Stratosphere, *Reviews of Geophysics*, *49*, RG3003, doi:10.1029/2011RG000355.

Gorbunov, M. E., H.-H. Benzon, A. S. Jensen, M. S. Lohmann, and A. S. Nielsen (2004), Comparative analysis of radio occultation processing approaches based on Fourier integral operators, *Radio Science*, *39*, RS6004, doi:10.1029/2003RS002916.

Grise, K. M., and D. W. J. Thompson (2013), On the Signatures of Equatorial and Extratropical Wave Forcing in Tropical Tropopause Layer Temperatures, *Journal of Atmospheric Sciences*, *70*, 1084–1102, doi:10.1175/JAS-D-12-0163.1.

Grise, K. M., D. W. J. Thompson, and T. Birner (2010), A Global Survey of Static Stability in the Stratosphere and Upper Troposphere, *Journal of Climate*, *23*, 2275–2292, doi:10.1175/2009JCLI3369.1.

Hegglin, M. I., C. D. Boone, G. L. Manney, and K. A. Walker (2009), A global view of the extratropical tropopause transition layer from Atmospheric Chemistry Experiment Fourier Transform Spectrometer O_3, H_2O, and CO, *Journal of Geophysical Research (Atmospheres)*, *114*, D00B11, doi:10.1029/2008JD009984.

Hegglin, M. I., A. Gettelman, P. Hoor, R. Krichevsky, G. L. Manney, L. L. Pan, S.-W. Son, G. Stiller, S. Tilmes, K. A. Walker, V. Eyring, T. G. Shepherd, D. Waugh, H. Akiyoshi, J. A. Añel, J. Austin, A. Baumgaertner, S. Bekki, P. Braesicke, C. Brühl, N. Butchart, M. Chipperfield, M. Dameris, S. Dhomse, S. Frith, H. Garny, S. C. Hardiman, P. Jöckel, D. E. Kinnison, J. F. Lamarque, E. Mancini, M. Michou, O. Morgenstern, T. Nakamura, D. Olivié, S. Pawson, G. Pitari, D. A. Plummer, J. A. Pyle, E. Rozanov, J. F. Scinocca, K. Shibata, D. Smale, H. Teyssèdre, W. Tian, and Y. Yamashita (2010), Multimodel assessment of the upper troposphere and lower stratosphere: Extratropics, *Journal of Geophysical Research (Atmospheres)*, *115*, D00M09, doi:10.1029/2010JD013884.

Held, I. M. (1982), On the Height of the Tropopause and the Static Stability of the Troposphere., *Journal of Atmospheric Sciences*, *39*, 412–417, doi:10.1175/1520-0469(1982)039<0412:OTHOTT>2.0.CO;2.

Holloway, C. E., and J. D. Neelin (2007), The Convective Cold Top and Quasi Equilibrium*, *Journal of Atmospheric Sciences*, *64*, 1467, doi:10.1175/JAS3907.1.

Kalnay, E., M. Kanamitsu, R. Kistler, W. Collins, D. Deaven, L. Gandin, M. Iredell, S. Saha, G. White, J. Woollen, Y. Zhu, A. Leetmaa, B. Reynolds, M. Chelliah, W. Ebisuzaki, W. Higgins, J. Janowiak, K. C. Mo, C. Ropelewski, J. Wang, R. Jenne, and D. Joseph (1996), The NCEP/NCAR 40-Year Reanalysis Project., *Bulletin of the American Meteorological Society*, *77*, 437–472, doi:10.1175/1520-0477(1996)077<0437:TNYRP>2.0.CO;2.

Kim, J., and S.-W. Son (2012), Tropical Cold-Point Tropopause: Climatology, Seasonal Cycle, and Intraseasonal Variability Derived from COSMIC GPS Radio Occultation Measurements, *Journal of Climate*, *25*, 5343–5360, doi:10.1175/JCLI-D-11-00554.1.

Kunkel, D., P. Hoor, and V. Wirth (2014), Can inertia-gravity waves persistently alter the tropopause inversion layer?, *Geophysical Research Letters*, *41*(22), 7822–7829, doi:10.1002/2014GL061970.

Kunz, A., P. Konopka, R. Müller, L. L. Pan, C. Schiller, and F. Rohrer (2009), High static stability in the mixing layer above the extratropical tropopause, *Journal of Geophysical Research (Atmospheres)*, *114*, D16305, doi:10.1029/2009JD011840.

Kursinski, E. R., G. A. Hajj, W. I. Bertiger, S. S. Leroy, T. K. Meehan, L. J. Romans, J. T. Schofield, D. J. McCleese, W. G. Melbourne, C. L. Thornton, T. P. Yunck, J. R. Eyre, and R. N. Nagatani (1996), Initial Results of Radio Occultation Observations of Earth's Atmosphere Using the Global Positioning System, *Science*, *271*, 1107–1110, doi:10.1126/science.271.5252.1107.

Kursinski, E. R., G. A. Hajj, J. T. Schofield, R. P. Linfield, and K. R. Hardy (1997), Observing earth's atmosphere with radio occultation measurements using the global positioning system, *Journal of Geophysical Research: Atmospheres*, *102*(D19), 23,429–23,465, doi: 10.1029/97JD01569.

Lindzen, R. D. (1967), Planetary waves on beta-planes, *Monthly Weather Review*, pp. 441–451.

Madden, R. A., and P. R. Julian (1994), Observations of the 40 50-Day Tropical Oscillation - A Review, *Monthly Weather Review*, *122*, 814, doi:10.1175/1520-0493(1994)122<0814:OOTDTO>2.0.CO;2.

Matsuno, T. (1966), Quasi-geostrophic motions in the equatorial area, *Journal of the Meteorological Society of Japan. Ser. II*, *44*(1), 25–43.

Miyazaki, K., S. Watanabe, Y. Kawatani, Y. Tomikawa, M. Takahashi, and K. Sato (2010a), Transport and Mixing in the Extratropical Tropopause Region in a High-Vertical-Resolution GCM. Part I: Potential Vorticity and Heat Budget Analysis, *Journal of Atmospheric Sciences*, *67*, 1293–1314, doi:10.1175/2009JAS3221.1.

Miyazaki, K., S. Watanabe, Y. Kawatani, K. Sato, Y. Tomikawa, and M. Takahashi (2010b), Transport and Mixing in the Extratropical Tropopause Region in a High-Vertical-Resolution GCM. Part II: Relative Importance of Large-Scale and Small-Scale Dynamics, *Journal of Atmospheric Sciences*, *67*, 1315–1336, doi:10.1175/2009JAS3334.1.

Molod, A., L. Takacs, M. Suarez, and J. Bacmeister (2015), Development of the geos-5 atmospheric general circulation model: evolution from merra to MERRA2, *Geoscientific Model Development*, *8*(5), 1339–1356, doi:10.5194/gmd-8-1339-2015.

Paulik, L. C., and T. Birner (2012), Quantifying the deep convective temperature signal within the tropical tropopause layer (TTL), *Atmospheric Chemistry & Physics*, *12*, 12,183–12,195, doi:10.5194/acp-12-12183-2012.

Pilch Kedzierski, R., K. Matthes, and K. Bumke (2015), Synoptic-scale behavior of the extratropical tropopause inversion layer, *Geophysical Research Letters*, *42*(22), 10,018–10,026, doi:10.1002/2015GL066409.

Pilch Kedzierski, R., K. Matthes, and K. Bumke (2016a), The tropical tropopause inversion layer: variability and modulation by equatorial waves, *Atmospheric Chemistry and Physics Discussions*, pp. 1–31, doi:10.5194/acp-2016-178, (in review).

Pilch Kedzierski, R., K. Matthes, and K. Bumke (2016b), Wave modulation of the extratropical tropopause inversion layer, *Atmospheric Chemistry and Physics Discussions*, pp. 1–31, (submitted).

Pilch Kedzierski, R., L. Neef, and K. Matthes (2016c), Tropopause sharpening by data assimilation, *Geophysical Research Letters*, *43*, pp. 1–18, doi:10.1002/2016GL069936, (accepted / in press).

Plougonven, R., and F. Zhang (2014), Internal gravity waves from atmospheric jets and fronts, *Reviews of Geophysics*, *52*, 33–76, doi:10.1002/2012RG000419.

Polavarapu, S., S. Ren, Y. Rochon, D. Sankey, N. Ek, J. Koshyk, and D. Tarasick (2005), Data assimilation with the canadian middle atmosphere model, *Atmosphere-Ocean*, *43*(1), 77–100, doi:10.3137/ao.430105.

Poli, P., S. B. Healy, and D. P. Dee (2010), Assimilation of Global Positioning System radio occultation data in the ECMWF ERA-Interim reanalysis, *Quarterly Journal of the Royal Meteorological Society*, *136*, 1972–1990, doi:10.1002/qj.722.

Rabier, F., H. Järvinen, E. Klinker, J.-F. Mahfouf, and A. Simmons (2000), The ecmwf operational implementation of four-dimensional variational assimilation. i: Experimental results with simplified physics, *Quarterly Journal of the Royal Meteorological Society*, *126*(564), 1143–1170, doi:10.1002/qj.49712656415.

Randel, W. J., and F. Wu (2005), Kelvin wave variability near the equatorial tropopause observed in GPS radio occultation measurements, *Journal of Geophysical Research (Atmospheres)*, *110*, D03102, doi:10.1029/2004JD005006.

Randel, W. J., and F. Wu (2010), The Polar Summer Tropopause Inversion Layer, *Journal of Atmospheric Sciences*, *67*, 2572–2581, doi:10.1175/2010JAS3430.1.

Randel, W. J., F. Wu, and P. Forster (2007a), The Extratropical Tropopause Inversion Layer: Global Observations with GPS Data, and a Radiative Forcing Mechanism, *Journal of Atmospheric Sciences*, *64*, 4489, doi:10.1175/2007JAS2412.1.

Randel, W. J., M. Park, F. Wu, and N. Livesey (2007b), A Large Annual Cycle in Ozone above the Tropical Tropopause Linked to the Brewer Dobson Circulation, *Journal of Atmospheric Sciences*, *64*, 4479, doi:10.1175/2007JAS2409.1.

Schmidt, T., J.-P. Cammas, H. G. J. Smit, S. Heise, J. Wickert, and A. Haser (2010), Observational characteristics of the tropopause inversion layer derived from CHAMP/GRACE radio occultations and MOZAIC aircraft data, *Journal of Geophysical Research (Atmospheres)*, *115*, D24304, doi:10.1029/2010JD014284.

Schreck, C. (2009), Extract equatorial waves by filtering in the Wheeler-Kiladis wavenumber-frequency domain., https://www.ncl.ucar.edu/Document/Functions/User_contributed/kf_filter.shtml.

Simmons, A. J., and D. M. Burridge (1981), An Energy and Angular-Momentum Conserving Vertical Finite-Difference Scheme and Hybrid Vertical Coordinates, *Monthly Weather Review*, *109*, 758, doi:10.1175/1520-0493(1981)109<0758:AEAAMC>2.0.CO;2.

Sjoberg, J. P., and T. Birner (2014), Stratospheric Wave-Mean Flow Feedbacks and Sudden Stratospheric Warmings in a Simple Model Forced by Upward Wave Activity Flux, *Journal of Atmospheric Sciences*, *71*, 4055–4071, doi:10.1175/JAS-D-14-0113.1.

Sokolovskiy, S., C. Rocken, D. Hunt, W. Schreiner, J. Johnson, D. Masters, and S. Esterhuizen (2006), GPS profiling of the lower troposphere from space: Inversion and demodulation of the open-loop radio occultation signals, *Geophysical Research Letters*, *33*, L14816, doi:10.1029/2006GL026112.

Son, S.-W., and L. M. Polvani (2007), Dynamical formation of an extra-tropical tropopause inversion layer in a relatively simple general circulation model, *Geophysical Research Letters*, *34*, L17806, doi:10.1029/2007GL030564.

Son, S.-W., N. F. Tandon, and L. M. Polvani (2011), The fine-scale structure of the global tropopause derived from COSMIC GPS radio occultation measurements, *Journal of Geophysical Research (Atmospheres)*, *116*, D20113, doi:10.1029/2011JD016030.

Taylor, J. R., W. J. Randel, and E. J. Jensen (2011), Cirrus cloud-temperature interactions in the tropical tropopause layer: a case study, *Atmospheric Chemistry & Physics*, *11*, 10,085–10,095, doi:10.5194/acp-11-10085-2011.

Tomikawa, Y., Y. Nishimura, and T. Yamanouchi (2009), Characteristics of tropopause and tropopause inversion layer in the polar region, *SOLA*, *5*, 141–144, doi:10.2151/sola.2009-036.

Virts, K. S., and J. M. Wallace (2010), Annual, Interannual, and Intraseasonal Variability of Tropical Tropopause Transition Layer Cirrus, *Journal of Atmospheric Sciences*, *67*, 3097–3112, doi:10.1175/2010JAS3413.1.

Wang, W., K. Matthes, T. Schmidt, and L. Neef (2013), Recent variability of the tropical tropopause inversion layer, *Geophysical Research Letters*, *40*, 6308–6313, doi:10.1002/2013GL058350.

Ware, R., C. Rocken, F. Solheim, M. Exner, W. Schreiner, R. Anthes, D. Feng, B. Herman, M. Gorbunov, S. Sokolovskiy, K. Hardy, Y. Kuo, X. Zou, K. Trenberth, T. Meehan, W. Melbourne, and S. Businger (1996), GPS Sounding of the Atmosphere from Low Earth Orbit: Preliminary Results., *Bulletin of the American Meteorological Society*, *77*, 19–40, doi:10.1175/1520-0477(1996)077<0019:GSOTAF>2.0.CO;2.

Wargan, K., and L. Coy (2016), Strengthening of the Tropopause Inversion Layer during the 2009 Sudden Stratospheric Warming: A MERRA-2 Study, *Journal of Atmospheric Sciences*, *73*, 1871–1887, doi:10.1175/JAS-D-15-0333.1.

Wheeler, M., and G. N. Kiladis (1999), Convectively Coupled Equatorial Waves: Analysis of Clouds and Temperature in the Wavenumber-Frequency Domain., *Journal of Atmospheric Sciences*, *56*, 374–399, doi:10.1175/1520-0469(1999)056<0374:CCEWAO>2.0.CO;2.

Wickert, J., C. Reigber, G. Beyerle, R. König, C. Marquardt, T. Schmidt, L. Grunwaldt, R. Galas, T. K. Meehan, W. G. Melbourne, and K. Hocke (2001), Atmosphere sounding by GPS radio occultation: First results from CHAMP, *Geophysical Research Letters*, *28*, 3263–3266, doi:10.1029/2001GL013117.

Wirth, V. (2001), Cyclone-Anticyclone Asymmetry Concerning the Height of the Thermal and the Dynamical Tropopause., *Journal of Atmospheric Sciences*, *58*, 26–37, doi:10.1175/1520-0469(2001)058<0026:CAACTH>2.0.CO;2.

Wirth, V. (2003), Static Stability in the Extratropical Tropopause Region., *Journal of Atmospheric Sciences*, *60*, 1395–1409, doi:10.1175/1520-0469(2003)060<1395:SSITET>2.0.CO;2.

Wirth, V. (2004), A dynamical mechanism for tropopause sharpening, *Meteorologische Zeitschrift*, *13*, 477–484, doi:10.1127/0941-2948/2004/0013-0477.

Wirth, V., and T. Szabo (2007), Sharpness of the extratropical tropopause in baroclinic life cycle experiments, *Geophysical Research Letters*, *34*, 2809, doi:10.1029/2006GL028369.

WMO (1957), Meteorology-A three-dimensional science, *WMO Bull.*, *6*, 134–138.

WMO (1996), Guide to Meteorological Instruments and Methods of Observation, *6th ed. WMO No. 8*.

Yulaeva, E., J. R. Holton, and J. M. Wallace (1994), On the Cause of the Annual Cycle in Tropical Lower-Stratospheric Temperatures., *Journal of Atmospheric Sciences*, *51*, 169–174, doi:10.1175/1520-0469(1994)051<0169:OTCOTA>2.0.CO;2.

Zängl, G., and K. P. Hoinka (2001), The Tropopause in the Polar Regions., *Journal of Climate*, *14*, 3117–3139, doi:10.1175/1520-0442(2001)014<3117:TTITPR>2.0.CO;2.

Zhang, Y., S. Zhang, C. Huang, K. Huang, Y. Gong, and Q. Gan (2015), The interaction between the tropopause inversion layer and the inertial gravity wave activities revealed by radiosonde observations at a midlatitude station, *Journal of Geophysical Research: Atmospheres*, *120*(16), 8099–8111, doi:10.1002/2015JD023115.

Own Publications

Peer reviewed:

Pilch Kedzierski, R., K. Matthes, and K. Bumke (2015), Synoptic-scale behavior of the extratropical tropopause inversion layer, *Geophysical Research Letters*, *42*(22), 10,018–10,026, doi:10.1002/2015GL066409.

Pilch Kedzierski, R., L. Neef, and K. Matthes (2016c), Tropopause sharpening by data assimilation, *Geophysical Research Letters*, *43*, pp. 1-18, doi:10.1002/2016GL069936, (accepted / in press).

In review / submitted:

Pilch Kedzierski, R., K. Matthes, and K. Bumke (2016a), The tropical tropopause inversion layer: variability and modulation by equatorial waves, *Atmospheric Chemistry and Physics Discussions*, pp. 1-31, doi:10.5194/acp-2016-178, (in review).

Pilch Kedzierski, R., K. Matthes, and K. Bumke (2016b), Wave modulation of the extratropical tropopause inversion layer, *Atmospheric Chemistry and Physics Discussions*, pp. 1-31, (submitted).

In preparation:

Neef, L., R. Pilch Kedzierski, R., W. Wang, S. Wahl, and K. Matthes (2016), Recovery of the tropopause inversion layer by data assimilation, *Journal of Geophysical Research*.

Shangguan, M., K. Matthes, W. Wang, and R. Pilch Kedzierski (2016), Synoptic-scale behavior of the water vapor and its radiative impacts using satellite water vapor data, *Atmospheric Chemistry and Physics*.

Acknowledgements

I would like to start by expressing my deepest gratitude to my supervisors Katja Matthes and Karl Bumke. Thank you for guiding me through this thesis, it has been a great and enjoyable experience including the Polarstern cruise and the international conferences, and somehow we managed to keep the doctoral work on the right tracks all the time. Katja, I will always appreciate you giving me the opportunity to start a career in science.

I also want to say thanks to other colleagues. My current office mates, Wuke Wang for introducing me to the TIL topic and for numerous discussions about it, and Lisa Neef for many English (and one German) checks; and for the fruitful scientific work together. My previous office mates, Matt Toohey and Rémi Thiéblemont for also sharing good advice and many beers with me. Sandro Lubis for good insight and references about wave theory. Sebastian Wahl for all the times I needed technical support or model data. Richard Greatbatch for taking the time to review this thesis, and Daniela Domeisen for joining the examination committee as well. And the rest of the group, secretariat and ME department for making it such a great place to be part of.

All in all, thank you for providing me with the most optimal working environment I could dream of. I feel very lucky to have ended up within your group.

A special mention to Julian Kinzel and Karl for helping me out with the German version of the abstract. Thanks to Julian again and to Robert Kopte for the countless coffees and conversations, kebabs, movings and so forth. Also to my former classmates in the masters course for their help during the exercises and the good times together.

Taking a look back in time, I also want to thank a few people that in some way have defined the path that led me here.

Douglas Maraun, my first Hiwi and my Master thesis supervisor. My working approach and objectivity in science benefited a lot from these experiences. Wonsun Park's support during the Master thesis is greatly appreciated as well. Later on I realized how much my skills improved during that time, and your guidance was of great value.

Ramiro Varela and Gabriel Rosón from Universidade de Vigo: from you I first learned the static stability formula, and I find it to be a nice coincidence that I continuously use it throughout my PhD thesis. You really raised my interest in Geophysics and how they explain the real world, and this was right after leaving Chemistry and I honestly had no idea where I was headed in my studies.

Time for my family now. Thank you Mother. To me you are an example of resilience and firmness to carry on no matter what, which I find admirable. You sure did gift me with some of these abilities, and I wouldn't have been able to get to this point without them. And for the occasional food packages too, dear Lord they are good. Thank you Tomek and Iwona, just for being my brother and sister, for all your moral support and for always being there in my life.

For the sake of completeness, I shall give the ME coffee machine some credit for the achievements of this thesis too, by literally boosting my brain.

List of figures

Abbreviations

3D-Var	Three-Dimension Variational (data assimilation)
4D-Var	Four-Dimension Variational (data assimilation)
AGCM	Atmospheric General Circulation Model
CCMVAL-2	Chemistry Climate Model Validation project 2
CHAMP	Challenging Minisatellite Payload
CMAM	Canadian Middle Atmosphere Model
COSMIC	Constellation Observing System for Meteorology, Ionosphere, and Climate
DA	Data Assimilation
DART	Data Assimilation Research Testbed
DJF	December-January-February
ECMWF	European Centre for Medium-Range Weather Forecasts
EIG	Eastward-propagating Inertia-Gravity wave
ENSO	El-Niño Southern Oscillation
ERA-Interim	European Centre for Medium-Range Weather Forecasts Interim Reanalysis
Ex-UTLS	Extratropical Upper-Troposphere and Lower-Stratosphere
GCM	General Circulation Model
GPS/MET	Global Positioning System Meteorology
GPS-RO	Global Positioning System Radio-Occultation
GRACE	Gravity Recovery and Climate Experiment)
IFS	Integrated Forecasting System
IGW	Inertia-Gravity Wave
JAS	July-August-September
JFM	January-February-March
JJA	June-July-August

LEO	Low Earth Orbiter
LR-TP	Lapse-Rate Tropopause
MERRA	Modern-Era Retrospective Analysis for Research and Applications
MJO	Madden-Julian Oscillation
MRG	Mixed Rossby-Gravity wave
mSSW	Major Sudden Stratospheric Warming
NAM	Northern Annular Mode
NCAR	National Center for Atmospheric Research
NCEP	National Centers for Environmental Prediction
NH	Northern Hemisphere
NCL	NCAR Command Language
OLR	Outgoing Longwave Radiation
PVU	Potential Vorticity Unit
QBO	Quasi-Biennial Oscillation
SH	Southern Hemisphere
SI	Supporting Information
SSW	Sudden Stratospheric Warming
STE	Stratosphere-Troposphere Exchange
sTIL	Strength of the Tropopause Inversion Layer
TIL	Tropopause Inversion Layer
TP	Tropopause
TTL	Tropical Tropopause Layer
UCAR	University Corporation for Atmospheric Research
US	United States
UTC	Universal Time Coordinated
UTLS	Upper-Troposphere and Lower-Stratosphere
WACCM	Whole Atmosphere Community Climate Model
WIG	Westward-propagating Inertia-Gravity wave
WMO	World Meteorological Organization

Declaration

I hereby declare that unless specific reference to others' work is made, and apart from my supervisors' guidance, the contents of this dissertation are original and resulting from my own work. This thesis has not been submitted to another examining body, partially or wholly, as part of any other degree or qualification. This thesis has been prepared subject to the Rules of Good Scientific Practice of the German Research Foundation (Deutsche Forschungsgemeinschaft, DFG).

Robin Pilch Kedzierski
Kiel, 2016